Dissertation

Ink-based preparation of chalcogenide perovskites as thin films for PV applications

---

Ibrahim Simsek

Univ.-Diss.

zur Erlangung des akademischen Grades

"doctor rerum naturalium"

(Dr. rer. nat.)

in der Wissenschaftsdisziplin

"Materialwissenschaften"

eingereicht an der

Mathematisch-Naturwissenschaftlichen Fakultät

Institut für Chemie

der Universität Potsdam

und am

Helmholtz Zentrum Berlin für

Materialien und Energie

Ort und Tag der Disputation:

Potsdam-Golm, 2022

Ibrahim Simsek
"Ink-based preparation of chalcogenide perovskites as thin films for PV applications"
Dissertation
Eingereicht: 15/06/2022
Betreuer: Dr. Thomas Unold, Prof. Dr. Andreas Taubert
Gutachter der Arbeit:
Prof. Dr. Andreas Taubert, Dr. Thomas Unold, Prof. Dr. Aleksander Gurlo

Disputationstermin: 15/12/2022 (Potsdam-Golm)
Promotionsausschuss:
Vorsitzender: Prof. Dr. Yan Lu
Komitee:
Prof. Dr. Andreas Taubert
Dr. Thomas Unold
Prof. Dr. Aleksander Gurlo
Prof. Dr. Dieter Neher
Prof. Dr. Helmut Schlaad

Angefertigt am:
Helmholtz-Zentrum Berlin für Materialien und Energie
Abteilung für Struktur und Dynamik von Energiematerialien (SE-ASD)
Hahn-Meitner-Platz 1
14109 Berlin

Published online on the
Publication Server of the University of Potsdam:
https://doi.org/10.25932/publishup-57271
https://nbn-resolving.org/urn:nbn:de:kobv:517-opus4-572711

Abstract

The increasing demand for energy in the current technological era and the recent political decisions about giving up on nuclear energy diverted humanity to focus on alternative environmentally friendly energy sources like solar energy. Although silicon solar cells are the product of a matured technology, the search for highly efficient and easily applicable materials is still ongoing. These properties made the efficiency of halide perovskites comparable with silicon solar cells for single junctions within a decade of research. However, the downside of halide perovskites are poor stability and lead toxicity for the most stable ones.

On the other hand, chalcogenide perovskites are one of the most promising absorber materials for the photovoltaic market, due to their elemental abundance and chemical stability against moisture and oxygen. In the search of the ultimate solar absorber material, combining the good optoelectronic properties of halide perovskites with the stability of chalcogenides could be the promising candidate.

Thus, this work investigates new techniques for the synthesis and design of these novel chalcogenide perovskites, that contain transition metals as cations, e.g., $BaZrS_3$, $BaHfS_3$, $EuZrS_3$, $EuHfS_3$ and $SrHfS_3$. There are two stages in the deposition techniques of this study: In the first stage, the binary compounds are deposited via a solution processing method. In the second stage, the deposited materials are annealed in a chalcogenide atmosphere to form the perovskite structure by using solid-state reactions.

The research also focuses on the optimization of a generalized recipe for a molecular ink to deposit precursors of chalcogenide perovskites with different binaries. The implementation of the precursor sulfurization resulted in either binaries without perovskite formation or distorted perovskite structures, whereas some of these materials are reported in the literature as they are more favorable in the needle-like non-perovskite configuration.

Lastly, there are two categories for the evaluation of the produced materials: The first category is about the determination of the physical properties of the deposited layer, e.g., crystal structure, secondary phase formation, impurities, etc. For the second category, optoelectronic properties are measured and compared to an ideal absorber layer, e.g., band gap, conductivity, surface photovoltage, etc.

Kurzzusammenfassung

Der stetig wachsende Energieverbrauch in der aktuellen technologischen Ära und die kürzliche Entscheidung der Politik auf Nuklearenergie zu verzichten hat die Menschheit dazu geleitet sich auf alternative umweltfreundliche Energiequellen wie Solare Energie zu fokussieren. Obwohl Silizium Solarzellen das Produkt einer ausgereiften Technologie sind geht die Suche nach hocheffizienten Materialien, die einfach umzusetzen sind weiter. Diese Eigenschaften führten zur Vergleichbarkeit von Halogeniden Perowskiten mit Silizium in Einfachsolarzellen innerhalb eines Jahrzehnts der Forschung. Allerdings mangelt es bei Halogeniden Perowskiten an Stabilität und jene stabile haben eine Blei-Toxizität.

Andererseits bieten Chalkogenide Perowskite aussichtsreiche Eigenschaften als Absorber Materialien für den Photovoltaik Markt auf Grund des hohen Vorkommens der Elemente auf dem Planeten und ihrer chemischen Stabilität in Luft. Auf der Suche nach dem ultimativen Absorber Material für Solarzellen könnte sich eine Kombination der guten optoelektronischen Eigenschaften von Halogeniden Perowskiten mit der Stabilität von Chalkogeniden als guter Kandidat herausstellen.

Infolgedessen untersucht diese Arbeit neue Methoden für die Synthese und das Design dieser neuartigen Chalkogeniden Perowskite, welche Übergangsmetalle als Kationen enthalten, z.B. $BaZrS_3$, $BaHfS_3$, $EuZrS_3$, $EuHfS_3$ and $SrHfS_3$. Es gibt zwei Schritte in den Methoden der Deposition in dieser Untersuchung: Im ersten Schritt werden die binären Verbindungen durch eine Lösungsmittelprozessierung auf dem Substrat aufgebracht. Daraufhin wird im zweiten Schritt das aufgetragene Material in einer Chalkogeniden Atmosphäre getempert, um die Perowskit Struktur durch Festkörperreaktion zu bilden.

Die Untersuchung fokussiert sich außerdem auf die Optimierung eines generalisierten Rezeptes für molekulare Tinte zur Deposition eines Präkursors aus unterschiedlichen binären Verbindungen. Die Implementierung der Präkursor Schwefelung führt entweder zu einer Formation der binären Verbindungen ohne Perowskit Struktur oder in der verzerrten Perowskit Struktur, obwohl für manche dieser Materialien laut Literatur die nadelförmige nicht-Perowskit Struktur günstiger sein sollte.

Zuletzt gibt es zwei Kategorien für die Evaluierung der hergestellten Materialien: Die erste Kategorie behandelt die Determinierung der physikalischen Eigenschaften der deponierten Dünnschicht, z.B. Kristallstruktur, Sekundärphasen, Unreinheiten. In der zweiten Kategorie werden die optoelektronischen Eigenschaften gemessen und mit einem idealen Absorber verglichen, z.B. Bandlücke, Leitfähigkeit, Oberflächen Photospannung, etc.

Acknowledgements

I would like to thank, my advisor, Dr. Thomas Unold for giving me the opportunity to work in his group and for his supports to follow my own curiosity about the material science.

My sincere thanks to Prof. Dr. Andreas Taubert for his excellent supervision and contributions during my thesis writing. He inspired me about what kind of supervisor I should be in the future.

I would like to gratefully acknowledge the financial support of Ministry of National Education of the Republic of Turkey during my PhD.

Thanks to all my colleagues I have worked at HZB at some point: Hasan Arif Yetkin, Ibbi Ahmet, Galina Gurieva and Rene Gunder.

Many thanks to all the members and former members of my work group at the Helmholtz-Zentrum-Berlin: Marin Rusu, Léo Choubrac, Jose Marquez-Prieto, Hannes Hempel, Sergiu Levcenco, Andrea Crovetto, Lars Steinkopf, Fatima Akhundova, Hampus Näsström and Adriana Röttger.

A special thanks to Dr. Pascal Beblo for his extraordinary support and friendship. His constructive critics and jokes shaped this thesis and motivated me to finish writing.

Big thanks to Nelly Birk, Fatih Ozdede and Huseyin Talha Tuncel for their moral supports.

Thanks to all the members of my online-support-team: Alev Irmak Kurtulmus, Ozgur Akcicek, Dogus Dogru, Kivanc Delioglu, Emrah Ozkan and Recep Yarligan.

I gratefully thank to my family for being there for me all the time even though they are physically far far away.

Finally, I want to thank to my girlfriend Adriana, who stood by my side, encouraged me to progress and provided me her unlimited love.

List of abbreviations

CIGS: Copper indium galium diselenide

COD: Crystallography Open Database

CPD: Contact potential difference

DFT: Density Function Theory

DMF: Dimethylformamide

DOS: Density of states

EDX: Energy-dispersive X-ray spectroscopy

*e*TM: Early-transition metals

FWHM: Full width at half maximum

GI-XRD: Grazing incidence X-ray diffraction

ICDD: International Center for Diffraction Data

ICSD: Inorganic Crystal Structure Database

KP: Kelvin Probe

LED: Light emitting diode

MO-CVD: Metalorganic chemical vapor deposition

NIR: Near infrared

OPTP: Optical-Pump Terahertz-Probe spectroscopy

PL: Photoluminescence

PLD: Pulsed laser deposition

PMT: Photomultiplier tubes

PYS: Photoelectron yield spectroscopy

RBS: Rutherford backscattering spectroscopy

RTP: Rapid thermal processing

SEM: Scanning electron microscopy

SPV: Surface photovoltage

sscm: Standard cubic centimeters per minute

XRD: X-ray Diffraction

CHAPTER 1
INTRODUCTION

With the industrial revolution, the trend of an increasing population was observed, which was directly linked to energy consumption in parallel with the increase in the consumption of goods.[1] This amount of energy consumption was used to theorize the estimation approach of civilizations' levels. In 1964 the soviet astronomer Kardashev came up with three types of civilizations, based on their energy consumption, which are called Kardashev scales. In the Type I, the planet could only use the overall energy, that is radiated onto the planet's surface from its parent star. The Type II civilization could use all the energy that is emitted from the parent star, whereas the Type III civilization could use all energy sources in its entire galaxy.[2] According to this definition, the earth is not even rated by Type I, since the annual energy consumption is only around 20 TW, whereas the annual energy amount that shines onto the earth is around 174 000 TW, which is around 4 orders of magnitude higher. Carl Sagan extended this theory by adding other energy sources on planets. And he extrapolated the scale, to determine the current Kardashev scale of the earth. According to his calculations, the Type 0 civilization was using only 1 MW annual energy and the Kardashev scale of the earth in 1973 was about 0.7, which was using around 10 TW energy annually.[3] Although our society is still below Type I in terms of power consumption, which currently is around 20 TW annually, the global capacity for the generation of the solar power is currently reached 1 TW threshold and constitutes only 3.7 % of the generated global energy.[4] The importance of an increase of the amount of energy harvested from the sun is getting more urgent by the hour due to the increasing carbon dioxide level and subsequently the global warming.

In addition, a goal of humanity is to decrease the carbon dioxide level despite an increasing energy consumption. 195 countries signed the Paris Agreement in 2015, to keep the carbon dioxide level below 2 °C above the pre-industrial carbon dioxide level. It was also noted, that it should be limited to 1.5 °C preferably.[5] The Intergovernmental Panel on Climate Change reported in 2018 that decreasing the limit from 2 °C to 1.5 °C will prevent 1.5 to 2.5 million km^2 of the area in the permafrost region from melting and it is still a doable goal.[6] Comparing to other energy sources, solar systems are much more environmentally friendly, and are good instruments to maintain the carbon dioxide level in the range defined by the Paris Agreement while satisfying the increasing energy demand.

The terawatt-scale of photovoltaics is a goal, to assess the future steps and the necessary improvements of the field as well. Its future projections calculate that the installation

requirements of solar facilities are 20-80 TW for 2050 and 80-170 TW for 2100, to make the climate mitigation cost-effective in accordance with the Paris Agreement. To implement this, the aim of humanity is to capture energy by solar collectors in the terawatt scale in the short run. Hence, it is necessary to develop more detailed projections for even bigger-scale solar power facilities.[7] However, building PV infrastructures produces carbon dioxide as well, which contributes to greenhouse emissions. Therefore, the development of low-emission solar technology should be prioritized which e.g., does not include parts produced at high temperatures. For instance, thin film solar cells have advantage over silicon ones due to flexible substrates which do not need metal frame and glass layer. Glass is produced at around 1500 °C when it is produced from the raw materials and the source of this heat is natural gas in most cases which contributes the carbon emission.[8] Even though there is no substrate need for silicon solar cells, the thin film solar cell technology still has the advantage of the potential to be produced at low temperature and deposited on flexible substrates, e.g., high density Teflon can endure up to 342 °C. Thin film perovskites as solar cell absorbers covered the most of the ground in a decade and reached more than 25% of the efficiency as single junction.[9] This incident resulted in searching for new materials in the same family as alternatives.

1.1. Perovskites as PV absorbers

The term perovskite was used for the first time in an article by Gustav Rose in 1839, to honor the Russian mineralogist Lev Perowski.[10] In this publication mainly the physical and chemical properties of perovskites were mentioned, such as color, brittleness, crystal structure, and solubility in various acids. Perovskite materials can be found in nature in their characteristic ABX_3 perovskite crystal structure (where A and B are cations) and are well known for decades. Yet, their usage in the solar photovoltaic field is comparatively new.

Coincidentally, the first report of the photovoltaic effect was published also in 1839 by Alexandre Edmond Becquerel. However, the first material for a solar cell was solid selenium which could reach barely 1-2% power efficiency by the 1870s.[11] Later, high-purity silicon solar cells were developed in 1950, and reached 4% power conversion efficiency in 1954 in Bell Labs being called the first generation solar cells.[11] When silicon solar cells took attention in the 1950s, the research for the second generation solar cells also started whose prominent property was using extremely thin absorber layers compared to silicon cells. With this, the development of new absorber materials with increasing efficiencies started. Cadmium sulfide, was reported for the first time in 1954 as one of the earliest members of the second generation solar cells.[11] In 1956, Gallium arsenide already reached 6% efficiency.[11] Later in the 1980s Copper indium gallium diselenides became popular, which is still commercially available today.[12] On the other hand, perovskites are the most popular member of the third generation

solar cells, which are nanostructured materials as quantum dots, nanowires, and mesoscopic solar cells in the same generation. Kojima *et al.* reported the first perovskite usage in a dye-synthesized solar cell with the power conversion efficiency of 3.8% and the stability for a couple of minutes in 2009.[13] Just a decade later, halide perovskites have reached an impressive efficiency of 25% for a single junction[9] and are expected to reach the power efficiency limit of 33% in a single junction.[14] On the other hand, the lifetimes of halide perovskites are the current issue of them since it has not improved proportionally to their efficiencies. And the replacement of the toxic lead component is still a major challenge. Hence, studies for new types of perovskites are crucial.

With new studies, the old theoretical approaches are tested and revised as well. For instance, Goldschmidt manifested the tolerance factor (*t*) calculation (see Eq. 1.1) for perovskites based on his oxide perovskite studies in 1926, where r_A and r_B are the corresponding ionic radii of the cations and r_X is the ionic radius of the anion of the ABX_3 perovskite structure.[15]

$$t = \frac{r_A + r_X}{\sqrt{2}(r_B + r_X)} \qquad \textit{Eq. 1.1}$$

This tolerance factor that was named after Goldschmidt works well for oxide perovskites, however, its adequacy for halide, sulfide and selenide anions was in dispute. Bartel *et al.* suggested their own modification to the Goldschmidt tolerance factor to make it applicable to halide perovskites as well as oxide ones.[16] However, chalcogenide perovskites were not covered with that approach. On the other hand, the Octahedral factor (μ) calculation (see Eq. 1.2) was put forward to evaluate the stability of the structure since the Goldschmidt tolerance factor is only a structural measure for a perfect cubic structure but not for its stability.[17]

$$\mu = \frac{r_B}{r_X} \qquad \textit{Eq. 1.2}$$

Based on these formulae, the *t* value of the material should be $0.7 < t < 1.1$ whereas the μ value should be $(\sqrt{2}-1) < \mu < (\sqrt{3}-1)$. For sulfide perovskites, μ increases with the transition metals in the structure as B cations respectively, Ti < Sn < Hf < Zr. However, even the highest value of μ for $(A)ZrS_3$ structure is slightly lower than the limits of μ mentioned above. Pilania *et al.* used these formulae to calculate the lattice parameters of oxysulfide perovskites which have more stable structures since oxysulfides have higher μ values.[18] With the exploration of new kinds of perovskites, the knowledge about the nature of perovskites will expand even more.

So that, this can then be used for the development of more stable and more efficient solar cells than the ones, currently available on the market.

1.2. Motivation

Metal halide perovskites are showing outstanding photovoltaic performance, thanks to their good optoelectronic properties, cost-effective production conditions, and the rapid increase in their efficiencies. Over the last decade, it was revealed, that the material science of halide perovskites is an art of finding a balance between cost, efficiency, and stability. By reaching more than 25% of power conversion efficiency for a relatively cheap cost due to a low fabrication temperature of 120 °C, two of the aforementioned three main necessities for solar absorbers were obtained.[19] However, stability issues are still the most problematic part of halide perovskites, which is holding them back from entering the commercial market. While lead halide perovskites are more stable than tin halide perovskites, they are the subject of other discussions, related to toxicity to the environment. On the other hand, chalcogenide materials as solar cell absorbers are known with their stabilities, e.g., kesterites[20] and CIGS[21], whereas their potential for higher efficiency in single junction solar cells is not promising anymore. A cross-breed member of the chalcogenide and the perovskite families could help to reach high efficiency and stability. In addition to the potential for good optoelectronic properties of perovskites, chalcogenide perovskites are thermodynamically stable up to 500 °C in oxygen atmosphere.[22] Their elements are abundant and non-toxic contrary to lead. In these materials the ABX_3 perovskite crystal structure uses an earth alkali metal or a lanthanide with 2+ oxidation state on the A site, a transition metal on the B site, and sulfide or selenide as X anion, which is suitable to optimize the band gap for the desired band gap by exchanging one anion with the other via band gap engineering. One of the disadvantages of chalcogenide perovskites so far is high reaction temperature of around 1000 °C, which is still lower than silicon production temperature and may be decreased by exploring new reaction pathways. This work focuses on chemical solution-based deposition techniques, which require less energy for high-degree sulfurization, which is an important part of the material science, to understand the nature of these materials. Since the materials are investigated here for potential solar cell absorbers, the materials with the potential or reported band gap lower than 2.5 eV are selected which are $BaZrS_3$, $BaHfS_3$, $EuZrS_3$, $EuHfS_3$, $SrHfS_3$, $SrSnSe_3$ and $BaHfSe_3$.[23–25]

1.3. Literature survey about the desired materials

Although the field of chalcogenide perovskites is relatively new, there are reports in the literature of some compounds that were experimentally shown or suggested by simulations to

be thermodynamically stable in the perovskite phase. Based on these reports, the following materials were selected to be investigated further for their potential as absorber material in solar cells. The publications are listed here chronologically.

1.3.1. $BaZrS_3$ perovskite

The material $BaZrS_3$ was reported for the first time by Hahn and Mutschke in 1957, who produced it by solid-state powder reaction from its binary chalcogenides.[26] The produced material was dimorph, which had a partially distorted tetragonal perovskite phase at 800 °C annealing temperature, while the second phase was an unknown structure at the annealing temperature of 900 °C. The first phase of the material was brittle and brown in color, whereas the latter was a softer material and light green in color. Clearfield reported the production of $BaZrS_3$ as powder from the sulfurization of the oxide ternary in 1963 by using CS_2 as a sulfur source at the temperatures between 500-1350 °C.[27] Below 800 °C, the phase of $BaZrS_3$ was tetragonal. Distorted orthorhombic $BaZrS_3$ perovskite was prepared at the temperature between 950-1200 °C. Above this temperature interval, the phase of the product was not indexed. Another method was reported by Lelieveld and Ijdo in 1980.[28] $BaCO_3$ and ZrS_2 powders were mixed and reacted with H_2S flow in an induction furnace at around 1100 °C for a week. The study was about crystallographic properties, and the end product was in the distorted perovskite structure, which was measured by neutron diffraction. In 2009, Bennett *et al.* reported, that the Density Function Theory (DFT) calculations of $BaZrS_3$ in *Pnma* #62 cubic crystal structure estimated a band gap of 1.7 eV, while the band gap of $BaZrO_3$ perovskite was estimated as 3.9 eV.[29]

Perera *et al.* confirmed the band gap value as 1.73 eV for $BaZrS_3$ sulfurized from its ternary oxide in their experimental results in 2016, although the experimental band gap value for $BaZrO_3$ was determined around 5 eV.[30] Moreover, the experiments showed that the band gap of the produced $BaZrS_3$ was direct, and the material was in the distorted perovskite phase. The study also denoted that the properties of the material did not change after 7 months, even though it was stored in the air and washed with deionized water many times. In 2017, Niu *et al.* investigated $BaZrS_3$ that was produced from barium sulfide, elemental zirconium and sulfur with iodine powder as a catalyst.[31] BaS, Zr, and S powders were mixed in the stoichiometric perovskite ratio. The ground powders were put in a quartz tube and 0.5 mg iodine per cm^3 volume was added into the tube before it was sealed under an inert atmosphere. The tube was kept at 600 °C for 60 h. After the reaction process, the produced material was ground and pressed into 13 mm diameter pellets under 600 MPa pressure by a hydraulic cold press. The produced $BaZrS_3$ in the distorted perovskite crystal structure had a brown color. According to energy-dispersive X-ray spectroscopy (EDX) results, the elemental composition of the material was Ba:Zr:S = 1:0.93:3.06. And the photoluminescence (PL) energy at room

temperature was measured as 1.82 eV. The formation energy of the material was reported by Filippone in 2018.[32] To simulate the phase diagrams, the FactSage software was used, which requires the heat capacities and the formation energies of the binary compounds. The formation energy of $BaZrS_3$ was calculated as -1.786 eV/f.u. for the formation from its chalcogen binaries. In 2020, Nishigaki *et al.* produced $BaZrS_3$ powder from its binary chalcogenides at 1273 K.[33] Binary sulfides were heated for 48 hours after they were mixed, pelletized, and sealed in an Argon-filled stainless-steel tube. The band gap of 1.94 eV was measured from the perovskite pellet. Comparotto *et al.* investigated co-sputtering of the $BaZrS_3$ precursor to produce their thin films in 2020.[22] The films were prepared from the sulfide compounds of barium and zirconium, which were sputtered at ambient temperature. For temperatures from 700 to 1000 °C, the rapid thermal processing method (RTP) was used without sulfur addition under N_2 atmosphere. Despite $BaZrS_3$ was produced in distorted perovskite structure from its sulfide binaries, the material contained oxide impurities of at least 4%, stemming from the oxygen-sensitive binaries. The most intense and narrowest XRD-peak was reported for 900 °C with the band gap energy of 1.84 eV.

Gupta *et al.* investigated an alternative method for the deposition of $BaZrO_3$ in 2020 by using stoichiometric barium acetate, zirconium (IV) acetylacetonate, and polyvinyl butyral powders which were dissolved in propionic acid at 60 °C.[34] The prepared transparent solution was spin-coated on substrates. The coated film was calcined in a muffle furnace at 700 °C for 15 minutes and at 870 °C for 40 minutes, to form $BaZrO_3$. The sulfurization process of $BaZrO_3$ occurred at 1050 °C for 4 hours, by using CS_2 gas in argon flow as a sulfur source. CS_2 was introduced into the furnace at 600 °C and the gas flow was stopped after the process was again at 600 °C during the cool down, to evaporate the excess sulfur out. The whole cool down was held naturally, to prevent cracks due to thermal contraction. A polycrystalline perovskite in the distorted orthorhombic perovskite structure was produced. Wei *et al.* used pulsed laser deposition (PLD) to deposit $BaZrO_3$ on sapphire substrates.[35] The sulfurization process was conducted for different substrates at the reaction temperatures of 900, 950, 1000, and 1050 °C for 4 hours. CS_2 as a sulfur source was introduced to the process at 800 °C with a flow rate of 20-25 standard cubic centimeters per minute (sscm). The film, which was produced at 1050 °C, has the peaks of the X-ray Diffraction (XRD) pattern, which matches the database. The EDX result confirms the material with the ratio Ba:Zr:S = 1:1.17:2.91. Márquez *et al.* produced $BaZrS_3$ from its ternary oxide, which was deposited by the PLD method.[36] The deposited oxide perovskite was annealed under H_2S atmosphere at various temperatures between 700-1100 °C. As the annealing temperature increased up to 1000 °C, the band gap energy decreased to 1.99 eV, and the sulfur amount in the structure increased.

Recently, Sharma *et al.* published a solution process method, to produce $BaZrS_3$ thin films by using Barium acetate, zirconium (IV) acetylacetonate, titanium (IV) oxyacetylacetonate, and

polyvinyl butyral which were dissolved in propionic acid at 60 °C.[37] The effect of varied titanium amounts was also studied, to see the changing in the band gap energy of the material. Up to 6 %(at) of titanium alloying decreased the band gap energy from 1.75 eV to 1.4 eV, whereas 8 %(at) started destabilizing the perovskite structure. Yu *et al.* PLD-deposited the already-sulfurized material at 500-700 °C, by using a pre-synthesized $BaZrS_3$ target.[38] As-deposited non-oriented material could only reach 1:1:2.4 ratio for Ba:Zr:S elements. After additional annealing under CS_2 atmosphere at 550 °C for 2 hours, the XRD-peaks for the material became clear. The band gap energies were reported 1.98 and 1.86 eV for the annealing temperature of 650 and 900 °C. Lastly, Comparotto *et al.* reported that SnS usage as a capping layer on sputtered Ba-Zr layers prevents oxidation of the sputtered metals before the sulfurization step which makes them sulfurize under a vacuum of around 1 Pa and at the reaction temperature of 550-590 °C for 20 minutes.[39]

1.3.2. $BaHfS_3$ perovskite

The first report of $BaHfS_3$ production was published in 1980, which was produced as powder from its oxide binaries.[28] The deposited oxide compounds were sulfurized in carbon crucibles at 1373 K for one week by using H_2S as a sulfur source. XRD measurements showed that the formed material was in the distorted perovskite structure. In 2018, Filippone *et al.* calculated a formation energy of -1.756 eV/f.u. for $BaHfS_3$ from its binary chalcogenides.[32] Hanzawa *et al.* also produced the material as powder in 2019 from its chalcogenide binaries, by the solid-state method in an argon sealed stainless-steel tube at 1100 K for 48 hours.[40] The band gap energy of 2.06 eV and 79.1% purity were reported with HfO_2 and BaS impurities. Lastly, Nishigaki *et al.* produced $BaHfS_3$ by the solid-state method as powder in 2020.[33] The chalcogenide binaries were reacted in an argon sealed stainless-steel tube at 1473 K. The band gap was measured as 2.17 eV.

1.3.3. $EuZrS_3$ perovskite

Even though there are two reported phases for $EuZrS_3$, the only publication for the distorted perovskite structure (β-phase) was published also by Lelievel and Ijdo in 1980.[28] Its binary chalcogenides were heated in an evacuated silica tube at 1373 K for one week to obtain the material. XRD measurements were conducted to obtain the lattice parameters. In 2016, Guo *et al.* produced only the needle-like non-perovskite configuration of the material (α-phase) by using the solid-state method, in that mixed and pelletized oxide compounds are sealed with sulfur under a vacuum of $1x10^{-4}$ Torr and heated at 1223 K for 10 days.[41]

1.3.4. $EuHfS_3$ perovskite

Compared to other members of the family, $EuHfS_3$ did not draw much attention. The synthesis of $EuHfS_3$ was reported by Lelieveld and Ijdo in 1980.[28] The material was formed by reacting its binary chalcogenides in an evacuated silica tube at 1373 K for a week. The lattice parameters of the distorted perovskite phase were published, which were measured by XRD.

1.3.5. $SrHfS_3$ perovskite

$SrHfS_3$ was reported for the first time in a study of Lelieveld and Ijdo in 1980, with the lattice parameters, that were measured by XRD.[28] The material was in the distorted perovskite structure. Filippone *et al.* calculated the formation energy of $SrHfS_3$ in 2018 by using DFT, which was -0.503 eV/f.u. for the formation from its chalcogen binaries.[32] Hanzawa *et al.* reported the material as a green-light-emitting semiconductor, due to its strong green photoluminescence exhibition of 2.3 eV observed in a temperature range of 30-300 K.[40] Nishigaki *et al.* produced the material as powder in 2020 with the same technique of Hanzawa *et al.* by heating it at 1373 K for 48 hours after mixing and pelletizing its chalcogen binaries.[33] The material was formed in the distorted perovskite phase with the band gap energy of 2.41 eV.

1.3.6. $SrSnSe_3$ perovskite

In 2017, Ju *et al.* reported, that the $SrSnSe_3$-perovskite material has a calculated-band gap energy of 1.00 eV.[24] Their Density Functional Theory (DFT) results showed that the material has a direct band gap, high mobility, and modest absorption in the infrared range of the sunlight. Furthermore, it might be an eligible material for the band gap engineering, to reach a more optimal band gap by substitution of selenium with sulfide. Thus, their study reported that it might be possible to produce $SrSn(Se,S)_3$, which has a band gap between 1.00 eV for $SrSnSe_3$ and 1.56 eV for $SrSnS_3$ perovskite.[24]

1.3.7. $BaHfSe_3$ perovskite

In 2015, Sun *et al.* published DFT calculations for different perovskite structures, which contain Ca, Sr, Ba, Zr, Hf, Ti, S, and Se elements.[23] They investigated the combination of those elements for three different phases, which are distorted cubic perovskite, orthorhombic perovskite, and needle-like non-perovskite configurations. $BaHfSe_3$, in the distorted cubic perovskite phase, was one of the promising candidates, due to its band gap energy of ~1.6 eV.

However, by the comparison of the formation energies, it is explored, that the needle-like non-perovskite configuration was the most favorable phase among the other phases. For this, it could be challenging to keep a stable phase in the perovskite structure.[23]

In 2017, Moroz reported in his PhD thesis, that $BaHfSe_3$ perovskite as powder was produced by using a solid-state reaction, to fabricate highly efficient inorganic solar cells, due to its band gap energy of 1.6 eV.[42] According to his report, this absorber material almost has the cubic perovskite structure. Moreover, no secondary phase was identified for fabrication temperatures of up to 1375 K, which was the highest temperature, that the setup can reach. Thus, this might show, that the material is highly stable at high temperatures. However, Sopiha *et al*. refuted this material later, by stating that the results of Moroz might have an indexation mistake with the XRD-results.[43]

1.4. Publications in peer-review journals

(1) Pareek, D.; Taskesen, T.; Márquez, J. A.; Stange, H.; Levcenco, S.; **Simsek, I.**; Nowak, D.; Pfeiffelmann, T.; Chen, W.; Stroth, C.; Sayed, M. H.; Mikolajczak, U.; Parisi, J.; Unold, T.; Mainz, R.; Gütay, L. Reaction Pathway for Efficient $Cu_2ZnSnSe_4$ Solar Cells from Alloyed Cu-Sn Precursor via a Cu-Rich Selenization Stage. *Sol. RRL* **2020**, *4* (6), 2000124. https://doi.org/10.1002/solr.202000124.

(2) Márquez, J. A.; Rusu, M.; Hempel, H.; Ahmet, I. Y.; Kölbach, M.; **Simsek, I.**; Choubrac, L.; Gurieva, G.; Gunder, R.; Schorr, S.; Unold, T. $BaZrS_3$ Chalcogenide Perovskite Thin Films by H_2S Sulfurization of Oxide Precursors. *J. Phys. Chem. Lett.* **2021**, 2148–2153. https://doi.org/10.1021/acs.jpclett.1c00177.

(3) Yetkin, H. A.; Kodalle, T.; Bertram, T.; Tovar, A. V.; Klenk, R.; Rusu, M.; Ibaceta-Jana, J.; Ruske, F.; **Simsek, I.**; Muydinov, R.; Szyszka, B.; Schlatmann, R.; A. Kaufmann, C. Elucidating the Effect of the Different Buffer Layers on the Thermal Stability of CIGSe Solar Cells. *IEEE J. Photovoltaics* **2021**, 1–10. https://doi.org/10.1109/JPHOTOV.2021.3053483.

CHAPTER 2
FUNDAMENTALS OF DEPOSITION AND ANALYSIS

There are many fields in the semiconductor industry: e.g., solar cells, capacitors, cathodes for water splitting, catalysts, LEDs, etc. This study only focused on the main measurements for solar cells to see if the absorber material is good enough to give a try for building a full solar cell.

In this chapter, the general structural and compositional properties of inorganic chalcogenide perovskites and their various binary compounds are investigated for the usage as absorber materials. The details about the material specific methods will be explained in the next chapters.

2.1. Synthesis of chalcogenide perovskites

The solution processing method is practical, to deposit precursors with a variety of compounds due to easily processabilities of them in solvents. Compared to other deposition techniques, solution processing is uncomplicated and low-cost, but difficult to reproduce and their production processes need to be optimized. In this study, the synthesis starts with the preparation of molecular inks with selected binaries in convenient solvents. Consequently, the prepared ink is spin-coated on suitable substrates homogenously. Finally, the coated precursor materials are heated under experimentally defined conditions, to form the perovskite crystal structure. The precursor deposition and pre-annealing procedures are implemented in a nitrogen filled glovebox to keep the oxygen level on the film low. Since the high temperature annealing procedure is conducted in a reactive gas atmosphere, the samples are exposed to oxygen very briefly (< 1 minute) while transferring them from an air-tight box to the annealing furnaces.

2.1.1. Fundamentals of molecular ink preparation

Halide perovskites are prepared by using the ‘One-step method’, in which binaries of perovskite materials are mixed in a single solution that can be deposited to form a ternary perovskite. It is difficult to produce chalcogenide perovskites with the one-step method due to

the low solubility of sulfide binaries.[44] On the other hand, acetate binaries, which are known for their use in H_2S sensors due to their fast reaction kinetics, are easy to sulfurize with hydrogen sulfide.[45] The acetates have very similar solubilities to chloride compounds and are quite soluble in aqueous solvents.[44] However, water as a solvent results in metal hydroxide formation at high temperatures, which is difficult to substitute with sulfur in the course of sulfurization. In the solution preparation process of perovskite absorber materials, the most used solvent is anhydrous dimethylformamide (DMF) which is also a polar solvent like water. DMF dissolves metal halides and is suitable for the S_N2 substitution reactions due to its polar aprotic properties.

As an alternative, catalytic studies denote that the partial usage of barium halides for chalcogenide perovskite reactions increases the reaction rate and decreases the reaction duration from days to hours.[46,47] However, using only earth-alkali metal iodide as a earth-alkali metal source caused transition metal impurities in the material due to higher energy need for sulfurization of these impurity compounds. Hence, the iodide compound of one of the binaries is used up to 20%(at) as a catalyst for sulfurization reaction in this study. And, since the iodide addition into the ink results in partial precipitation of transition metal iodide, glacial acetic acid is used as a buffer layer for the acetate compounds. Acetic acid helps to dissolve halides and does not cause solvolysis.[48] When the solution is saturated enough, the spin-coating process is initiated.

2.1.2. Spin-coating of solutions on substrates

Spin-coating is a low-cost and common method to coat substrates up to dimensions of 10 cm to 10 cm. For spin coating two different techniques can be followed; some reports suggest that the solution should be injected in the center of the substrate during spinning so that the liquid material can be distributed evenly by the centrifugal force (see Fig. 2.1). Another possible technique is dripping the solution onto the whole substrate before starting to spin which makes it possible for the material to form crystal seeds on substrates before spin-coating. The saturation of injected solutions should be optimized according to the selected injection procedure to provide a homogenous layer on the spinning substrates due to change in viscosity which will change the thickness of the film as well. For the selection of the substrate, it must be considered that it must stand without a phase change in the temperature interval of the later to be conducted annealing.

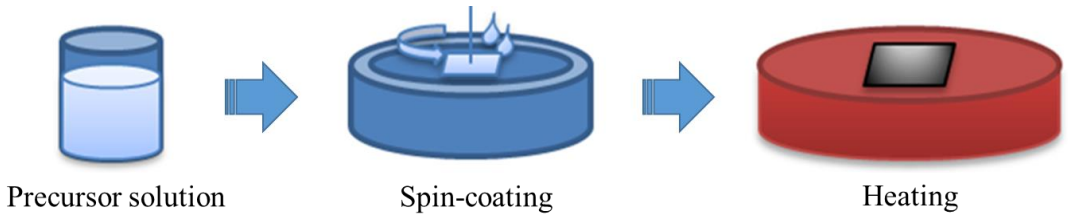

Figure 2.1: Scheme of the experimental procedure. After the preparation of the precursor ink, the solution is deposited on the substrate by spin-coating. The final precursor layer is achieved by pre-annealing to evaporate the solvents before implementing the sulfurization to the sample in the reactive-gas atmosphere.

When the substrate is coated homogeneously with the precursor solution, it requires to be pre-annealed to evaporate the solvent. If no reaction is desired before sulfurization, the pre-annealing temperature should be selected slightly above the boiling temperature of the solvents which is 153 °C for DMF and 118 °C for glacial acetic acid. It should be taken into consideration if there is a possible decomposition temperature for any of the compounds below the pre-annealing temperature since any decomposition would change the stoichiometry of the final product. Most of the substrates are broken into two before selenization to see the difference that only comes from the sulfurization but not from the deposition.

2.1.3. Reaction pathways of absorber layers during sulfurization

For the annealing step, in which precursor materials develop bonds and form the crystal structure of the desired materials, two different annealing setups are studied. It is observed in this study, that high temperatures, even in the reactive atmosphere of H_2S, are needed to conduct the molecular perovskite formation for chalcogenide perovskite materials. Hence, annealing under the reactive H_2S atmosphere is the main part of this study.

The formation reaction pathways of perovskites depend on the selection of the binaries. To form the ABX_3 perovskite structure, acetate compounds of A cations are used in this study which are metals with 2+ oxidation states. Unless there is oxygen in the atmosphere, acetate compounds decompose into oxalates. As temperature increases, oxalates decompose into carbonates and carbonates turn into oxides respectively (see Eq. 2.1).[49]

$$A(CH_3COO)_2 \xrightarrow{\uparrow 2CH_3^-} A(C_2O_4) \xrightarrow{\uparrow CO} A(CO_3) \xrightarrow{\uparrow CO_2} AO \qquad \textit{Eq. 2.1}$$

An acetate ion is a conjugated base of acetic acid, whereas an oxalate ion is a conjugated base of a hydrogenoxalate ion and the secondary dissociation of oxalic acid since it is diprotic.

Moreover, a carbonate ion is a conjugated base of bicarbonate ions, and the secondary dissociation of carbonic acids. Hence, sulfurization of acetates by using H_2S, which has a reactive acidic nature, can take place easily without dealing with oxide substitution. Starting with the barium acetate at room temperature, each of the decomposition products can be obtained at 300, 400 and 500 °C respectively.[49]

Metal acetylacetonate compounds are commonly used for the metalorganic chemical vapor deposition (MO-CVD) technique due to their decomposition properties at low temperatures. Metal acetylacetonates are used as B cations as well as metal acetates in this study when the acetate compound of the B cation is not commercially available. Under vacuum conditions, acetylacetonates can be easily evaporated and decomposed into metal oxides (see Eq. 2.2).

$$B(acac)_4 \xrightarrow{\uparrow 4acac} BO_2 \qquad \textit{Eq. 2.2}$$

Chang *et al.* reported in 2010 that hafnium (IV) acetylacetonate sublimes at 190 °C and starts to decompose into HfO_2 and acetylacetone.[50]

Metal halides are well-known compounds in not only the perovskite field but also in the photovoltaic field in general, e.g. the halide compounds are used for $Cu_2ZnSnSe_4$ production.[51] Halide compounds of metal halides can be substituted by chalcogens in the reactive chalcogen atmospheres to form hydrogen halides and metal chalcogenides which is why H_2S is used as a sulfur source for sulfurization in this work.

2.1.3.1. Sulfurization with reactive H_2S in argon flow reactor

Argon flow reactors have a very similar concept to tube furnaces. One of the biggest differences with this argon flow setup to tube furnaces (see Fig. 2.2) is using reactive hydrogen sulfide (H_2S) in an argon flow as a sulfur source instead of solid selenium or sulfur chunks. Another difference is that there is a continuous flow in the reactor which might be a problem for materials with low evaporation temperature since some of the materials might be swept off by the flow and the elemental composition might have been changed and resulting in undesired side products or secondary phases.

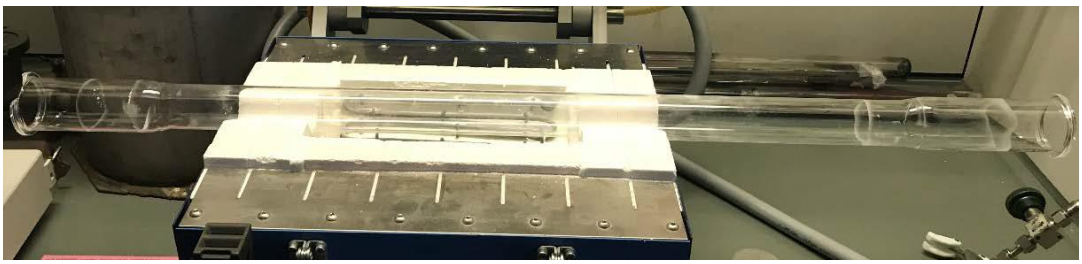

Figure 2.2: Tube furnace setup that uses reactive H_2S in argon flow. During the process, the lid of the furnace is closed, and the flow tubes are connected. The samples are placed in the center of the quartz tube before connection.

Even the desired final product might be swept off by the flow as well which might change the qualities of coated layers like homogeneity, thickness, coverage, etc. Moreover, hydrogen disulfide is very toxic, and extra precautions must be taken to prevent possible toxic exposure. Therefore, the whole processes must be performed under a fume hood by using two additional light and voice alarms connected to H_2S sensors. The oven can be heated up to 1200 °C, which is the temperature limit for the glass transition temperature of the quartz reactor tube.[52]

2.1.3.2. Tube-furnace for selenization

To avoid the cross contamination, a separate tube-furnace, which is designed only for the selenization (Fig. 2.3), is used in this study. In 1993, Lakshmikumar *et al.* used a similar setup to selenize chalcopyrites at around 340-400 °C.[53] In 2013, Bucherl *et al.* optimized a similar setup for kesterites by changing the process temperature to reach the optimal vapor pressure of selenium. It was reported that the selenium vapor pressure was between 33 and 70 Torr at the temperature range of 500-530 °C.[54] The vapor pressure of selenium can be calculated from the previous literature, since it is well studied.

The pre-annealed solid precursor layer on a soda-lime glass substrate is sealed in a graphite box with selenium chunks. Then, the graphite box is put into the furnace and the furnace is pumped down to a pressure of 10^{-3} mbar and then filled with nitrogen to the reaction pressure of 100 mbar. The oven is then heated up to ~540 °C for 30 minutes. Only after the desired final temperature is reached, the graphite box with the sample is placed into the hot zone of the furnace. After 30 minutes at ~540 °C, which is the highest temperature for this selenization setup, the graphite box is pulled back to the cold zone to cool down naturally.

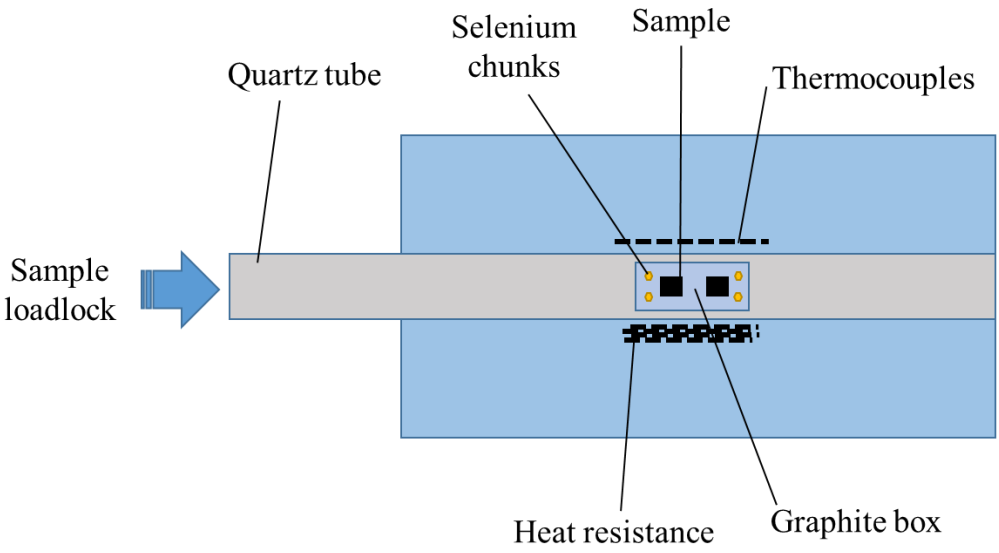

Figure 2.3: Scheme of the tube furnace. Different than the sulfurization furnace, this setup does not have a flow of a reactive gas. The driving force of the reaction is the partial pressure of the selenium chunks.

Under these process conditions, the selenium chunks start to evaporate and diffuse into the spin-coated precursors of perovskite absorber layers. The driving force of the reaction here is the partial pressure of the selenium chunks inside the graphite box being an example of a batch reactor, whereas the reactive H_2S is the driving force in the argon flow reactor. Thus, the required partial pressure to push the reaction to the formation side of chalcogenides can be obtained. The inner volume of the graphite box used in this furnace is ~60 mL. In most cases, selenization takes place firstly with the individual precursors since the formation of the desired perovskite phase needs much more energy. Different secondary phases or side products as impurity can be produced if there is a problem with the selenization of one of the precursors.

2.1.4. Alloying properties of chalcogenide perovskites

Compared to other deposition techniques, solution processing has a significant advantage for alloying. Miscible compounds of the desired alloy materials can be dissolved in the same solvent in the solution processing method. Any modification on the stoichiometry can be done easily. In contrast, for PLD or sputtering techniques targets of the already-alloyed materials are used, that have to be prepared in advance, , which is an extra workload, expensive and thus more complicated to study compositional changes. Using the targets of the main material together with additionally, separately prepared alloy targets is an alternative way; however, it could result in inhomogeneities and defects.

Alloying can change the band gap, the phase of materials due to the lattice parameters, and the type of semiconductors in accordance with the Vegard's Law, which explains how the

changing in the lattice parameters depends on the compound proportions of the solid solutions.[55] For instance, although $BaZrS_3$ has the distorted perovskite structure and $BaTiS_3$ has the hexagonal crystal structure, alloying $BaZrS_3$ with up to 6%(at) of $BaTiS_3$ does not change the crystal structure of $BaZrS_3$. However, it decreases the band gap remarkably from 1.7 to 1.4 eV. Beyond 6%(at) of alloying, phase segregation is observed.[37] Alloying an n-type material with a p-type material or vice versa might change the type of semiconductor as well.

2.2. Characterization of chalcogenide perovskites

Choosing the proper characterization techniques is a key element for the material sciences; it is especially significant in the development of novel materials. With this motivation for this project, fundamental characterization instruments were implemented, to see the material characteristics firstly. And additional measurements were performed for their optoelectronic potentials as the second step. In the end, they complemented each other as the results fitted to the literature data of the desired materials. The setups used for these investigations are described in the following.

2.2.1. X-ray fluorescence (XRF)

X-ray fluorescence (XRF) yields quantitative information about the elemental composition of the measured material. In an XRF instrument, an X-ray tube is used as an X-ray photon source which is emitted on materials. This X-ray exposure results in the excitation of the materials' inner electrons since the energy of X-ray is higher than the electron binding energies of measured materials. An electron from a higher orbital moves towards the electron-hole, creating an X-ray photon. XRF measures this characteristically created X-ray energy due to electron excitations.

Figure 2.5: The image of the X-ray fluorescence instrument.

In this work, a Bruker M4 Tornado XRF instrument (see Fig. 2.5) was used which has a rhodium tube as an X-ray source. The rhodium tube uses a voltage of 50 kV and a current of 200 µA. And the polycapillary optic in the XRF measures a ~20 µm spot size. For the quantification of the results, the proprietary software from Bruker was used. To cross-check, the elemental composition of barium zirconium trisulfide was also determined with Rutherford backscattering spectroscopy (RBS), and only a deviation of 1% was observed for the results from the XRF setup used in this work.

2.2.2. X-ray diffraction (XRD)

XRD is a useful measurement since it is a rough method to determine side products and secondary phases, which might be detrimental for the optoelectronic properties of the material. X-ray diffraction gives information about the crystal structures of all materials present in the sample. If the quantities of side products and secondary phases are large enough, they can be detected by XRD as well, by additional peaks from their lattices.

An XRD measurement is commonly conducted by detecting the angle dependent diffraction intensity of X-rays. For the generation of the X-rays in the lab, an X-ray tube with a copper tube is commonly used. The detector of the instrument measures the diffraction intensity. The plot which relates the intensity to the angle is called a diffractogram. The X-ray interference into the material affects the intensity.[56]

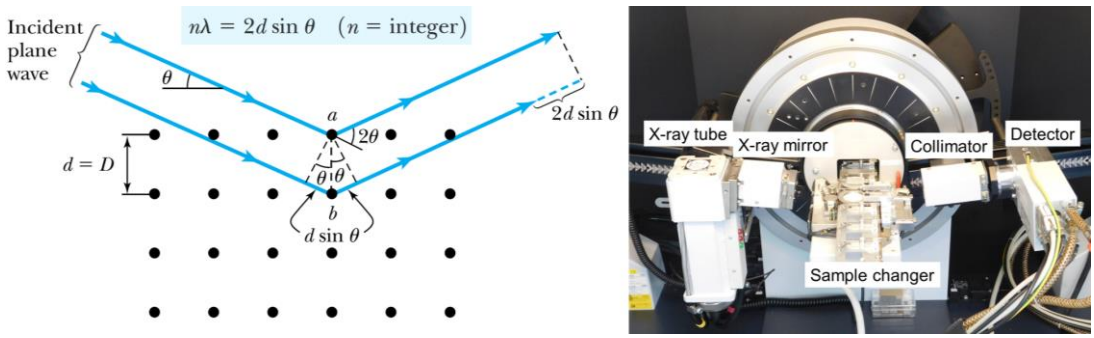

Figure 2.6: Scheme of Bragg's Law (reprinted with permission: Thornton, S. T.; Rex, A. F. *Modern Physics for Scientists and Engineers*, 4th ed., 2013) and the GI-XRD instrument of HZB Corelab.

In this study, the Bruker-D8 Advance and PANalytical X'Pert MPD Pro grazing incidence X-ray diffraction (GI-XRD) instruments in HZB Corelab were used which have Cu-Kα X-ray tube (λ=0.154059 nm). The X-ray tubes are operated at a current of 30-40 mA and a voltage of 40 kV. The software of the instrument is connected to the databases of the Crystallography Open Database (COD) at the University of Cambridge and the International Center for Diffraction Data (ICDD) which is used for a quick phase identification.

For the evaluation of the measurement, a model of the crystal structure is refined to fit the measured diffractogram. This model includes the space group and the unit cell parameters. Then, information about the crystal structure of the sample can be read from this refined model. One technique to perform this refinement is named the Le Bail Method which gives the lattice parameters of the measured material.[57] Also, the extra information from the Le Bail fit can be used in the Rietveld Analysis which gives the phase quantities different than the Le Bail Method. These analyses are implemented in either FullProf or in Profex which is an open-source code and has graphical user interface and used for the analysis conducted in this work. For $BaZrS_3$, GI-XRD measurements and Le Bail analysis were done by Dr. Galina Gurieva.

2.2.3. Scanning electron microscopy (SEM)

On scanning electron microscopes, it is possible to image the material down to a few nanometer scales, which is vital for morphological material characterization. SEM can be used for the determination of thicknesses of spin-coated materials, coverage ratios on substrates, crystal sizes and crystal phases of materials. As the SEM setup, *Leo Gemini 1530* is used in this study (see Fig. 2.7), whose electrons are accelerated within 3-10 kV acceleration voltages and a beam current of 80 µA. Accelerated electrons scatter both elastically and inelastically when they hit the material.

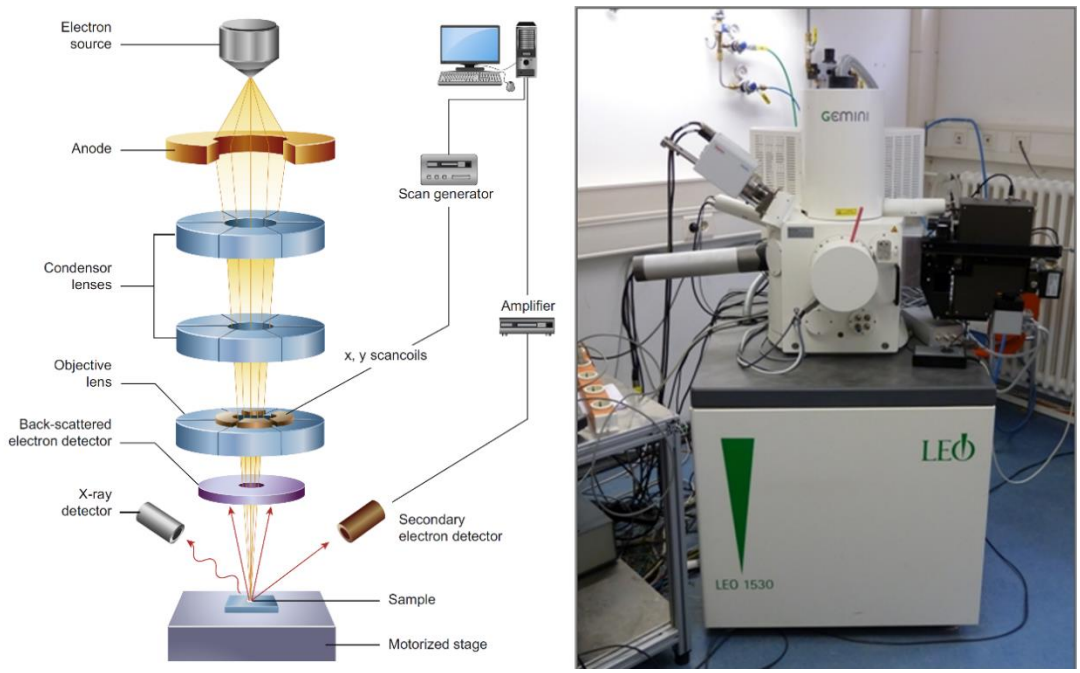

Figure 2.7: Schematic diagram illustrating the imaging methodology of scanning electron microscopy (left) and the image of the SEM used in this study in the HZB Corelab (right). The illustration is reprinted with permission: Inkson, B. J. 'Scanning Electron Microscopy (SEM) and Transmission Electron Microscopy (TEM) for Materials Characterization.' Materials Characterization Using Nondestructive Evaluation (NDE) Methods; Elsevier, 2016; 17–43.

The SEM used in this study has two kinds of secondary electron detectors for imaging. One is placed closer to the specimen is called in-Lens and the other one is for the rest of secondary electron beams. There is also a separate detector for back-scattered electrons as well. Secondary electrons occur as a result of inelastic scattering, whereas back-scattered electrons are produced by elastic scattering of incident electrons.[58] This SEM setup also features an additional detector to make energy dispersive X-ray (EDX) analysis. Electrons in the ground state of elements in materials are excited and forced to leave the shell. Thus, electron holes are formed. When other electrons from the outer shells fill these electron holes, the energy differences between shells are emitted in X-ray forms. EDX detectors measure this characteristic X-ray energy. In contrast, in X-ray fluorescence (XRF), the electron excitation is induced by X-ray photons, instead of an electron beam (see chapter 2.2.1). This method can be used to determine the elemental composition of the material with the consideration of the standard deviation of the detector.

2.2.4. Raman spectroscopy

Raman spectroscopy can be used to obtain the characteristic information about the molecular interactions of the material since it determines the vibrational modes of molecules. It is

sensitive to not only secondary phases but also to crystalline impurities, strains, and defects. The light scattered from the measured material shows two types of behaviors: some of the photons scatter inelastically (Raman scattering) whereas most of them scatter elastically (Rayleigh scattering). The energy of the elastically scattered light can be filtered easily. On the other hand, the inelastic scattering of light causes energy shifts based on photon-phonon interaction during the scattering. Thus, a Raman spectrum can be plotted by measuring the energy of the scattered light with these energy shifts. The increases in energy on Raman spectrums are called anti-Stokes whereas the decreases in energy are called Stokes.[59] Raman spectra were measured using a *Renishaw inVia* confocal Raman spectroscopy which is equipped with Diode-Pumped Solid State laser having an excitation energy of 532 nm.

2.2.5. Ultraviolet-visible spectroscopy (UV-Vis)

Ultraviolet-visible spectroscopy (UV-Vis), also known as absorption spectroscopy, uses mostly ultraviolet and the full spectrum of visible light to measure the wavelength dependent reflection and transmission of materials. Using transmission and reflection, the absorption coefficient of a material can be calculated. It is also possible to find out the band gap of the measured material from the absorption. In this work, reflection and transmission measurements were conducted with a *Perkin Elmer Lambda 1050* UV-Vis setup which has 3 detectors of Photomultiplier tubes (PMT), InGaAs and PbS, to measure across the UV/Vis/NIR range.

The absorption coefficient of the thin film on a semi-infinite transparent substrate is calculated based on equation 2.3 where α is the absorption coefficient, d is the film thickness, R is reflectance and T is the transmittance.[60]

$$\alpha = \frac{1}{d}\ln\left[\frac{(1-R)}{T}\right] \qquad \textit{Eq. 2.3}$$

$$\alpha_{dir} \propto \left(h\nu - E_g\right)^{\frac{1}{2}} \qquad \textit{Eq. 2.4}$$

$$A + R + T = 1 \qquad \textit{Eq. 2.5}$$

One method to obtain the band gap is using absorption coefficient for the calculation of the Tauc band gap by implementing equation 2.4 where $h\nu$ is the photon energy and E_g is the

direct band gap. To estimate the optical band gap value, the value of $(\alpha h\nu)^2$ versus photon energy ($h\nu$) plot is used. The extrapolation of the linear range until the abscissa is plotted and the interception of the extrapolation on the abscissa is taken as the direct band gap of the material.[61] However, the Tauc plot method is a user-dependent approach to obtain the band gap, whose application is still debatable for the accuracy due to the subjective choice of the extent of the linear region. That is why the band gap values in this works are derived from the absorbance (A) which is calculated from the measured transmittance (T) and reflectance (R) (see Eq. 2.5). The maxima of the absorbance derivatives give the band gaps. With this method, the estimated band gap is not affected from the user-defined fitting range of the Tauc plot. This is also a quick method; however, it works quite well for fast estimations of band gaps and it is cross-checked for this material in the literature.[36]

2.2.6. Kelvin-Probe (KP)

The work function (ϕ) and the type of the semiconductor material can be determined by using the Kelvin-Probe setup (see Fig 2.8). To measure the work function, the contact potential difference (V_{CPD}) between the Kelvin-Probe tip and the sample is measured firstly by applying an external bias voltage (V_{dc}) to compensate it according to the equation of $V_{CPD} + V_{dc} = 0$. The obtained V_{CPD} is used to calculate the work function of the sample (ϕ_{sample}) according to $-e.V_{CPD} = \phi_{tip} - \phi_{sample}$, where e is an elemental charge and the value of ϕ_{tip} is known.

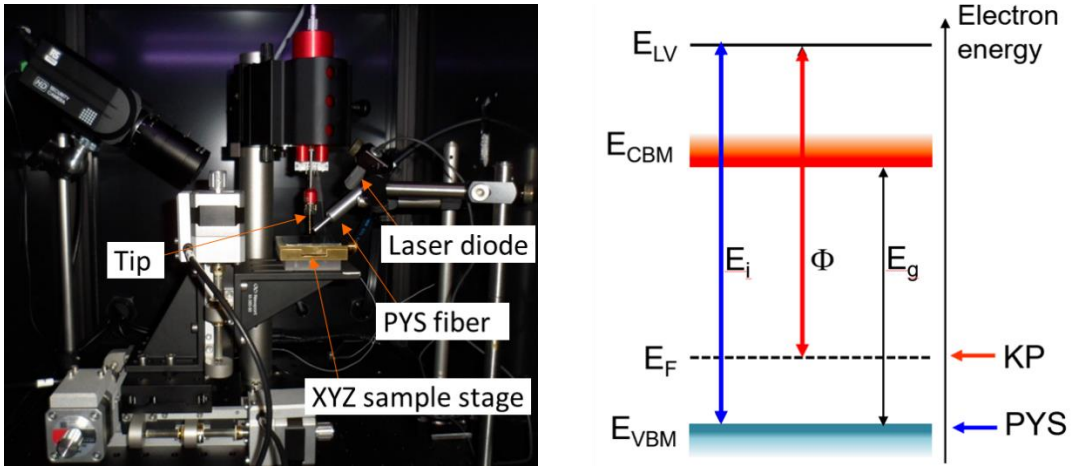

Figure 2.8: The image of the Faraday cage of Kelvin-Probe (KP) and Photoelectron yield spectroscopy (PYS) (left) and the scheme of the measurements (right).

In this study, an ambient-pressure *KP Technology SKP5050-APS02* instrument was used which has a gold-alloyed tip with a 2.0 mm diameter. 532 nm / 2.33 eV laser was used to

illuminate the sample for the surface photovoltage (SPV) measurement. Since Kelvin-Probe measurements were performed by Dr. Marin Rusu, only the results of the measurements are present in this work.

2.2.7. Photoelectron yield spectroscopy (PYS)

The photoelectron yield spectroscopy (PYS) is a method to determine the ionization energy of the measured material to the vacuum level. There are three steps for the PYS measurements: (i) electrons of the material are photoexcited into higher energy states, (ii) excited electrons travel toward the surface, (iii) electrons escape from the surface to vacuum. In the PYS process, the photoelectron yield $Y(\mathrm{h}\nu)$ is measured as a function of photon energy $\mathrm{h}\nu$. In other words, the photoelectron yield is the amount of the photoemitted electrons per incident photon at a given energy $\mathrm{h}\nu$.

$$Y(\mathrm{h}\nu) \propto (\mathrm{h}\nu - E_i)^n \qquad \textit{Eq. 2.6}$$

As the photon energy ($\mathrm{h}\nu$) surpasses and increases the threshold ionization energy (E_i), the photoelectron yield $Y(\mathrm{h}\nu)$ increases as can be seen in Eq. 2.6. The power index is n = 2 for metals, whereas n = 3 for semiconductors. The PYS spectrum also contains the information about the density of states.[62] In this study, a *KP Technology SKP5050-APS02* instrument (see Fig. 2.8) is used which has a deuterium (D_2) lamp equipped with a grating monochromator. The incident photon energy is in the range of 3.4-7.0 eV. Photoelectron yield spectroscopy was conducted by Dr. Marin Rusu. For this reason, limited information about the results is present in this work.

2.2.8. Optical-Pump Terahertz-Probe spectroscopy (OPTP)

OPTP measures the photoconductivity transient and the mobility of photogenerated charge carriers. To photogenerate electrons and holes, laser pulses with a wavelength of 400 nm, a pulse duration of ~150 fs, a repetition rate of 150 kHz and a photon flux per pulse Φ_{laser} of 3.5 x 10^{13} cm^{-2} were used. The conductivity or mobility of these carriers are probed by terahertz pulses (far-infrared light with a photon energy of ~2-10 meV). The pump-induced change in terahertz transmission $\Delta T/T$ is measured by optoelectrical sampling and the sheet photoconductivity $\Delta\sigma_s$ is obtained by the so-called thin film approximation (see Eq. 2.7), which contains the vacuum permittivity ε_0 the speed of light c and the reflective index of the substrate at terahertz frequencies n_{sub}:

$$\Delta\sigma_s = -\varepsilon_0 c(1 + n_{sub})\frac{\Delta T}{T} \qquad \textit{Eq. 2.7}$$

The transient behavior of this conductivity is obtained by delaying the terahertz pulse with respect to the pump pulse. If this conductivity is divided by the induced sheet carrier concentration $\Delta n_s = (1 - R)\Phi_{laser}$ and by the elementary charge, the mobility $\mu_\Sigma = \Delta\sigma_s / q\Delta n_s$ can be read from the initial amplitude. In a slightly modified version, the whole terahertz pulse (not only the maximum amplitude) is measured shortly after photogeneration (here 2 ps). The pump-induced change in terahertz transmission is Fourier-transformed and analyzed again by the thin-film approximation, which yields the mobility spectrum for charge transport at terahertz frequencies. As the same numbers of electrons and holes are photogenerated, it yields the sum of electron mobility and hole mobility. Optical-pump terahertz-probe spectroscopy measurements and evaluations were conducted by Dr. Hannes Hempel. Therefore, the limited details of the measurements and evaluations are presented in this work.

CHAPTER 3
INVESTIGATION OF $BaZrS_3$ PEROVSKITE

The methods developed and described in this work can be used to understand the nature of alkali earth and transition metal perovskites as semiconductor materials. To fulfill the necessary charge balance for perovskites, compounds with the chemical formula of I-II-VII_3, II-IV-VI_3 or III^a-III^b-VI_3 can be used. To classify a material with these formulae as a perovskite material, it has to be in the perovskite structure which needs the corner sharing octahedra. Due to the edge-sharing structure, "the needle-like" configurations with the aforementioned chemical formulae cannot be called "perovskite". However, the necessity of the latter is generally overlooked and these non-perovskite structures are referred to as a "perovskite" anyway in the literature.[43]

The literature survey about $BaZrS_3$ is conducted in chapter 1.3.1. In this chapter, the thin film production method for solution-processed $BaZrS_3$, which is a member of II-IV-VI_3 perovskites, is investigated. After producing the chalcogenide perovskite thin films, the physical and optoelectrical properties were determined to evaluate its potential as a solar cell absorber. These properties are also important to decide about the design of the solar cell architecture. Afterwards, the material is compared with a similar $BaZrS_3$ thin film, which was deposited using pulsed laser deposition and sulfurized in an identical process described in this thesis.[36]

3.1. Preparation of $BaZrS_3$

First, 1.07 mmol of BaI_2 (Santa Cruz Biotechnology, >%98), 3.92 mmol of barium acetate (ACROS Organics, 99+%) are dissolved in a mixture of 3 mL N-N-dimethylformamide (DMF) (Sigma-Aldrich, 99.9%) and 3 mL acetic acid (Sigma-Aldrich, >99.8%) to prepare the molecular ink solution. Then, 1.77 mL of zirconium (IV) acetate solution (Sigma-Aldrich, 4.07 mmol of Zr in dilute acetic acid) are added to the mixture. The final solution is stirred within a glovebox at room temperature for half an hour. A transparent solution is obtained.

For the deposition, quartz substrates are used due to their high glass transition temperatures of ~1200 °C.[52] Before the spin-coating phase, the quartz substrates (1 inch x 1 inch) are rinsed with acetone. This conditions the substrate surface for a better coverage, since acetone is the anti-solvent for acetate compounds. The precursor coating step is implemented after the

substrates have dried in the glovebox. A pipette is filled with 250 µL of the precursor solution to dispense the ink onto the substrate. The dynamic spin-coating is conducted at 1000 rpm for 10 seconds, and then ramped up in 3 seconds to 3500 rpm and continues to spin there for 20 seconds more. 3 repetitions of dynamic dispense spin-coating are performed. In between the spin-coating of layers, the substrates are held at 250 °C for 2 minutes. After the final spin-coating step, the samples are held at 250 °C for 10 minutes, to evaporate the solvent residual.

The spin-coated films are taken out of the glovebox right before sulfurization, to minimize the amount of oxidation, since the sulfur replacement of oxygen needs more energy. To place the samples into the furnace as soon as possible, the samples are put in a quartz boat. After the quartz boat is placed into the middle of the furnace, the quartz tube can be evacuated. The furnace is evacuated at first, then flushed with argon twice to purge out any remaining air, and then flushed with 5% H_2S in argon afterwards. At opening the valve of the exhaust, the flow of sulfurization gas is initiated. The gas inlet is set to 60 sccm of 5% H_2S (± 0.15 Vol %, Air Liquide) in argon. When the flow is established, the furnace is turned on to heat up. The desired sulfurization temperature is set to be reached in 30 minutes. After 30 minutes of sulfurization process, the furnace is left to cool down naturally. When the temperature reaches 400 °C, the gas flow is changed back to pure argon to purge out the residual H_2S in the tube. The samples are collected when room temperature is reached.

3.2. Results and discussions

A series of $BaZrS_3$ thin films with different sulfurization temperatures was fabricated to improve the understanding of the effects of the reaction temperature on the growth mechanism. The structural, compositional, morphological, and, subsequently, optoelectronic properties are investigated in the following part.

3.2.1. Molecular ink preparation route of $BaZrS_3$

Unlike halide perovskites, the preparation of chalcogenide perovskites from their binaries is difficult, since the solubility of metal sulfides are relatively low, and the sulfide binaries are mostly toxic. Hence, the study of the molecular ink preparation has started with searching for the proper compound which can be dissolved easily and deposited onto the substrate with good coverage ratio. After using barium iodide and barium acetate individually and both turning out to have different advantages, a mixture of both was used for the preparation of additional films described in this chapter. As a zirconium source, zirconium (IV) acetate was used for all of the barium sources. In the following sections, the properties of each of these three films will be detailed.

Pure barium acetate as the barium source

Acetate binaries are relatively inexpensive compounds compared to many others since they can be easily produced by reacting metals with acetic acid. While they are highly soluble in aqueous solvents, the direct usage of water as a solvent may cause metal hydroxide formation in some cases.[44] Since metal hydroxides are turning into metal oxides at higher temperatures, which result in oxide perovskite phases, anhydrous dimethylformamide (DMF) is picked as the solvent, which is also a polar solvent like water, and commonly used in the production of halide perovskites.

On the other hand, the easy solubility of acetate compounds is also the disadvantage of the material deposition via spin coating since the coated layer dissolves easily when multiple subsequent deposition cycles are needed. In this case, the coverage was poor (see Fig. 3.1, right) on the cm-scale. The reason of having a poor coverage is the surface interaction between the substrate and the solution which might not be good enough to remain on some areas of it.

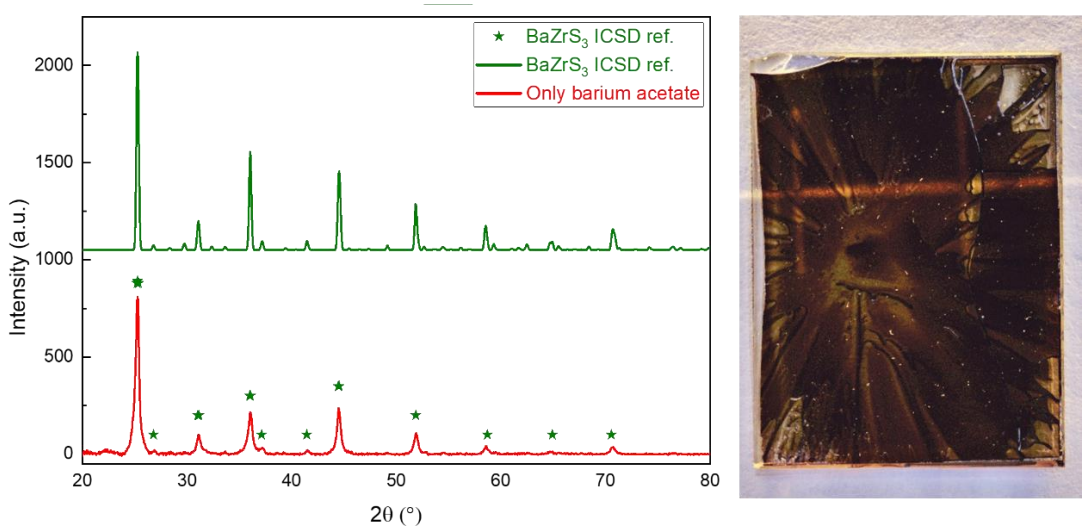

Figure 3.1: Comparison of the XRD patterns (left) of $BaZrS_3$ thin film which uses barium acetate as barium source (red) and the ICSD reference of $BaZrS_3$ powder (ICSD-23288) (green). Image of the sulfurized $BaZrS_3$ thin film produced with only acetate compounds (right).

Concentrations of the solutions affect the viscosity and consequently the thickness of the spin-coated thin films. During the solution preparation, the maximum solubility amount of the binary compounds at room temperature is reached. Increasing the solvent temperature could increase the solubility as well to have thicker solution, since the dissolution processes of the compounds used in this work are endothermic. However, a temperature study was not

conducted for the solution temperature at this point to keep the reproducibility of the work higher. Despite the poor coverage, an XRD measurement was performed to assess the material phase. The XRD measurement reveals that, the precursor material formed the distorted perovskite structure successfully after the sulfurization step as it can be seen in Fig. 3.1. The diffractogram of $BaZrS_3$ powder reference from the Inorganic Crystal Structure Database (ICSD) are used for the indexation of X-ray diffractograms. It can be seen that the produced film does not have a preferred orientation since the most prominent XRD peaks of the film and the powder are at the same peak position. These results revealed that barium acetate is a promising binary, however, it needs to be stabilized for a better coverage.

Pure barium iodide as the barium source

In the literature, mixing only a small amount of pure iodine to sulfide binary precursors increases the reaction kinetic of the perovskite formation and decreases the reaction duration from a week to couple of hours.[31] However, due to the relatively low boiling temperature of iodine (184.3 °C), addition of iodine as powder would not be more practical than adding the iodide compound of barium. The $BaZrS_3$ thin film produced from barium iodide here has the same peak positions as well as the one produced from barium acetate. Using only barium iodide instead of barium acetate helped to improve the coverage (see Fig. 3.2) and the thickness subsequently due to accumulation of layers on each spin-coating cycle.

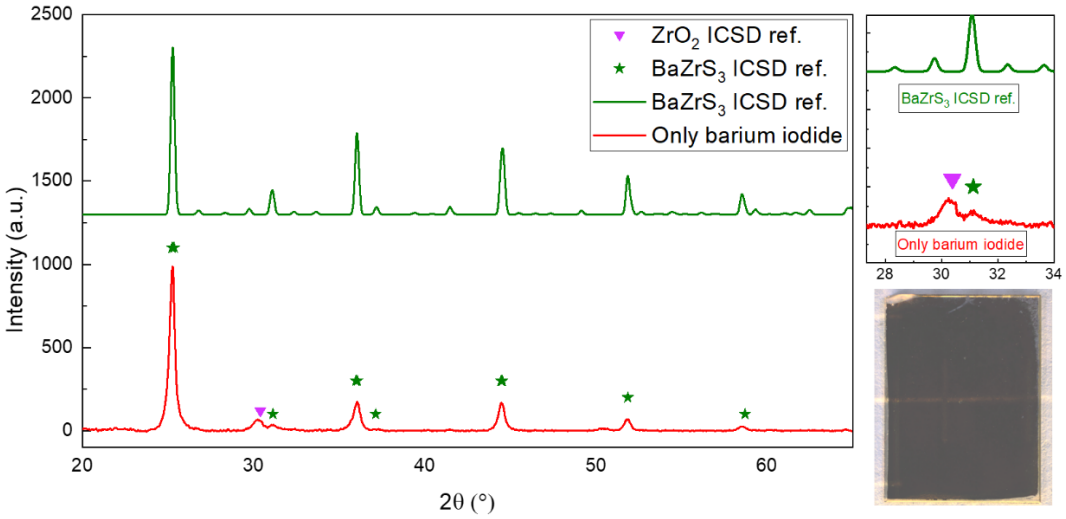

Figure 3.2: Comparison of the XRD patterns of $BaZrS_3$ thin film which uses barium iodide as barium source (red) and the ICSD reference of $BaZrS_3$ (green, ICSD-23288) (left). Magnification of the zirconium (IV) oxide impurity peak (magenta triangle, ICSD-41011) (top right). Image of the sulfurized $BaZrS_3$ thin film produced with only barium iodide as a barium source (bottom right).

However, using only iodide binaries as it is done in halide perovskites did not result in the desired perovskite structure without impurities and secondary phases, since the zirconium could not be fully sulfurized. This resulted in a zirconium (IV) oxide impurity, which can be seen by the reflection at 30° in the X-ray diffractogram in Fig. 3.2. The high amount of iodide ions might interact with zirconium as well which formed an oxide phase impurity later, whereas it is not a significant problem in the mixed iodide-acetate solution.

Mixed barium acetate and barium iodide compounds

In order to achieve a better coverage with good morphological properties and without a secondary phase, small amount of barium iodide binary was mixed to the barium acetate. The optimum amount for barium iodide was determined as ~20 %(at) empirically. And in the case of mixed barium acetate and barium iodide, it is observed in the SEM images (see Fig. 3.3) that the coverage of the film is better than for the ones with only barium iodide or only barium acetate.

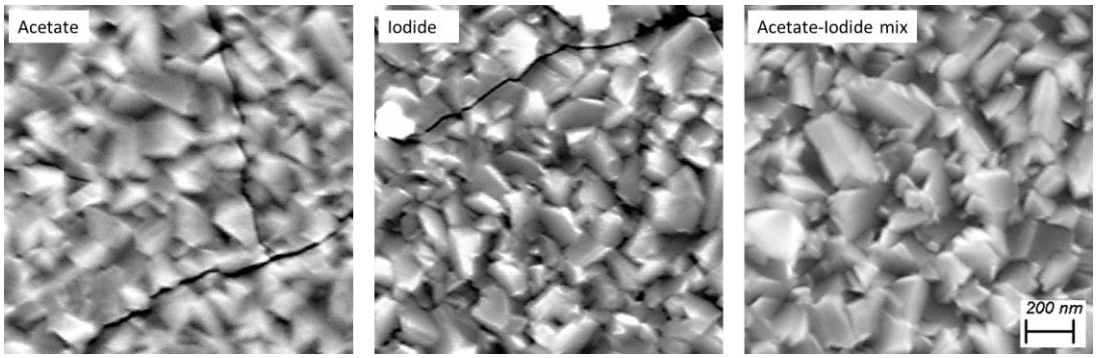

Figure 3.3: Comparison of the SEM images of the $BaZrS_3$ thin films which use different barium compounds. The scale applies to all images.

The bigger grain size for the one prepared by the acetate-iodide mixture can be observed on the SEM images which can also be seen as an increase in the peak intensity of the XRD patterns in Fig. 3.4. The GI-XRD measurements were performed with the same instrument configuration and for the same duration for all the samples presented here. The stronger XRD intensity of acetate-iodide mixture sample shows better crystallinity over the other samples as it confirms the SEM images.

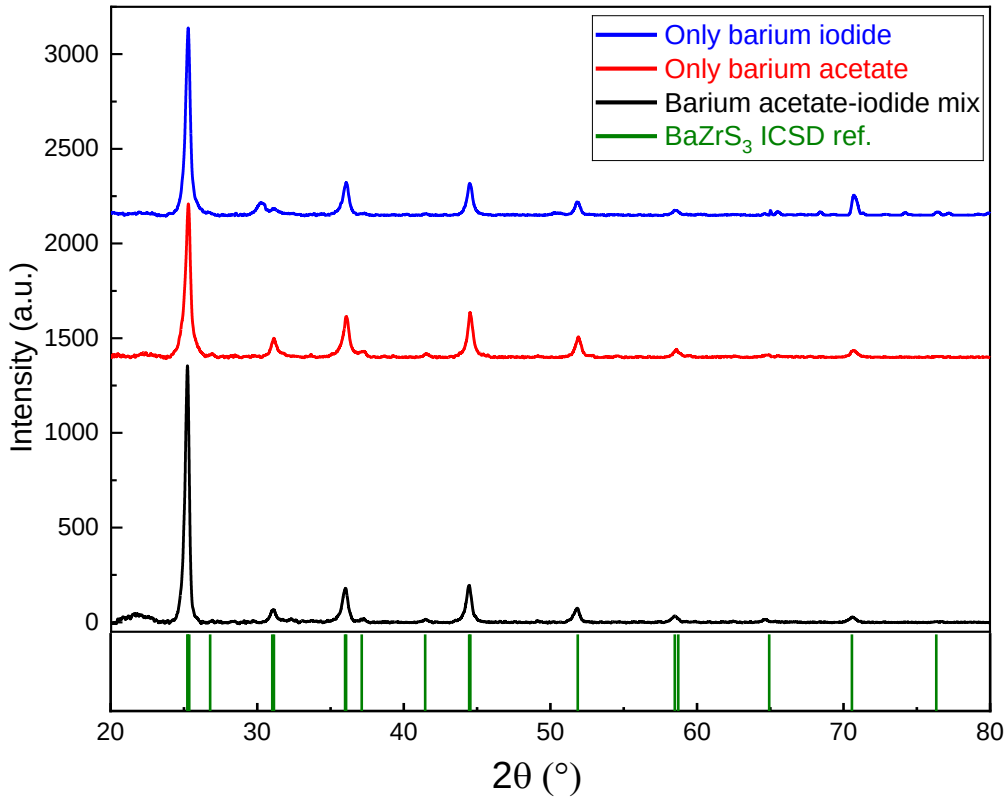

Figure 3.4: Comparison of the XRD patterns of the $BaZrS_3$ thin films which use different barium compounds: Barium iodide (blue), barium acetate (red), mixture of barium acetate and barium iodide (black) and the ICSD reference of $BaZrS_3$ (green, ICSD-23288).

The previously reported solution-processed works used polyvinyl butyral in their solutions to improve the coverage in the case that they used only barium acetate as a barium source.[34,37] Polyvinyl butyral is a resin based binding material which decomposes into aromatic components at 260-380 °C.[63] It is likely that annealing the samples to form $BaZrO_3$ was performed to eliminate these aromatic residuals from the film. And due to the high-solubility of this binding material in nonpolar solvents, propionic acid was used as a solvent in the aforementioned works. However, since the nonpolar side of the propionic acid limits the solubility of the acetate compounds, the solutions were prepared at the temperature of 60 °C which is a clear disadvantage compared to the solution processing performed at room temperature in this work. The advantage of mixing the two compounds of barium here is advancing the solubility of materials by eliminating the common ion effect at room temperature. Due to higher solubility of different compounds in the same solvent, it is possible to reach higher thickness values even after less spin-coating cycles which improves the film quality.

With the results of these experiments, it is decided to focus on the partial usage of iodide compounds as a part of the ink-preparation for chalcogenide perovskite productions. In the

rest of the chapter, it is investigated how the changes of other parameters affect the formation of the perovskite structure.

3.2.2. Elemental composition and crystal structure of $BaZrS_3$

The elemental composition is one of the most important parameters for the reaction processes, in order to prevent secondary phases and impurities which cause defects in materials. The elemental compositions of the materials are determined by XRF. Although the elemental Ba:Zr ratio of the solution is approximately 1.25:1 according to the molecular ink recipe, it is seen that the elemental ratio of the deposited material is 1:1.02 (see Table 3.1). This might be related to the interactions between the material and the substrate. During spin-coating, some of the barium acetate might not stay on the substrate due to low surface interactions. Hence, for different deposition conditions or methods, the stoichiometry of the solvent should be modified.

X-ray fluorescence (XRF) analysis shows that the films were sulfurized to the high degree at 900 °C and above. For the 800 °C sample and below, the elemental stoichiometry is as sulfur deficient as 1:1:2. Starting from the annealing temperature of 900 °C, the elemental stoichiometry is close to the perovskite structure stoichiometry of 1:1:3. However, XRD measurements are needed to see if the samples formed the perovskite or remained just as sulfurized binaries. The elemental composition and thickness of the thin films with annealing temperatures of 800 °C, 900 °C, 950 °C, 1000 °C and 1100 °C are shown in in Table 3.1.

Table 3.1: Elemental composition, thickness and band gap for thin films at various sulfurization temperatures between 900 and 1100 °C. Ba:Zr shows the cation ratio on the precursor films before the sulfurization. Ba:Zr:S indicates the elemental ratio after sulfurization at given temperature. The derivative of the absorbance for each film was used to calculate the band gap (E_g) values.

Sulfurization temperature (°C)	**Precursor Ba:Zr (molar %)**	**Sulfurized Ba:Zr:S (molar %)**	**Ba-Zr-S_3 sulfurized thickness (nm)**	**Band gap (eV)**
800	1:0.95	1:0.98:2.06	~240	-
900	1:1.02	1:1.02:2.81	~500	2.16
950	1:1.02	1:1.03:3	~450	2.12
1000	1:1.02	1:1.03:3.13	~450	2.02
1100	1:1.02	1:1.03:2.97	~500	2.01

The XRF analysis also revealed that the Ba:Zr ratio did not change significantly after sulfurization, which means none of these cations and their possible compounds is volatile at such temperatures (see Table 3.1). The volatility of components can be major problem for some thin film technologies (*i.e.* tin loss in kesterites).[20] On the other hand, the transparent color of the precursor turns into a brown color which is a clear sign that the crystal structure and composition of the material has changed (see Fig. 3.5).

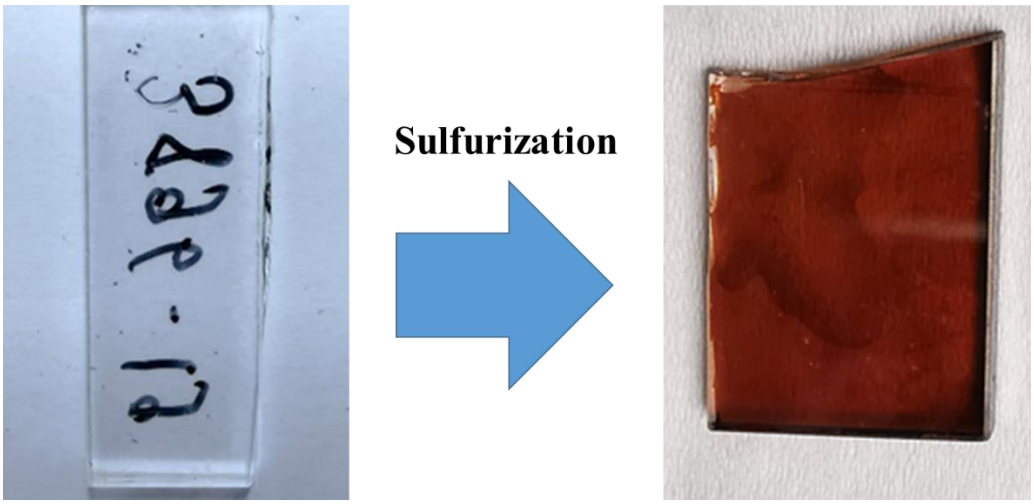

Figure 3.5: Photographic image of a film before sulfurization (left) and after sulfurization ($BaZrS_3$) (right) at 1000 °C for 30 minutes.

The XRF instrument used in this work is not able to measure oxygen. Due to the same reason, Marquez *et al.* calculated the oxygen content by using charge neutrality from the measured sulfur content and the calculations matches the results of the RBS measurements.[36] Since the elemental composition of the films investigated in the present study agreed with the perovskite ratio (see Table 3.1), it is assumed that there is no significant amount of oxide component in these films. However, measuring with XRD could reveal oxide phases in the material structure.

For depth related structure changes, the grazing incidence X-ray diffraction (GI-XRD) was performed for the incidence angles of 0.5, 1, 1.5 and 2° (see Fig. 3.6). As the grazing incidence angle increases, the depth of measurement increases which gives an idea about the homogeneity of the bulk. It is known that several surface layers might have a different compositions than the bulk due to the vacancies and adatoms on the surface.[64] And since the grazing incidence angle of 0.5° gives different values for the lattice parameters compared to the bulk, the grazing incidence angles bigger than 0.5° are picked. On the other hand, a bigger grazing incidence angle might cause measuring the substrate if the sample is not thick enough.

For these reasons, the grazing incidence angle of 1° for the GI-XRD measurements is determined. As can be seen in Fig. 3.6, the lattice parameters do not change significantly above 0.5°, which means the composition does not change significantly with depth. In other words, the sulfurization reaction did not occur only on the surface.

Angle	$BaZrS_3$ sulfurized at 1000°C					
	a (Å)	±	*b* (Å)	±	*c* (Å)	±
0.5°	7.059	0.001	9.986	0.001	7.004	0.001
1°	7.074	0.001	9.994	0.001	7.002	0.001
1.5°	7.078	0.001	9.998	0.001	7.003	0.001
2°	7.078	0.001	9.998	0.001	7.002	0.001

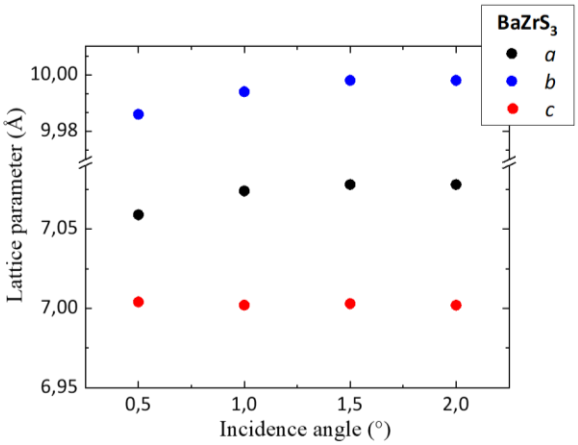

Figure 3.6: Dependence of lattice parameters obtained by Le Bail analysis on the depth via the incidence angle changing.

The X-ray diffraction patterns in Fig. 3.7 show that all the prominent peaks of the orthorhombic $BaZrS_3$-structure (space group *Pnma* #62) are present on the measured diffractograms, which are sulfurized at the annealing temperatures starting from 900 °C. The peaks are not distinguishable from the background noise for the samples annealed below 900 °C. And the peaks get broader as the annealing temperature decreases indicating a poorer crystallinity for the lower annealing temperature.

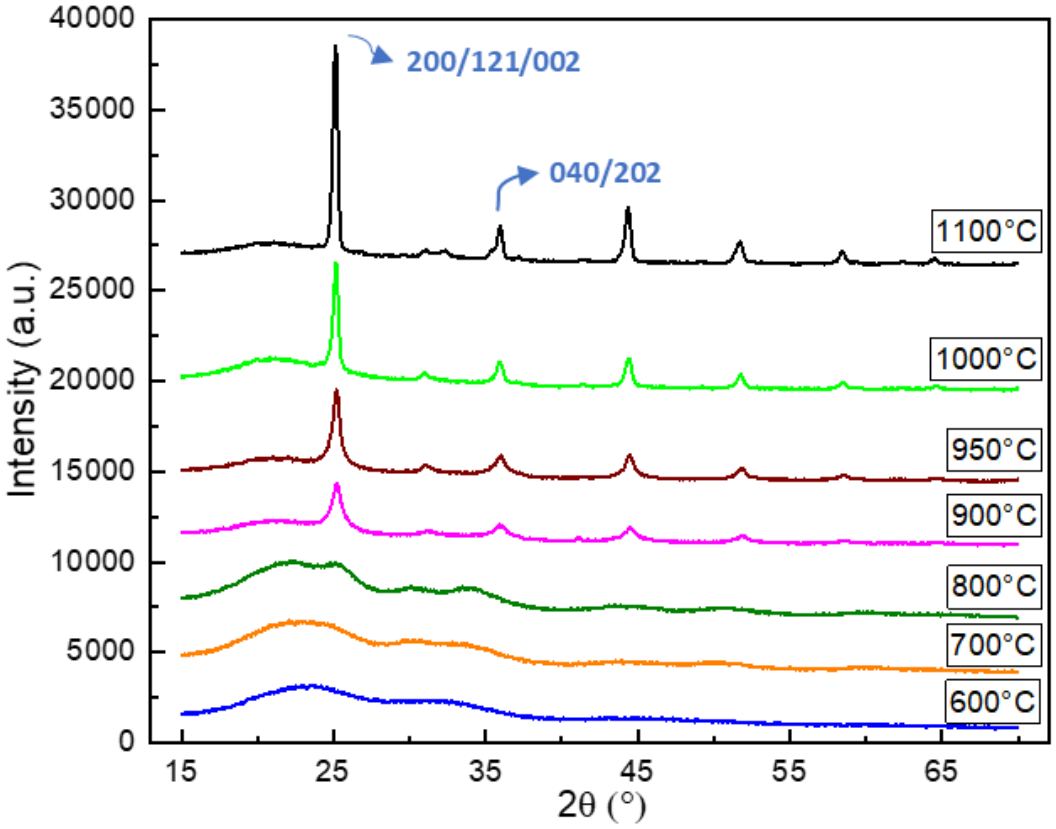

Figure 3.7: Grazing incidence X-ray diffraction patterns with 1° incidence angles of $BaZrS_3$ thin films sulfurized from 600 °C to 1100 °C.

In the case of the $BaZrS_3$ sulfurized from PLD-deposited $BaZrO_3$ of Marquez *et al.*, the 110 Bragg peak of $BaZrO_3$ (space group $Pm\bar{3}m$) is visible for the annealing temperatures of above 1000 °C (see chapter 3.2.6).[36] However, no XRD-peaks for oxide phases or binaries were observed on the films synthesized by solution processing. Moreover, the dependence of crystallinity on annealing temperature can be described in Fig. 3.8 with the full width at half maximum (FWHM) obtained from the Le Bail analysis. The increasing crystallinity with the increasing sulfurization temperature can be seen on both peaks of the materials produced by solution processing. There is no significant increase above the sulfurization temperature of 1000 °C, which is one of the reasons for picking 1000 °C as the optimum temperature for the following measurements.

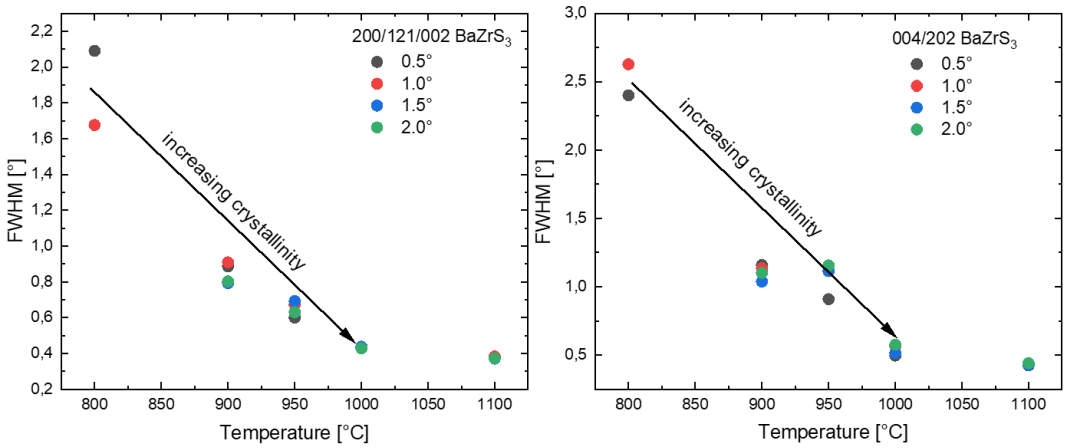

Figure 3.8: Le Bail analysis for the crystallinity of the 200/121/002 peaks (left) and 004/202 peaks (right) for various sulfurization temperatures from 600 °C to 1100 °C.

XRD measurements also revealed that a trace amount of $Ba_4Zr_3S_{10}$ is present in the film, which is a member of the Ruddlesden-Popper phases.[65–68] This is another reason for not going above 1000 °C for the $BaZrS_3$ synthesis, since it shows up on the sample sulfurized at 1100 °C as it can be seen in Fig. 3.9. There are multiple peaks from this phase visible. And some are overlapping with the intended product.

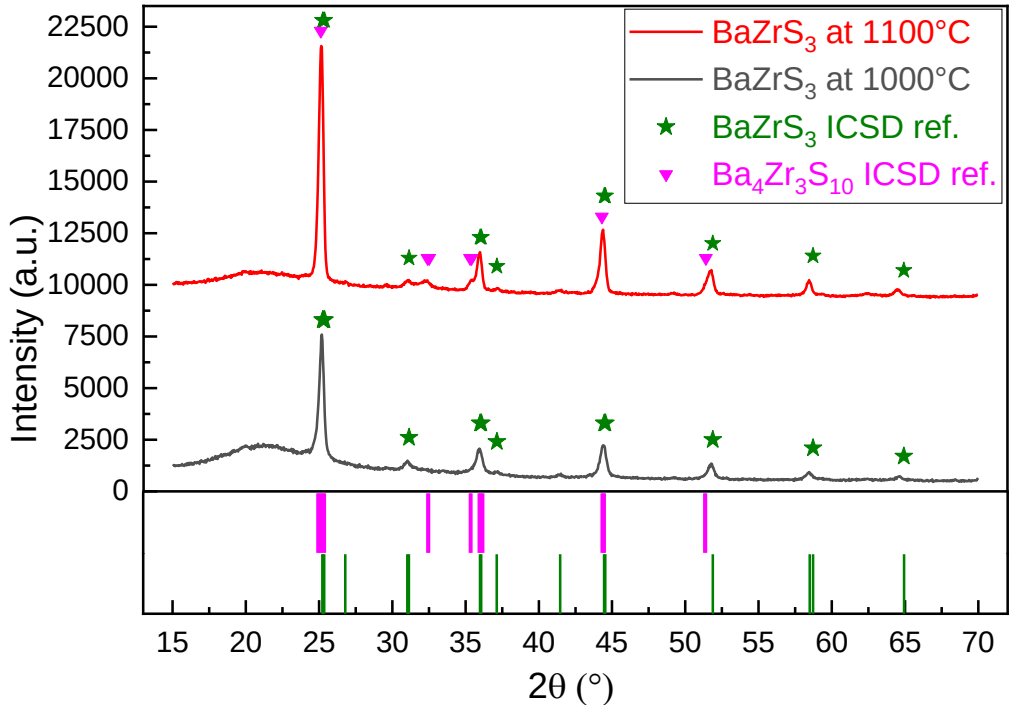

Figure 3.9: Indexation of the samples sulfurized at 1000 and 1100 °C with the reference from the Inorganic Crystal Structure Database (ICSD) for BaZrS3 (green, ICSD-23288) and Ba4Zr3S10 (magenta, ICSD-72656).

For $BaZrS_3$ powder, the 121 Bragg peak is the strongest one. Close to the 121 peak, 200 and 002 peaks occur as well at around 25°, and they cannot be resolved. In case of statistical orientation of $BaZrS_3$ grains, if the integral intensity of the 040/202 peak at around 36° to the integral intensity of the 200/121/002 peak ratio is higher than one, there is a preferred orientation in the film. This is the case for the films produced by the pulsed laser deposition (PLD) technique (see chapter 3.2.6).[36] However, since the most prominent peaks of the powder reference and the films produced by solution processing are at the same peak position, there is no-preferred orientation for the solution processed films.

To cross reference the results on morphology, Raman measurement were conducted as well. Figure 3.10 shows the Raman spectra of the $BaZrS_3$ films. The intensities of the peaks increase as the sulfurization temperature increases due to the decrease in anharmonic thermal phonon-decay.[30] The assignment of the peak modes is done according to the paper of Perera *et al.*, in that the produced $BaZrS_3$ is reported as a pure phase.[30] At temperatures above a 1000 °C an additional mode at around 350 cm^{-1} is observed. The appearance of this peak coincides with the formation of the $Ba_4Zr_3S_{10}$ phase as observed in the XRD results. Thus, it is likely that this peak at around 345 cm^{-1} can be attributed to this phase, however there is no literature available to corroborate.

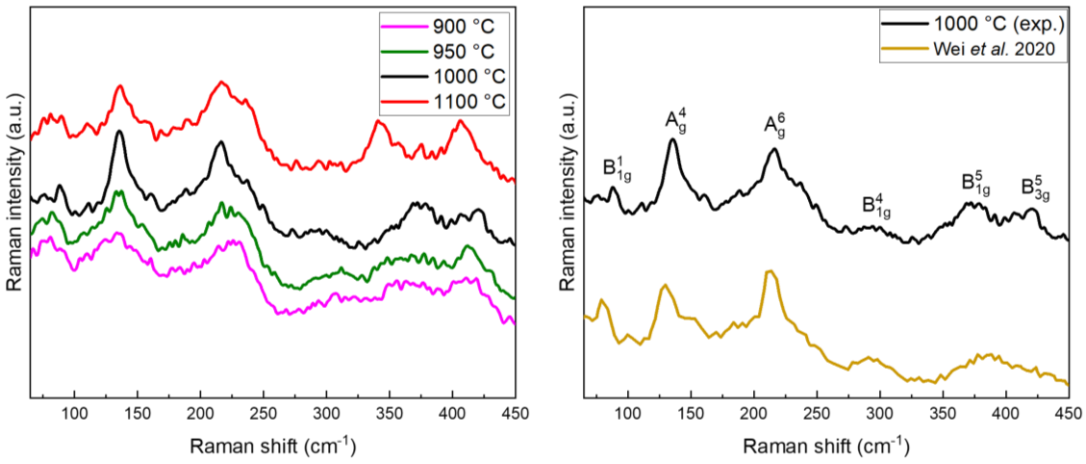

Figure 3.10: Raman spectra of $BaZrS_3$ (Left) measured at the room temperature for the films sulfurized at 900 °C (magenta), 950 °C (green), 1000 °C (black) and 1100 °C (red). Comparison of the films (right) sulfurized at 1000 °C (black) and the replotted data from Wei *et al.* (2020) for the film sputtered and then annealed at 1050 °C (gold, replotted with permission).[35]

On the right side of the Fig. 3.10, the modes of the film sulfurized at 1000 °C can be seen with the comparison of the Wei *et al.* publication.[35] The indexation of the modes were done according to this paper.

Scanning electron microscopy (SEM) images show that the grain size increases as the sulfurization temperature increases (see Fig. 3.11). At 900 °C, the crystallite size was less than 200 nm whereas the size reached 200 nm at 950 °C. And it increased to around 1 µm at 1100 °C, which might be caused by the formation of $Ba_4Zr_3S_{10}$ crystals as well since the increase in the crystallite size is in great agreement with the XRD result.

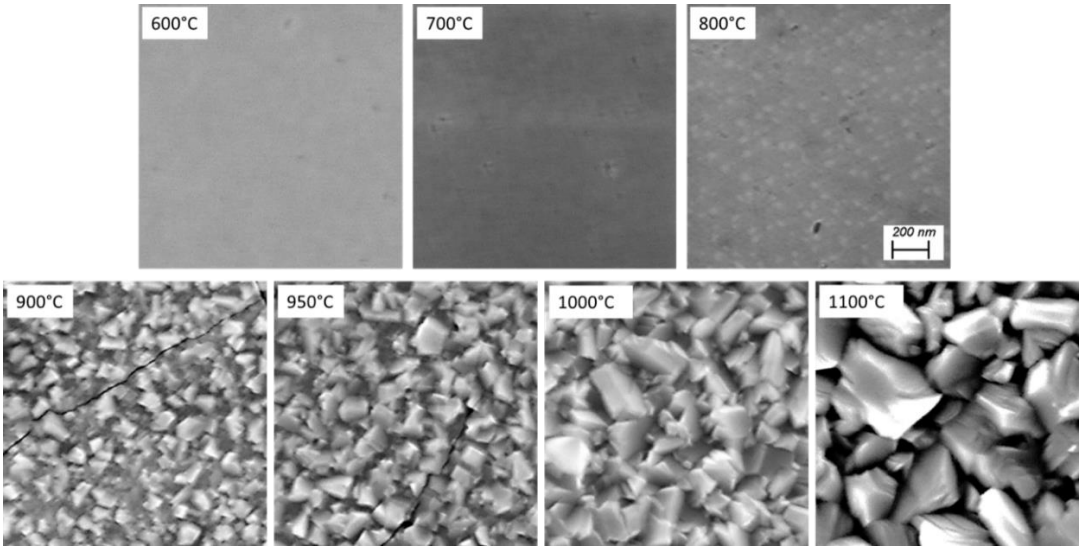

Figure 3.11: Scanning electron microscopy (SEM) in-Lens secondary electron detector images of the thin films for the sulfurization temperatures from 600 °C to 1100 °C, respectively. The scale applies to all images.

3.2.3. Optoelectronic properties of $BaZrS_3$

For the calculation of absorbance, transmittance and reflectance were measured with the UV-Vis spectroscopy. The calculation of the absorbance and the band gap values are explained in chapter 2.2.5. As it can be seen in Fig. 3.12, the band gap energy decreases, as the sulfurization temperature increases. However, there is a secondary phase formation at 1100 °C, which makes 1000 °C optimal for producing a single-phase material.

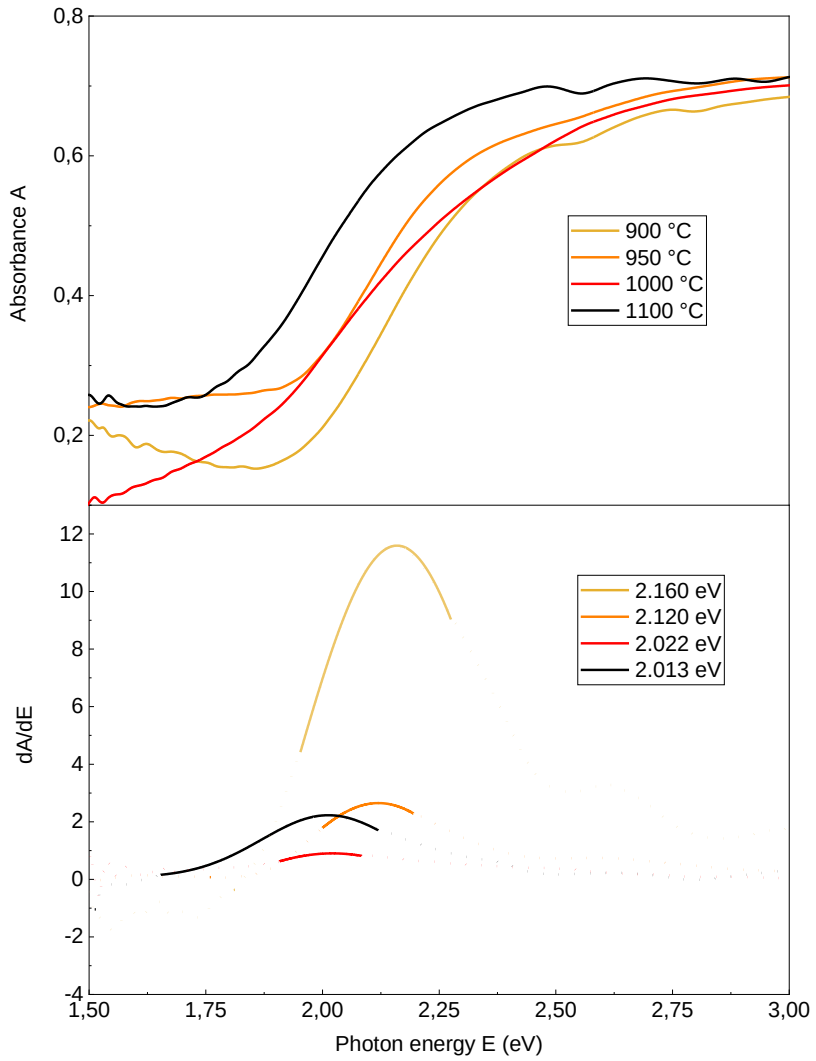

Figure 3.12: Absorbance for the films (top), which are sulfurized at 900 °C (gold), 950 °C (orange), 1000 °C (red) and 1100 °C (black). The derivative of the absorbance (dotted) and their Gaussian fits (line) are used for the determination of the band gap energy values of the films (bottom). The maxima of the fits estimate the band gaps, and the dots represent the measurement steps.

In Fig. 3.12, the derivatives of the absorbance can be seen as dots. And the inflection points of the absorbance determine the band gaps. In order to find the exact maxima in between the measurement steps, a Gaussian fit is used which shows that the band gap is around 2 eV for the materials produced in this work.

Kelvin-Probe (KP) measurements were performed to measure the work function and the surface photovoltage of the film sulfurized at 1000 °C (see Fig. 3.13) under nitrogen atmosphere. The samples were illuminated by a 532 nm laser. The work function was measured as around 4.3 eV. And the change in the work function under an illumination gives the surface photovoltage. The negative value of the surface photovoltage shows that the film is an n-type material.

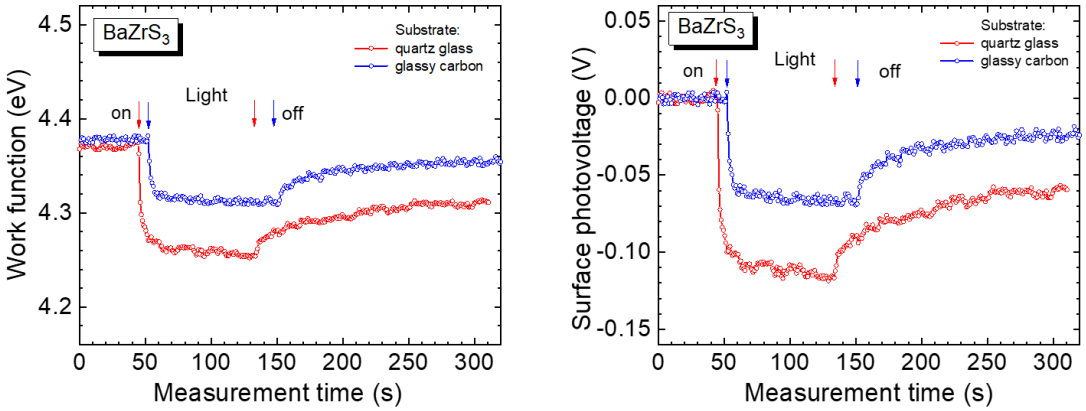

Figure 3.13: The work function and the surface photovoltage of the films sulfurized at 1000 °C on quartz glass and glassy carbon substrates.

The ionization energy and the density of states (DOS) were measured for the film sulfurized at 1000 °C by Photoelectron Yield Spectroscopy (PYS) also in nitrogen atmosphere by using the derivative of the photoemission current. The measurement was not conducted for this material after 6.8 eV as can be seen Fig. 3.14. Thus, the trend of DOS after that point is unknown.

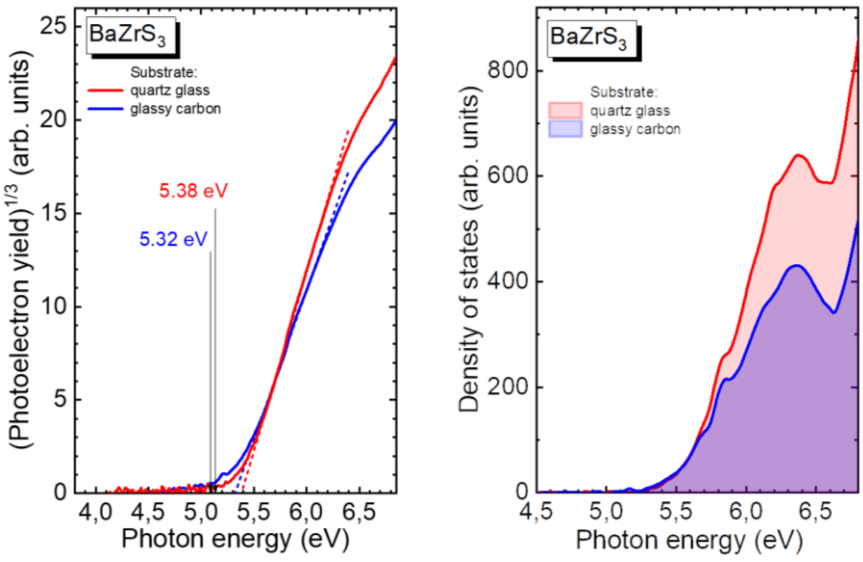

Figure 3.14: Ionization energy (E_i) and density of states (DOS) of the films sulfurized at 1000 °C on quartz glass and glassy carbon substrates.

KP and PYS measurements show that the solution-processed $BaZrS_3$ material has ~5.35 eV ionization energy as can be seen in Table 3.2. To conduct KP and PYS measurements, the

material is deposited on both quartz and glassy carbon substrates, which gave comparable results.

Table 3.2: Contact potential difference (CPD), surface photovoltage (SPV), work function (ϕ), ionization energy (E_i) and the energy difference between the Fermi level and the valance band maximum (E_F-E_{vbm}) of $BaZrS_3$ sulfurized at 1000 °C.

Sample	Surface cond.	CPD (± 2 mV)		SPV (± 3 mV)	Φ (± 0.04 eV)		E_i (± 0.03 eV)	E_F - E_{VBM} (± 0.05 eV)	
		dark	light		dark	light		dark	light
$BaZrS_3$/Quartz Glass	air-exp.	-270	-385	-115	4.37	4.26	5.38	-1.01	-1.13
$BaZrS_3$/Glassy Carb.	air-exp.	-263	-329	-66	4.38	4.31	5.32	-0.94	-1.01

The dynamics of photogenerated charge carriers are investigated by Optical-Pump Terahertz-Probe spectroscopy (OPTP) (see chapter 2.2.8), which obtains photoconductivity transient $\Delta\sigma_\mu$. This photoconductivity $\Delta\sigma_\mu = \Delta\sigma/q\Delta n_0$ is divided by the elementary charge q and by the initially photogenerated carrier concentration Δn_0, which allows to read the sum of electron mobility and hole mobility μ_Σ from its initial amplitude. Hence, it has units of a mobility [$cm^2V^{-1}s^{-1}$] but its decay still corresponds to a transient photoconductivity and can therefore be caused by trapping (a mobility decay) or recombination (a decay of the carrier concentration).

2 ps after photogeneration, the sum of electron and hole mobility was measured frequency-resolved. Such mobility spectra are shown in Figure 3.15 for sulfurization temperature between 800 °C and 1100 °C.

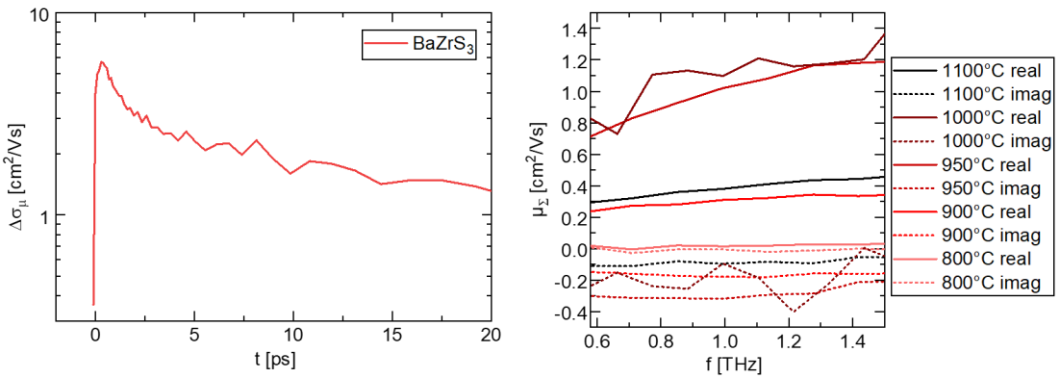

Figure 3.15: Photoconductivity transients of ink-based $BaZrS_3$ sulfurized at 1000 °C (left) and mobility spectra at terahertz frequencies for different sulfurization temperatures (right). The negative imaginary part indicates partial charge carrier localization.

The highest mobilities are obtained for 1000 °C and 950 °C, which therefore should allow the best charge carrier extraction in a potential solar cell. For higher and lower temperatures, the mobility decreases significantly. For 800 °C, it is below the resolution of ~0.02 $cm^2V^{-1}s^{-1}$. The imaginary part, which is shown in Figure 3.15 as dotted line, is slightly negative. Such behavior indicates charge carrier localization and is likely connected to the fast-trapping process within the first ps.

3.2.4. Comparison of PLD and solution-processed samples

PLD is an expensive deposition technique which makes preparation of high-quality thin films possible. On the other hand, spin coating is a low-cost process which has a disadvantage on reproducibility of the coatings. And a significant advantage however is the easy transition to large area deposition via ink jet printing. In this part, the products of both processes are investigated. The XRD patterns are compared for the various sulfurization temperatures. In the case of the PLD-processed $BaZrS_3$-sulfurization from its ternary oxide, the 110 Bragg peak of $BaZrO_3$ (space group $Pm\bar{3}m$) is reported around 30° for the annealing temperatures of over 1000 °C as can be seen in Fig. 3.16. This is not observed in the solution-processed samples since $BaZrS_3$ production did not include any step of $BaZrO_3$ formation which is also the novelty of this work compared to the solution-processing works reported before.[34,37]

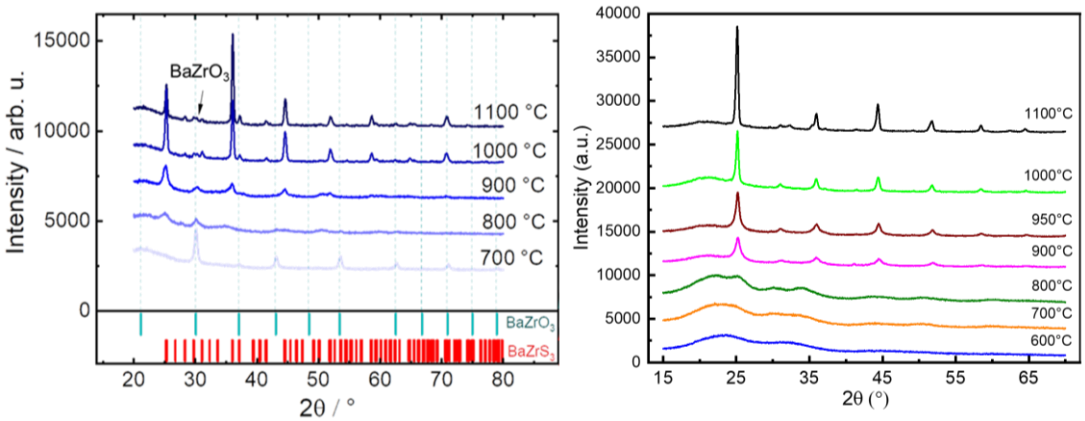

Figure 3.16: Comparison of the XRD patterns for the samples produced by PLD technique (left, reprinted with permission from: Márquez *et al.*, '$BaZrS_3$ Chalcogenide Perovskite Thin Films by H_2S Sulfurization of Oxide Precursors', Copyright 2021 American Chemical Society.) and the solution-processed deposition technique (right).

Since commonly bigger grains result in improved optoelectronic parameters of a material, the impact of the sulfurization temperature on the crystallinity is investigated by XRD. FWHM values of XRD measurements are important parameters to obtain information about crystallinity. The integral intensity is the ratio of the selected peak from the material to the peak at the position of the most prominent peak in the powder reference sample. The integral intensity gives an information about the crystal orientation. Since the selected peak is divided by the most prominent peak, the results lower than one means no preferred orientation. If this ratio of these two peaks is bigger than one, it means the crystal has a preferred orientation to the direction of the selected peak. The 121, 200 and 002 peaks at around 24° are used together as the strongest peak in its powder diffractogram, since they overlap and cannot be resolved. In the case of the PLD processed sample, the integral intensity of the 040/202 peak at around 36° to the 121, 200 and 002 peak is higher than 1, whereas the solution-processed one has an integral intensity lower than one similar to the powder reference one since the 121, 200 and 002 peak is the most prominent peak. Increase in the FWHM as the sulfurization temperature shows (see Fig. 3.17) that both materials produced in two different method have a high temperature requirement for perovskite formation.

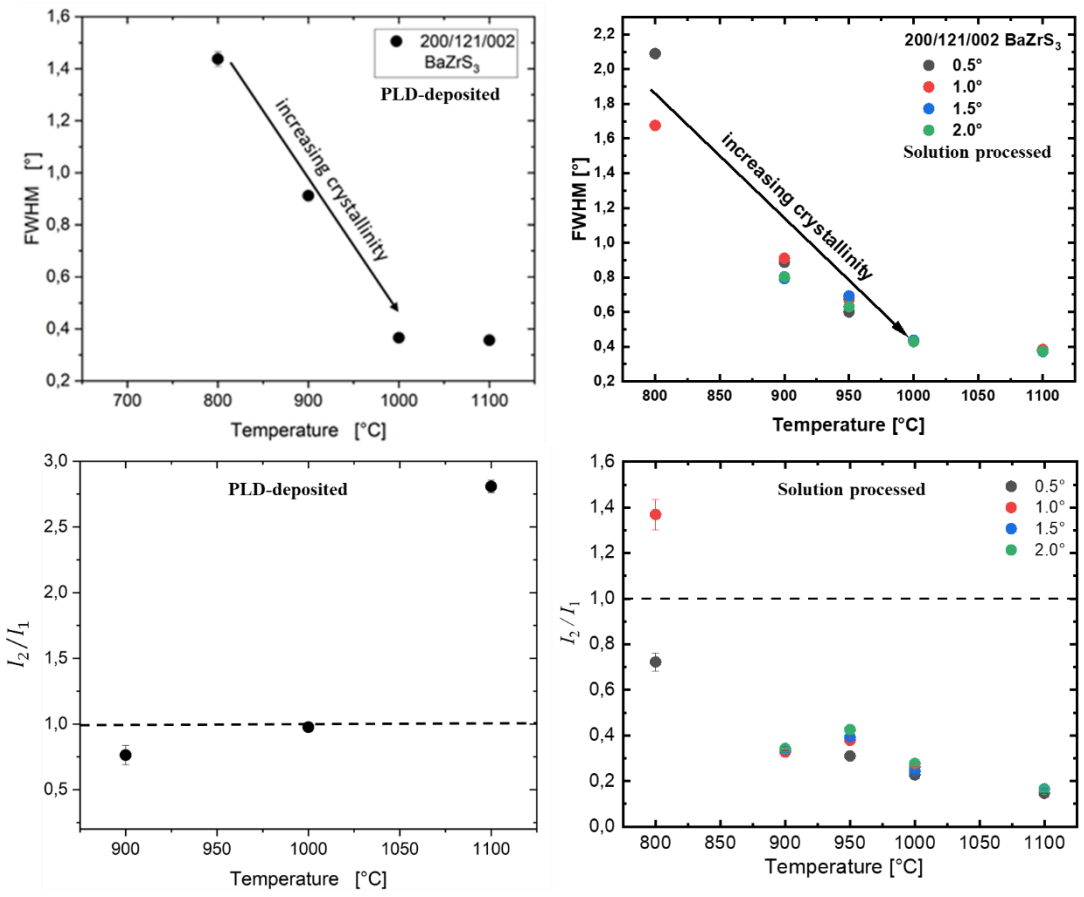

Figure 3.17: Crystallinity comparisons of PLD processed (top left, reprinted with permission from: Márquez *et al.*, 'BaZrS$_3$ Chalcogenide Perovskite Thin Films by H$_2$S Sulfurization of Oxide Precursors', Copyright

2021 American Chemical Society.) and solution-processed (top right) $BaZrS_3$ for various sulfurization temperatures by using the full width at half maximums (FWHM) of the given peaks in the legend. The solution-processed sample is measured for different grazing incidence angles, whereas PLD one is measured at 1° grazing incidence angle. Integral intensity (I_2/I_1) comparisons of PLD deposited (bottom left, reprinted with permission from: Márquez *et al.*, '$BaZrS_3$ Chalcogenide Perovskite Thin Films by H_2S Sulfurization of Oxide Precursors', Copyright 2021 American Chemical Society.) and solution-processed (bottom right) $BaZrS_3$ to determine the preferred orientations of the crystal.

After the morphological comparison, the comparisons of the optical measurements were performed. An estimation is done for the band gap by using the derivation method of the absorbance as described in chapter 2.2.5. Due to the lack of sulfur replacement at lower temperatures, PLD processed samples have higher band gaps until reaching considerable amounts of sulfur at 1000 °C as can be seen in Fig. 3.18. It is likely that the high amount of sulfurization is obtained due to easier acetate replacements of solution-processed samples which results in lower band gaps. This shows that using acetate compounds instead of oxide compounds is more promising for the low temperature production of this material since the band gaps are comparable for the high reaction temperature of 1000 °C for both processes in the end.

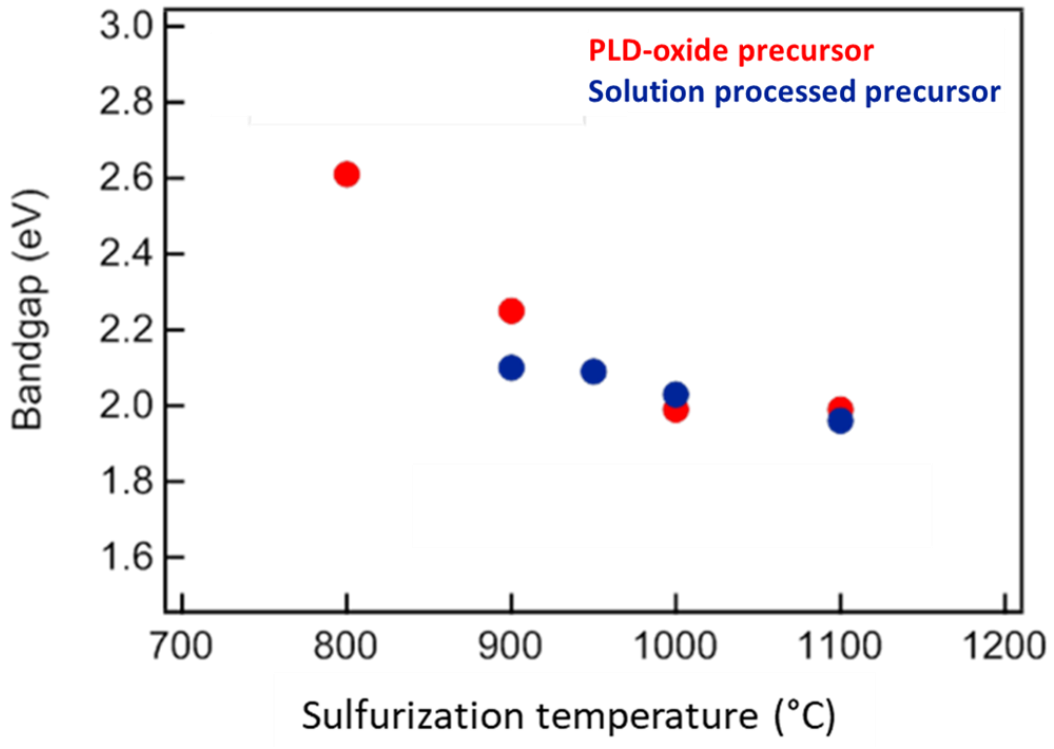

Figure 3.18: Band gap comparison of the $BaZrS_3$ samples produced by PLD (red, reproduced with permission from: Márquez *et al.*, '$BaZrS_3$ Chalcogenide Perovskite Thin Films by H_2S Sulfurization of Oxide Precursors', Copyright 2021 American Chemical Society.) and solution process (blue) at various sulfurization temperatures.

Figure 3.19 shows the photoconductivity transients of the ink-based $BaZrS_3$ that was annealed in H_2S at 1000 °C and compares it with the previous results for $BaZrS_3$ that was sulfurized in the same way and at the same temperature from PLD grown $BaZrO_3$.[36] The mobility (initial amplitude) of the ink-based $BaZrS_3$ of 2.4 $cm^2V^{-1}s^{-1}$ is slightly larger than for the PLD-based $BaZrS_3$ of 2.1 $cm^2V^{-1}s^{-1}$, but this variation is within the uncertainty of repetitive measurements. Also, the trapping and recombination kinetics are rather similar for the sample fabricated with both processes.

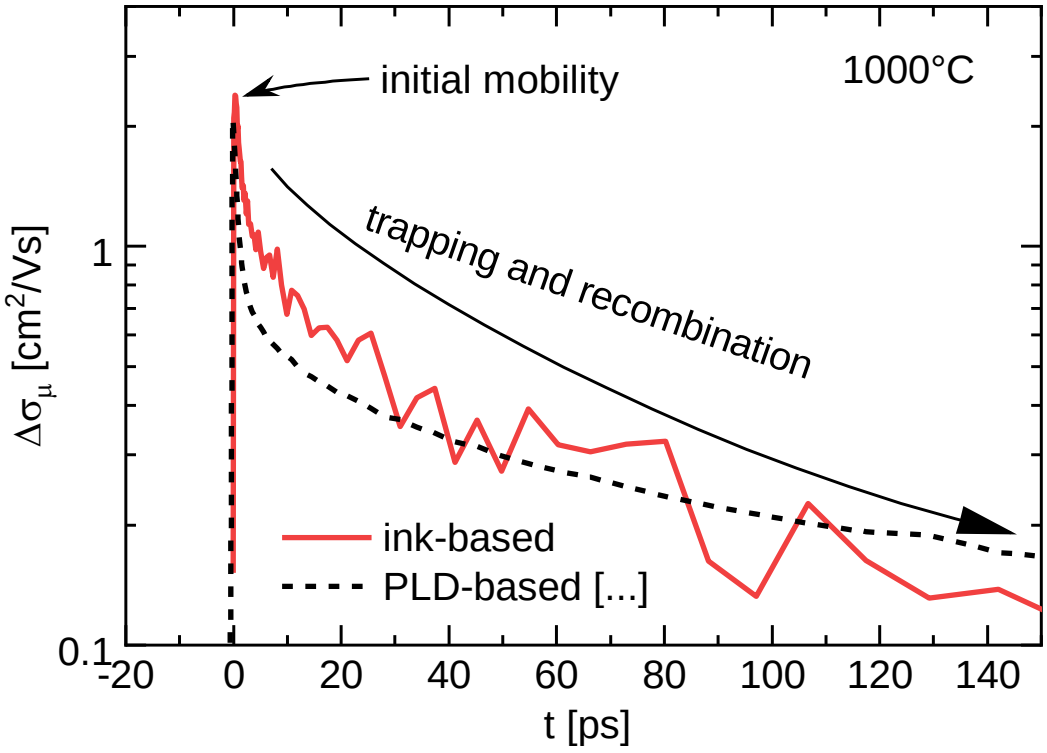

Figure 3.19: Photoconductivity transients of ink-based $BaZrS_3$ studied in this work and PLD-based $BaZrS_3$ published previously in Márquez *et al.* (Reproduced with permission from: Márquez *et al.*, 'BaZrS$_3$ Chalcogenide Perovskite Thin Films by H_2S Sulfurization of Oxide Precursors', Copyright 2021 American Chemical Society.). It is scaled in a way that the initial amplitude yields the charge carrier mobility.

A fast decay in the first ps, is usually attributed to charge carrier trapping into immobile states, which can be understood as a decrease of the effective average mobility. The longer components with a decay time of a few 100s of ps may be attributed to charge carrier recombination. The similarity of the charge carrier mobility and photoconductivity decay indicates that the ink-based processing route has no drawback for the electronic properties of $BaZrS_3$.

3.3. Alloying of $BaZrS_3$ with titanium

The band gap of this material is still too high for PV applications and thus band gap engineering is necessary to decrease it. Alloying with titanium is one of the ways to decrease the band gap to ~1.3 eV for the production of highly-efficient single-junction solar cells or to ~1.7 eV for the production of a top-cell in tandem solar cells. However, using high amount of titanium as alloy results in a phase segregation, since $BaTiS_3$ alone is not stable in the distorted perovskite structure, whereas it is staying in the distorted perovskite structure without a phase change if the Ti/(Ti+Zr) ratio is less than 5 %.[33,69]

In this work, titanium (IV) isopropoxide (Sigma Aldrich, >97%) as a titanium source is mixed to the solution in the ratio of (Ti/(Ti+Zr)) = 3 %. However, it is not possible to confirm the ratio of titanium in the film by using either XRF or EDX, since the emission lines of titanium overlap with zirconium lines.

To observe if there is a titanium binary impurity, a $BaTiS_3$ phase segregation or a titanium incorporation, XRD measurements were performed. As can be seen in Fig. 3.20, the titanium alloyed material has almost the same peak positions with the pure $BaZrS_3$ sample in the distorted perovskite structure. The sulfurization of titanium alloyed samples also results in an increase on the same peak at around 45° compared to the peak at 36° (see Fig. 3.20) as the pure $BaZrS_3$ has. It is likely to form $Ba_4Zr_3S_{10}$ as a secondary phase in trace amount, as seen with the unalloyed material (see chapter 3.2.2). But no additional peak for any other impurity is detected. The photo in the Fig 3.20 shows that the titanium alloyed film color is darker than the pure $BaZrS_3$ material which might be a sign for a better absorbance. And SEM images shows that grain size of the alloyed material is more homogenous compared to the pure one.

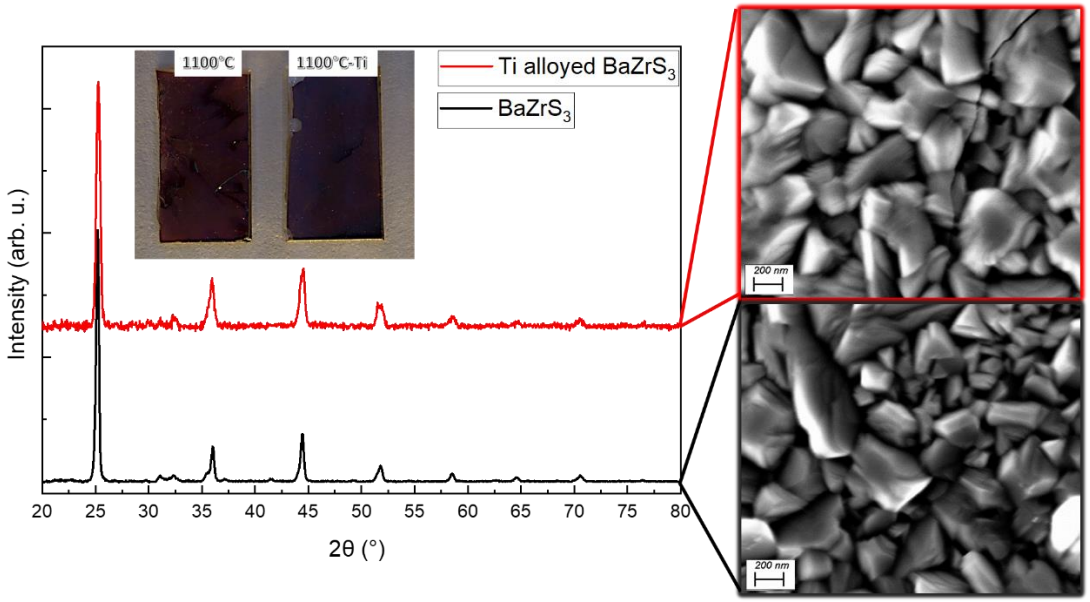

Figure 3.20: Diffractogram comparison of alloyed $BaZrS_3$ with titanium (red) and unalloyed $BaZrS_3$ (black) respectively, both sulfurized at 1100 °C (left). SEM images of the titanium alloyed $BaZrS_3$ (in red box) and plain $BaZrS_3$ (in black box) (right).

In the XRD peak analysis, the comparison of the FWHM shows that the alloying with titanium does not have negative effects on the perovskite formation compared to the pure $BaZrS_3$, e.g., phase segregation or phase transition. Titanium alloying even improves the crystallinity of the sample that was sulfurized at 1000 °C as can be seen in Fig. 3.21. The angle dependent measurements reveal that the crystallinity is almost same in the bulk material.

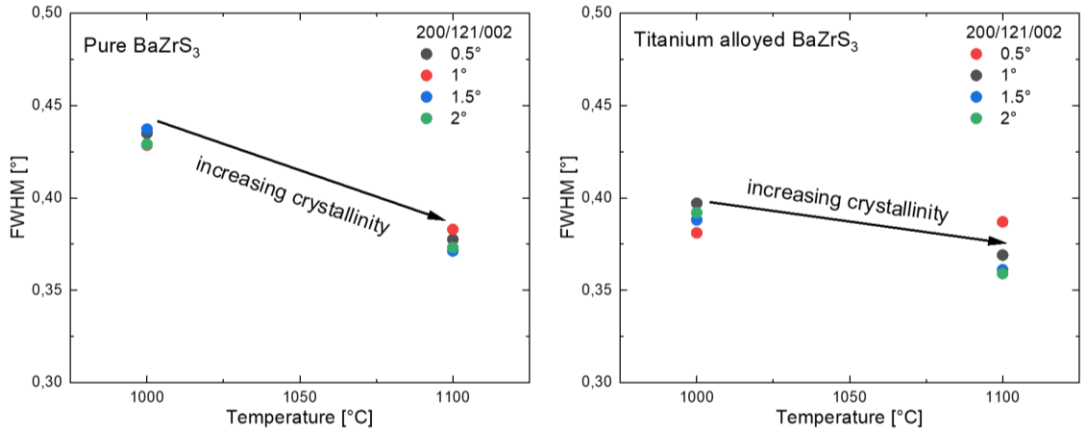

Figure 3.21: Full width at half maximum of the ink-based pure (left) and titanium alloyed (right) $BaZrS_3$ for different grazing incidence angles of XRD measurements.

Raman spectroscopy measurement was performed, since a low amount of titanium in the $BaZrS_3$ structure could not be identified with XRF, EDX and XRD. As can be seen in the Fig. 3.22, the peak at around 400 cm^{-1} position might be attributed to titanium alloying since it is there for both titanium alloyed $BaZrS_3$ samples that were sulfurized at 1000 and 1100 °C and because there were no apparent secondary phases in XRD. The peak at around 350 cm^{-1} can be observed for the titanium alloyed $BaZrS_3$ that sulfurized at 1100 °C as well as pure $BaZrS_3$ that sulfurized at 1100 °C, which might be assigned to $Ba_4Zr_3S_{10}$ phase as the traces can be seen in the XRD measurement.

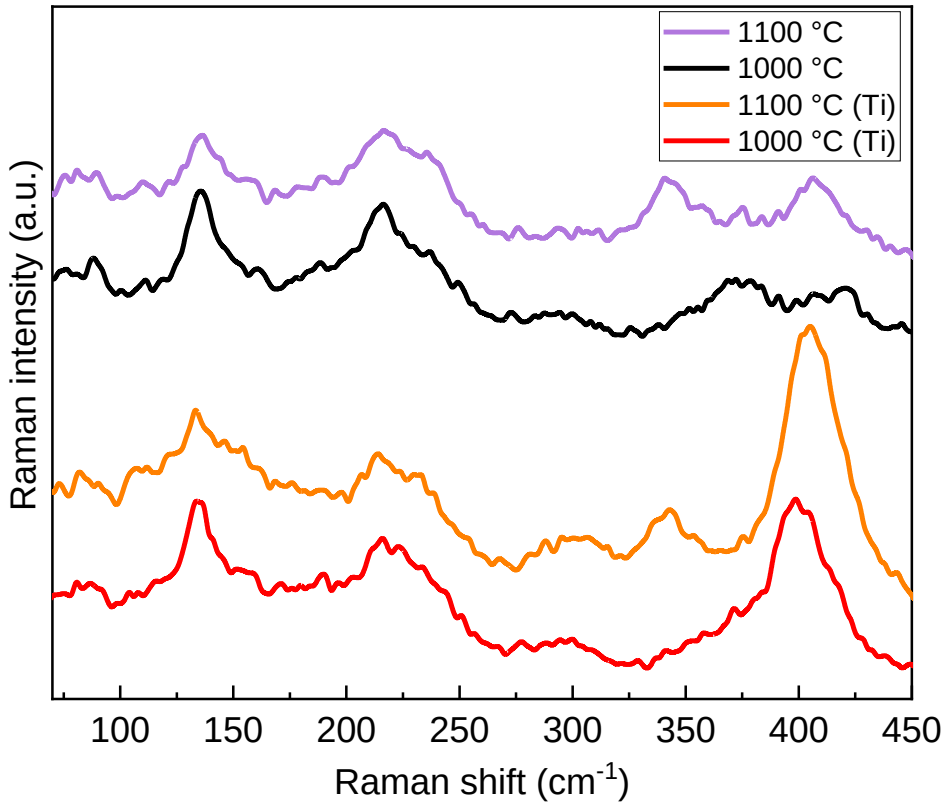

Figure 3.22: Comparison of Raman spectra of pure (black) and titanium alloyed (red) $BaZrS_3$ sulfurized at 1000 °C with comparison of pure (purple) and titanium alloyed (orange) $BaZrS_3$ sulfurized at 1100 °C (orange).

To investigate if the titanium alloying helps as intended to decrease the band gap of $BaZrS_3$, UV-Vis was performed on the Ti-alloyed samples. It was found that the band gap decreased from 2.01 eV (see chapter 3.2.2) to 1.82 eV for the sulfurization temperature of 1100 °C as can be seen in Fig. 3.23. However, it might need higher sulfurization temperature or longer reaction time to incorporate to the structure since the band gap for the sample sulfurized at 1000 °C did not change significantly.

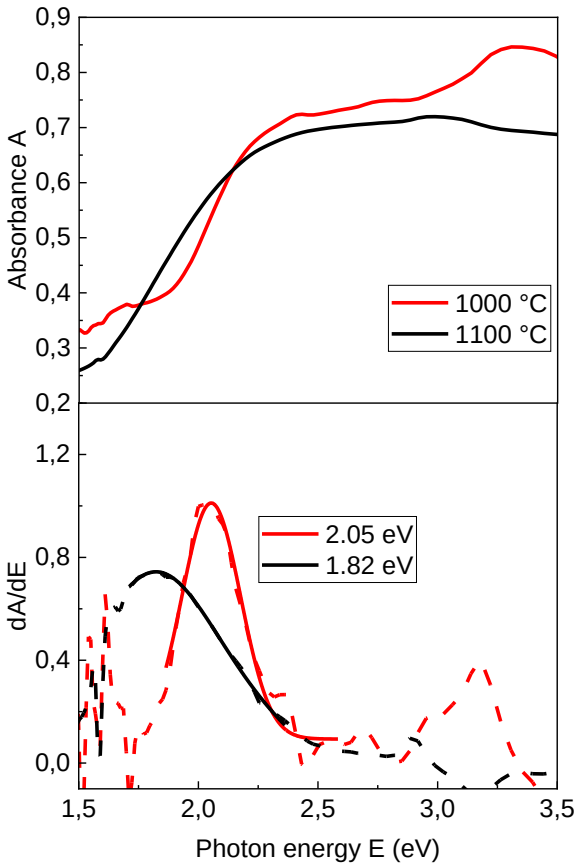

Figure 3.23: Absorbance for the titanium alloyed $BaZrS_3$ films (top), which are sulfurized at 1000 °C (red) and 1100 °C (black). The derivative of the absorbance (dotted) and their Gaussian fits (line, bottom) are used for the determination of the band gap energy values of the films.

To conclude, titanium alloying looks promising to decrease the band gap as an approach of band gap engineering. It is worth considering it for future works in the way of understanding the nature of the chalcogenide perovskites.

3.4. Conclusions

In summary, a novel ink was developed in this work to deposit the precursors of chalcogenide perovskites. $BaZrS_3$-precursor thin films were sulfurized from this ink contains iodide and acetate precursors at the sulfurization temperatures of 600, 700, 800, 900, 950, 1000 and 1100 °C, respectively. The novelty of this ink is that it does not require the middle-step of $BaZrO_3$ formation, as it is used in other reported works.[34,37] Avoiding the step of $BaZrO_3$ formation is crucial to decrease the reaction temperature since it requires higher energy to sulfurize the material to the high degree.

The X-ray diffractograms show that the films start to crystallize above 800 °C. However, the XRF analyses show that the sulfur amounts in the films are not stoichiometric for the reaction

temperatures below 900 °C. The prominent peaks for the distorted perovskite structure with the space group of *Pnma* #62 were identified, whereas no XRD-peaks for oxide or binary products were observed. The ICSD reference diffraction patterns are used for the comparison of the diffractograms. Small amount of $Ba_4Zr_3S_{10}$ is identified on the diffractograms, yet the amount could not be determined, since its prominent peaks overlap with the peaks of $BaZrS_3$. The Ba:Zr ratios remained unchanged even at high sulfurization temperatures. XRD and SEM showed that the crystalline domain sizes increased, as the sulfurization temperature increased. The XRD results reveal that the grains of the solution-processed material show no preferred orientation, whereas the material prepared by the PLD setup has a preferred orientation.

Moreover, the band gap estimations from the UV-Vis data show that the band gap energy decreased, as the sulfurization temperature increased. The band gap is estimated as ~2.02 eV for the film sulfurized for half an hour at 1000 °C, which is close to the PLD processed material. Additionally, the band gap of the titanium alloy (1.82 eV) is significantly lower at 1100 °C than the pure $BaZrS_3$. There is no-significant decrease in the band gap by the increase in sulfurization temperature after 1000 °C, which makes it the optimal reaction temperature for this method, since the formation of $Ba_4Zr_3S_{10}$ at 1100 °C sulfurization temperature can be seen in Raman spectroscopy measurements as well. The KP measurement reveals that the films have n-type semiconductor material properties with the ionization energy of ~5.3 eV.

Alloying with 3% of titanium did not change the phase type from distorted perovskite to non-perovskite phase, even though pure $BaTiS_3$ is in the non-perovskite phase. Moreover, the full width at half maximum values show that titanium alloyed material has similar crystallinity with the pure $BaZrS_3$ material.

As a result, the solution-processed deposition technique revealed its advantage over other deposition methods by getting sulfurized to the high degree even at 900 °C without a sign for oxide impurity in the film. And based on the right compound selection, there is a potential to sulfurize the precursors at even lower temperatures. As a material, $BaZrS_3$ is a good candidate for PV applications and the ink-based solution-processing method is a promising deposition technique for this material.

CHAPTER 4
INVESTIGATIONS OF Ba-Hf PRECURSORS

This chapter focuses on $BaHfS_3$ thin films, which have so far only been reported on in the distorted perovskite structure with the space group of *Pnma* #62 as powders as they are discussed in chapter 1.3.2.

First, a viable synthesis route for a $BaHfS_3$ chalcogenide perovskite thin film was discussed. The first step of this route is the preparation of the molecular ink as it is discussed in chapter 2.1.1. The precursor solution of $BaHfS_3$ has not only metal acetates and metal iodide as a catalyst in a proper solvent mixture but also metal acetylacetonate when the acetate compound is not commercially available. In the second step, the same spin-coating and sulfurization parameters used for $BaZrS_3$ in chapter 3.1 are applied. Finally, the morphological, structural and optoelectronic measurements of the deposited materials are investigated in the last step.

4.1. Preparation of $BaHfS_3$

0.51 mmol of BaI_2 (Santa Cruz Biotechnology, >98%) and 1.96 mmol of barium acetate (ACROS Organics, 99+%) are dissolved in a micture of 3 mL of N-N-dimethylformamide (DMF) (Sigma-Aldrich, 99.9%) and 3 mL of acetic acid (Sigma-Aldrich, >99.8%) to prepare the molecular ink solution at first. 2.05 mmol of hafnium (IV) acetylacetonate powder (Alfa-Aesar, >97%) are added to the mixture afterwards. Finally, the solution is stirred in a glovebox at room temperature for half an hour to obtain a clear and pale-yellow colored solution.

In the spin-coating step, the quartz substrates (1 inch x 1 inch) are rinsed with acetone first. Then a pipette is filled with 250 µL of the precursor solution to dispense the ink onto the substrate. The dynamic spin-coating process is started at 1000 rpm for 10 seconds, and then ramped up in 3 seconds to 3500 rpm and continues to spin there for 20 seconds more. The thickness of the films was only determined after the sulfurization, which is described below. In between deposition of layers, the substrates are held at 250 °C for 2 minutes and additionally at 250 °C for 10 minutes after spin-coating to evaporate the solvent residual.

The spin-coated films are taken out of the glovebox right before sulfurization to minimize the chance of oxidation, since the replacement of oxygen with sulfur needs more energy. The samples are put in a quartz boat so that the samples can be placed into the furnace without contamination from the furnace. After placing the quartz boat in the middle of the quartz tube,

it is ready to be evacuated. The furnace is evacuated first, then flushed with argon twice, and then flushed with 5% H_2S in argon for the third time. As the valve of the scrubber is opened, the flow of sulfurization gas is initiated. The gas inlet is set to 60 sccm of 5% H_2S (± 0.15 Vol %, Air Liquide) in argon. After reaching to the desired flow, the furnace is turned on to heat up. The sulfurization temperature is set to be reached in 30 minutes. Another 30 minutes is set for the sulfurization process at the chosen temperature as well. After the reaction the furnace is left to cool down naturally. After reaching a temperature of 400 °C, the gas flow is changed back to pure argon to remove the residual H_2S in the tube. The sulfurized samples are collected when the temperature reaches room temperature.

4.2. Results and discussions

As an alternative to $BaZrS_3$, $BaHfS_3$ can be produced in similar conditions. To investigate its structural, compositional, morphological, and subsequently optoelectronic properties, following measurements were conducted in this section.

4.2.1. Molecular ink preparation route of $BaHfS_3$

Solution-processed precursors for $BaHfS_3$ are prepared analogously to $BaZrS_3$ precursors, which the molecular ink was initially designed for. Only the transition metal ion is changed from acetate to acetylacetonate, since hafnium (IV) acetate is not commercially available. Acetylacetonates are more expensive than acetates since they are used especially for metal organic chemical vapor deposition processes. Under vacuum, the organic parts of acetylacetonates can decompose easily and set the metal part free to react. Unlike most of the metal halides, acetylacetonates are soluble in organic solvents.

4.2.2. Elemental composition and crystal structure of $BaHfS_3$

The elemental Ba:Hf ratio of the deposited material is measured by XRF as 1.00±0.01:1.05±0.01 (see Table 4.1), although the elemental Ba:Hf ratio of the solution was approximately 1.25:1 according to the molecular ink recipe. It is concluded that due to the spin-coating conditions and low surface interactions of barium compounds, some of the barium material is lost during deposition. Changes in the composition ratio could occur when different coating conditions are implemented.

Using XRF analysis it is observed that the films were totally sulfurized. Above the annealing temperature of 1000 °C, the elemental stoichiometry is close to the perovskite structure stoichiometry of 1:1:3. Wang *et al.* reported in his paper that barium forms BaS_3 before

reacting with ZrS_2 to form $BaZrS_3$, which might explain the excess sulfur at 1000 °C. The same pattern is observed for the ink-based $BaZrS_3$ in chapter 3.2.2.[46] The XRF analysis also showed that the Ba:Hf ratio changed slightly after sulfurization, this can be explained by that fact, that hafnium acetylacetonate is volatile under vacuum. The Ba:Hf ratios of the samples before and after sulfurization can be seen also in Table 4.1.

Table 4.1: Elemental composition for $BaHfS_3$ thin films prepared at the sulfurization temperatures of 1000 and 1100 °C, obtained by XRF analysis. Ba:Hf shows the cation ratio on the precursor films before the sulfurization step. Ba:Hf:S indicates the elemental ratio after sulfurization at the given temperature.

Sulfurization temperature (°C)	**Precursor Ba:Hf (molar %)**		**After sulfurization Ba:Hf:S (molar %)**		
1000 °C	1.00±0.01	1.05±0.01	1.00±0.01	1.00±0.01	3.36±0.02
1100 °C	1.00±0.01	1.05±0.01	1.00±0.02	1.00±0.04	2.93±0.05

The clear pale-yellow color of the precursor turns into a golden yellow color after sulfurization (see fig. 4.1). After the sulfurization, the obtained film reaches approximately 185 nm thickness by using three cycles of dynamic dispense spin-coating. To verify the formation of the desired Perovskite structure XRD was performed. The X-ray diffraction (XRD) patterns in Fig 4.1 show that all the prominent peaks of the orthorhombic $BaHfS_3$-structure (space group *Pnma* #62) are present on the measured pattern. Another interpretation of the diffractograms can be that there is no preferred orientation for the crystals, since the diffractogram peaks of the sample have a similar integral intensity pattern with the reference peaks of the powder sample of the ICSD database. The FWHM of the solution deposited $BaHfS_3$ sulfurized at 1100 °C is 0.381, which is comparable with the values and the crystallinity of the solution deposited $BaZrS_3$.

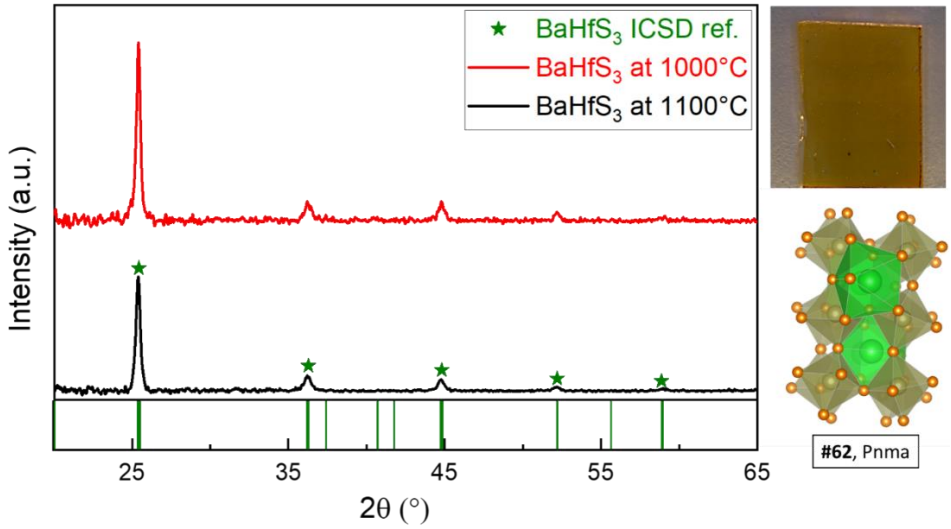

Figure 4.1: XRD pattern of the solution-processed $BaHfS_3$ sulfurized at 1000 °C (red), 1100 °C (black) and the reference pattern from the ICSD database (green, ICSD-615918) (left), image of the solution-processed sulfurized $BaHfS_3$ sample (top right), crystal structure of $BaHfS_3$ visualized by VESTA software (bottom right).

Raman spectroscopy is used as a complementary measurement to XRD to cross-check the structural properties of $BaHfS_3$ thin film (see Fig.4.2). For $BaZrS_3$ the peaks at ~137 cm^{-1} and ~216 cm^{-1} are signature A_g peaks, which can be seen for $BaHfS_3$ as well. This similarity could be due to similar chemical properties of hafnium and zirconium, e.g. the ionic radii of Hf and Zr for six-coordination are 0.71 and 0.72 Å respectively.[28] In $BaHfS_3$, there are three Hf-S bonds with almost the same binding strengths, which result in the distorted perovskite structure.[70]

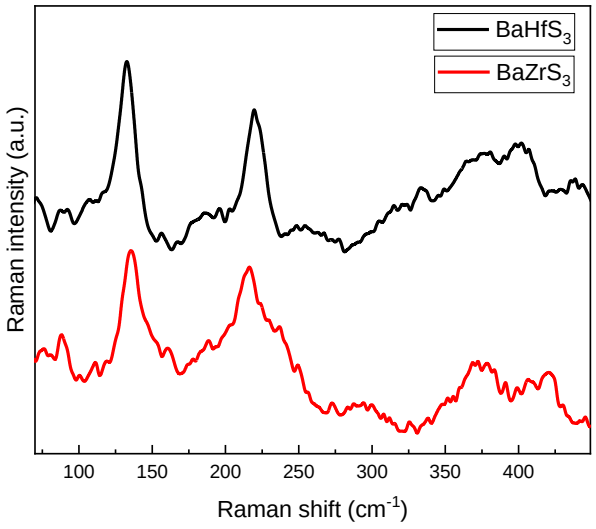

Figure 4.2: Raman spectra of $BaHfS_3$ film sulfurized at 1100 °C (black) and as a reference $BaZrS_3$ film sulfurized at 1000 °C (red) that are measured at the room temperature for 60 seconds.

Scanning electron microscopy (SEM) is conducted to investigate the crystal morphology of the material. It can be seen in the Fig. 4.3 that the crystallite size reached ~300 nm at 1100 °C. High-magnification imaging of this material with the in-Lens secondary electron detector is difficult due to charging effect, possibly because the crystal domain sizes are not big enough to reach each other and to provide enough lateral conduction to measure. Nevertheless, these low magnification topography images are clear enough to determine the crystal domain sizes.

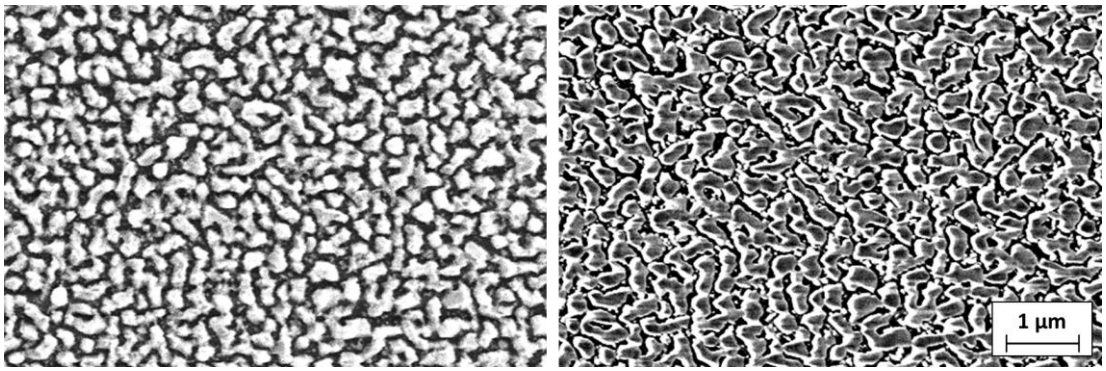

Figure 4.3: Topography secondary electron (left) and in-Lens secondary electron (right) images of the $BaHfS_3$ thin film for the sulfurization temperature of 1100 °C. The scale applies for both images.

As the elemental composition and crystal structure could be determined to fit to $BaZrS_3$, further measurements will be performed to obtain the optoelectronic properties.

4.2.3. Optoelectronic properties of $BaHfS_3$

Due to the same reason of not having high quality secondary electron images, KP and PYS measurements could not be conducted. While the $BaZrS_3$ samples reported above were conductive enough by themselves to be measured by these measurements, $BaHfS_3$ does not have such lateral conductivity with this deposition technique. Another plausible reason for low conductivity could be a lower carrier concentration.

For the calculation of absorbance, transmittance and reflectance were measured via UV-Vis spectrometer. Fig. 4.4 shows that the optical band gap energy decreases due to the perovskite formation as the sulfurization temperature increases. The band gap energy of the thin films that are sulfurized at 1000 and 1100 °C are calculated by the derivative of the absorbance as 2.52 and 2.26 eV, respectively.

Optical-Pump Terahertz-Probe spectroscopy is used to investigate the dynamics of photogenerated charge carriers via the photoconductivity transient $\Delta\sigma_\mu$. On the right side of the Fig. 4.4, the photoconductivity transients of $BaHfS_3$ and $BaZrS_3$ can be seen.

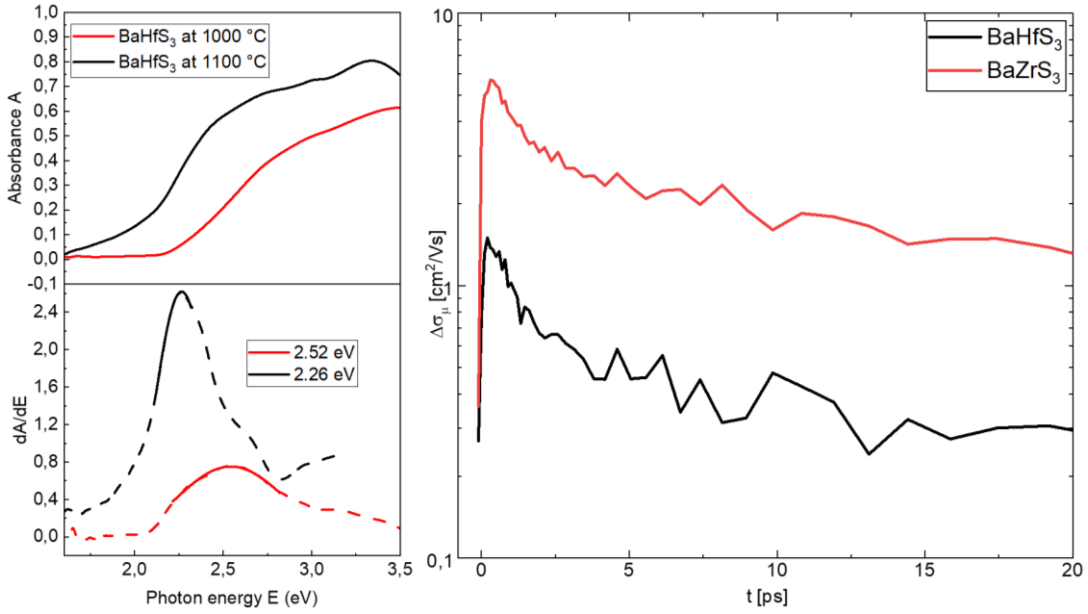

Figure 4.4: Absorbance for the $BaHfS_3$ films (top left), which are sulfurized at 1000 °C (red) and 1100 °C (black). The derivative of the absorbance and their Gaussian fits (bottom left) are used for the determination of the band gap energy values of the films. Photoconductivity transients (right) of ink-based $BaHfS_3$ (black) that is sulfurized at 1100 °C and ink-based $BaZrS_3$ that is sulfurized at 1000 °C (red) that is scaled in a way that the initial amplitude yields the charge carrier mobility.

The photoconductivity response is very similar to $BaZrS_3$, showing a very fast initial decay on the picosecond timescale, followed by a slower decay. Similar to the case of $BaZrS_3$, the fast decay in the first ps is believed to be due to charge carrier trapping into immobile states. The initial amplitude indicates a DC charge carrier sum mobility of 1.5 cm^2/Vs in the material which is about a factor 3-4 smaller than the values obtained for $BaZrS_3$. This may be in part due to the smaller-grained morphology of $BaHfS_3$ compared to the latter thin films obtained by solution processing.

4.3. Selenization of the sulfurized $BaHfS_3$

Previously conducted studies are discussed in chapter 1.3.7 in detail. Selenization of the sulfurized $BaHfS_3$ is studied in this work as well, due to similar chemistry of sulfur and selenium, since they are in the same chemical group on the periodical table. Aforementioned properties of the band gap engineering (see chapter 2.1.4) allow selenization to decrease the band gap into the efficient range for solar cell applications.

In this study, an already sulfurized sample is used to replace sulfur with selenium. Sulfurization is conducted in the custom selenization tube furnace which was introduced in chapter 2.1.3.2. The setup can reach up to 542 °C during the process with 300 mg of Se chunks in the closed graphite box. The graphite box is kept at the cold zone during the air evacuation and is slid into the hot zone after flushing with nitrogen twice. The pressure of the tube furnace is kept at 100 mbar. The temperature of the tube furnace decreased to around 500 °C when the graphite box is placed in the hot zone, however it reaches 542 °C again after about 20 minutes during the experiment. The samples were cooled down naturally.

XRF measurements show that the amount of sulfur in the material decreased significantly from during the 60-minute-long selenization. On the other hand, the amount of selenium did not increase as it is supposed to be in the 1:1:3 ratio of the perovskite structure but barely reached ~0.5. The elemental composition of Ba:Hf:S:Se is obtained by XRF analysis as 1.16:1.00:0.06:0.47 after the 60-minute-long selenization.

Filippone *et al*. calculated the material properties of $BaHfSe_3$ and reported its formation energy as -0.447 eV/f.u. Unfortunately the phase diagrams for these materials were not plotted in the literature because the thermodynamic data for $HfSe_2$ was not available.[32,71] Nevertheless the calculation was done later, and the ground state of $BaHfSe_3$ was reported as needle-like non-perovskite configuration.[23,43]

XRD measurements were conducted to control if the materials were selenized in the perovskite structure. As it can be seen in Figure 4.5, the X-ray diffractogram of the material selenized for 30 minutes did not have any dominant peaks, whereas 60 minutes of selenization was sufficient to selenize barium in the film. The selenized barium is indexed as $BaSe_3$ which is shown with green stars. $BaSe_3$ with an ionic formula of $Ba^{2+}Se^{0}Se_2^{-1}$ is a brown-red material which is a nonmetallic polyselenide.[72] In addition, there are unindexed peaks which are not available in the reference databases. Although the peak at 29.6 ° can be indexed either HfO_2 or HfI_4, indexing based on just one peak would not be dependable. The peak width around 20° might come from the quartz substrate since the material is deposited as thin film or it might come from the non-oriented phase of the perovskite or both.

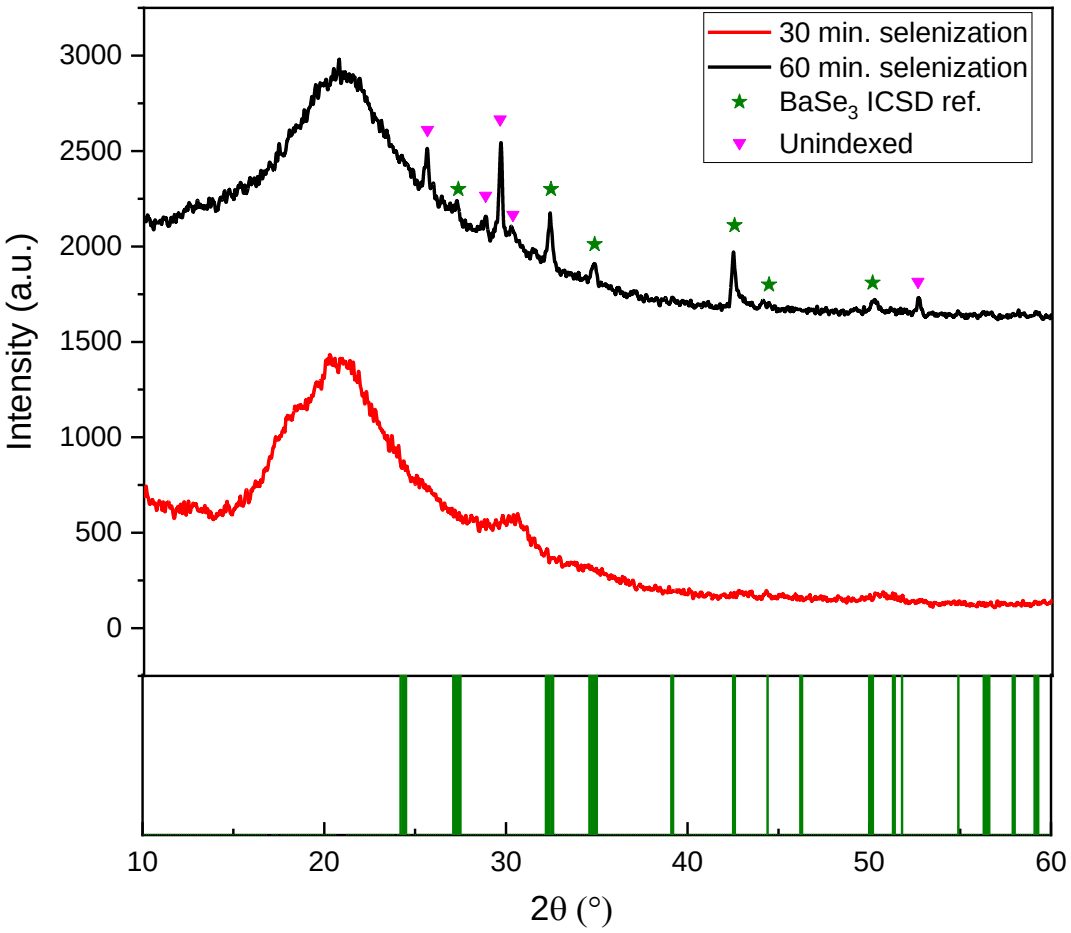

Figure 4.5: XRD images of selenized $BaHfS_3$ at 542 °C for 30 minutes (red) and 60 minutes (black) in the selenization tube furnace. Peaks are indexed according to the ICSD reference for $BaSe_3$ (green, ICSD-16359) and peaks that cannot be indexed (magenta) are shown as well.

From the measurements of XRF and XRD, it can be seen that excess barium is selenized and the stable phase of $BaSe_3$ is synthesized. The perovskite structure is neither selenized nor held the sulfur amount that it had previously. It is possible that the perovskite sample lost the sulfur in the vacuum due to the high temperature and then formed non-oriented oxide materials after taking the sample out from the tube furnace. Since the XRF system used in this work cannot measure oxygen, it is not visible there. Furthermore, since room temperature is not enough to give orientation to the oxidizing crystals, the XRD pattern was not showing peaks related to these phases. Another possibility is the formation of alloys, which might explain the unindexed XRD peaks, as they are not available in diffractogram databases.

4.4. Conclusions

$BaHfS_3$ in the distorted perovskite structure are deposited as thin films on quartz substrates for the first time. The material requires a higher sulfurization temperature than $BaZrS_3$, which

needs 1000 °C, whereas $BaHfS_3$ needs 1100 °C for a lower band gap value. Either high reaction temperature or longer sulfurization time could help to deplete this BaS_3, that XRF shows for 1000 °C, to form $BaHfS_3$ as well. The elemental composition and the sulfurization degree are confirmed via XRF analysis which shows that a small amount of hafnium is lost during the sulfurization. The magnitude of the loss, however, it is within the uncertainty of the measurement technique. Under the reactive H_2S atmosphere, it is observed that the setup used in this study could sulfurize the deposited hafnium (IV) acetylacetonate as expected.

The distorted perovskite crystal structure is also confirmed via XRD measurements by the comparison of material diffractogram with the ICSD database reference pattern.[28] This comparison also shows that the crystals did not have any preferred orientation. No secondary phase in a significant amount was detected with the XRD in the film. Topography images of 300 nm wide crystalline are taken via SEM. UV-Vis measurements are conducted to determine the absorbance of the material. By using the derivative of absorbance, the band gap is estimated as 2.26 eV for the film that is sulfurized at 1100 °C. The photoconductivity transients of $BaHfS_3$ are very similar to those measured on $BaZrS_3$ and show low intragrain sum mobilities close to $1 cm^2/Vs$ and short charge carrier decay times in the picosecond regime, which indicates that optoelectronic properties should be improved for the use in photovoltaic applications.

The selenization attempts were not successful, possibly due to the high temperature need of hafnium selenization, as reported in the literature, since the barium in the bulk is selenized into $BaSe_3$. It is reported in the former studies that $HfSe_2$ can be synthesized at around 800-900 °C.[55,73,74] However, since the formation energy is different for different reaction pathways, it is worth trying to selenize $BaHfS_3$ at temperatures lower than the selenization temperature of hafnium metal.

CHAPTER 5
INVESTIGATION OF $EuZrS_3$ PEROVSKITE

The survey about the studies of $EuZrS_3$ is reported in chapter 1.3.3. This chapter will cover the study of $EuZrS_3$, to understand the nature of its phases. In comparison with $BaZrS_3$, the distorted perovskite structure of $EuZrS_3$ (β-phase) needs higher temperature to form the perovskite structure, whereas the needle-like non-perovskite configuration (α-phase) needs lower temperature to form.[28,41]

Again, three main steps are used to obtain a viable synthesis route to produce $EuZrS_3$ chalcogenide perovskite thin film. The molecular ink is prepared in the first step. The solution of $EuZrS_3$ has binaries of not only metal acetates and metal iodide as a catalyst in a proper solvent mixture but also metal acetate-hydrate. The optimal spin-coating and sulfurization parameters used for $BaZrS_3$ were used here as well. The optimal sulfurization parameters of the deposited material in H_2S atmosphere are discussed in the last step.

5.1. Preparation of $EuZrS_3$

To begin, 0.51 mmol of ZrI_4 (Santa Cruz Biotechnology, >98%), 4.21 mmol of europium acetate-hydrate (Alfa-Aesar, >99.9%) are dissolved in 3 mL of N-N-dimethylformamide (DMF) (Sigma-Aldrich, 99.9%) and 3 mL of acetic acid (Sigma-Aldrich, >99.8%) mixture to prepare the molecular ink solution. As the next step, 1.37 mL of zirconium (IV) acetate solution (Sigma-Aldrich, 3.07 mmol of Zr in dilute acetic acid) are added to the mixture. The prepared solution is stirred in a glovebox at room temperature for half an hour to obtain a murky-white solution.

The quartz substrates (1 inch x 1 inch) are rinsed with acetone before spin-coating the solution on them. 250 µL of the precursor solution is taken by a pipette to dispense the ink onto the substrate. The films are spin-coated dynamically at 1000 rpm for 10 seconds, and then the spin rate is ramped up in 3 seconds to 3500 rpm and the coating continued for 20 seconds more. After 2 repetitions of dynamic dispense spin-coating and then the sulfurization, the deposited film reaches approximately 180 nm thickness. Substrates are held at 250 °C for 2 minutes in between spin-coating of layers and are held also at 250 °C for 10 minutes in the end, to evaporate the solvent residual.

To minimize the oxidation of the precursor, spin-coated films are taken out of the glovebox right before sulfurization since the sulfur replacement of oxygen needs more energy. The samples are put in a quartz boat to place the samples into the furnace. As soon as the quartz boat is placed in the middle of the furnace, oxygen in the quartz tube can be evacuated. Firstly, the furnace is evacuated, and then flushed with argon twice. For the third flushing, the furnace is flushed with 5% H_2S in argon. The flow of sulfurization gas is initiated when the valve of the scrubber is opened. The reactive gas inlet is set to 60 sccm of 5% H_2S (± 0.15 Vol %, Air Liquide) in argon. The furnace is turned on to heat up when the flow is ready. The desired reaction temperature for sulfur replacement is set to be reached in 30 minutes. And after another 30 minutes of sulfurization process, the furnace is left to cool itself down naturally. As the temperature reaches down to 400 °C, the gas flow is changed back to pure argon to remove the residual H_2S in the tube. When room temperature is reached the samples are collected.

5.2. Results and discussions

$EuZrS_3$ is a material that there is not enough data reported in the literature yet. In the following sections, the preparation method of the $EuZrS_3$ in the distorted perovskite structure is explained. The effects of different sulfurization temperatures on its compositional, structural, morphological and optoelectronic properties are studied.

5.2.1. Molecular ink preparation route of $EuZrS_3$

Solution-processed $EuZrS_3$ is prepared similarly to $BaZrS_3$, as the molecular ink is designed for. Only the earth-alkali metal is changed to europium and its ion is changed from acetate to acetate-hydrate since anhydrous europium (III) acetate is not commercially available. Even though the lanthanide member europium is stable with 3+ ionic charge, it forms with 2+ ionic charge in the perovskite structure. It is possible to dissolve europium (III) acetate-hydrate in organic solvents of DMF and acetic acid mixture. For the catalyst effect of iodine as reported above for $BaZrS_3$ and $BaHfS_3$, a low amount of ZrI_4 is used.

5.2.2. Elemental composition and crystal structure of $EuZrS_3$

The elemental Eu:Zr ratio of the deposited material is measured as 1.00:1.07 (see Table 5.1), although the elemental Eu:Zr ratio of the solution is approximately 1.17:1.00 according to the molecular ink recipe. Possibly some of the europium (III) acetate-hydrate is lost during spin-

coating due to the low surface interaction with the substrate. Hence, changes in the elemental ratio should be considered when different conditions of coating are implemented.

It is seen via X-ray fluorescence (XRF) analysis that the films were sulfurized at 1100 °C to a much high degree than films sulfurized at 1000 °C. Annealing the film at the temperature of 1100 °C made the elemental stoichiometry closer to the perovskite structure stoichiometry of 1:1:3, however they were still not completely sulfurized. The Eu:Zr ratios for before and after sulfurization can be seen also in Table 5.1.

Table 5.1: Elemental composition for $EuZrS_3$ thin films at the sulfurization temperatures of 1000 and 1100 °C. Eu:Zr shows the cation ratio on the precursor films before the sulfurization step. Eu:Zr:S indicates the elemental ratio after sulfurization at given temperature.

Sulfurization temperature (°C)	**Precursor Eu:Zr (molar %)**		**After sulfurization Eu:Zr:S (molar %)**		
1000 °C	1.00±0.01	1.07±0.01	1.00±0.02	1.06±0.02	1.08±0.03
1100 °C	1.00±0.01	1.07±0.01	1.00±0.02	1.04±0.02	2.63±0.01

All the prominent peaks of the orthorhombic $EuZrS_3$-structure reference (space group *Pnma* #62), that can be seen in Fig 5.1, are present on the samples X-ray diffraction (XRD) patterns. It is concluded that there is no preferred orientation for the crystals since the diffractogram peaks of the powder sample have the similar intensity pattern with the reference peaks of the powder sample of the ICSD database.[28]

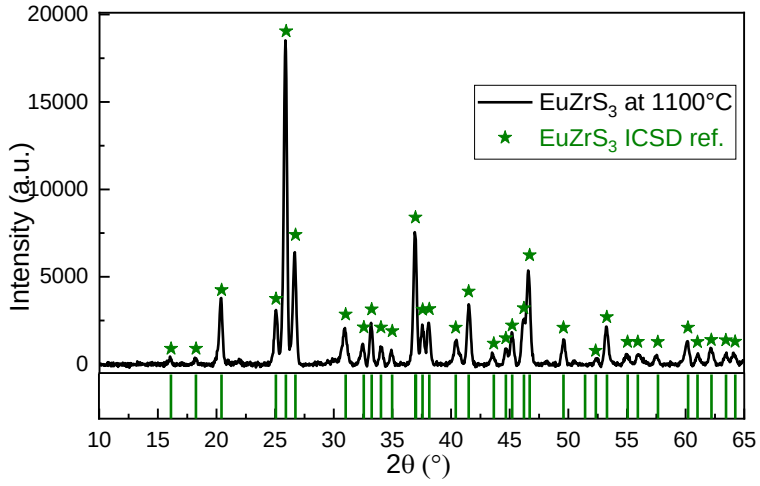

Figure 5.1: XRD patterns of the deposited film that is sulfurized at 1100 °C (black) for 30 minutes. The ICSD database reference (below) for $EuZrS_3$ with the orthorhombic perovskite structure (ICSD-631644) is shown in green.

The lattice parameters are shown in Fig. 5.2 which were extracted from the grazing incidence XRD measurements. They are compared with the lattice parameters of $BaZrS_3$, since they both are from the same space group of *Pnma* #62 and the distorted perovskite crystal structure.

Material	Lattice parameters at 1° grazing incidence angle					
	a (Å)	±	*b* (Å)	±	*c* (Å)	±
$BaZrS_3$	7.074	0.001	9.994	0.001	7.002	0.001
$EuZrS_3$	7.101	0.001	9.721	0.001	6.693	0.001

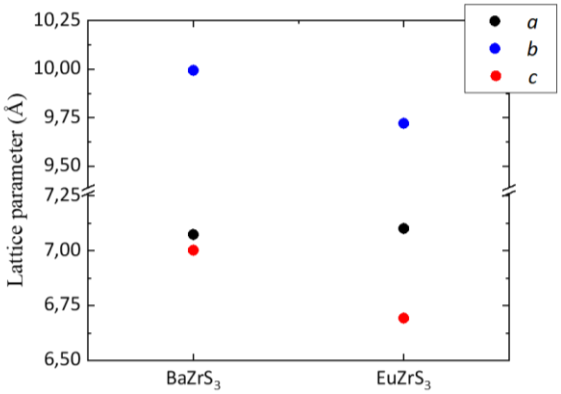

Figure 5.2: Lattice parameters comparison of the $BaZrS_3$ and $EuZrS_3$ distorted perovskites for the grazing incidence angle of 1°.

In another set of films discussed in the following, EuS crystals are formed as well, since the materials are europium rich in the ratio of Eu:Zr = 1.07:1.00. Based on increasing intensity of EuS with the increasing sulfurization temperature, it is possible to conclude that EuS is the limiting compound of the perovskite formation. Hence using EuI_2 instead of using ZrI_4 could catalyze the reaction by forming EuS at a lower temperature and react with zirconium. On the other hand, the color change of white color of the precursor into brown color might be a sign for sulfurization (see Fig. 5.3).

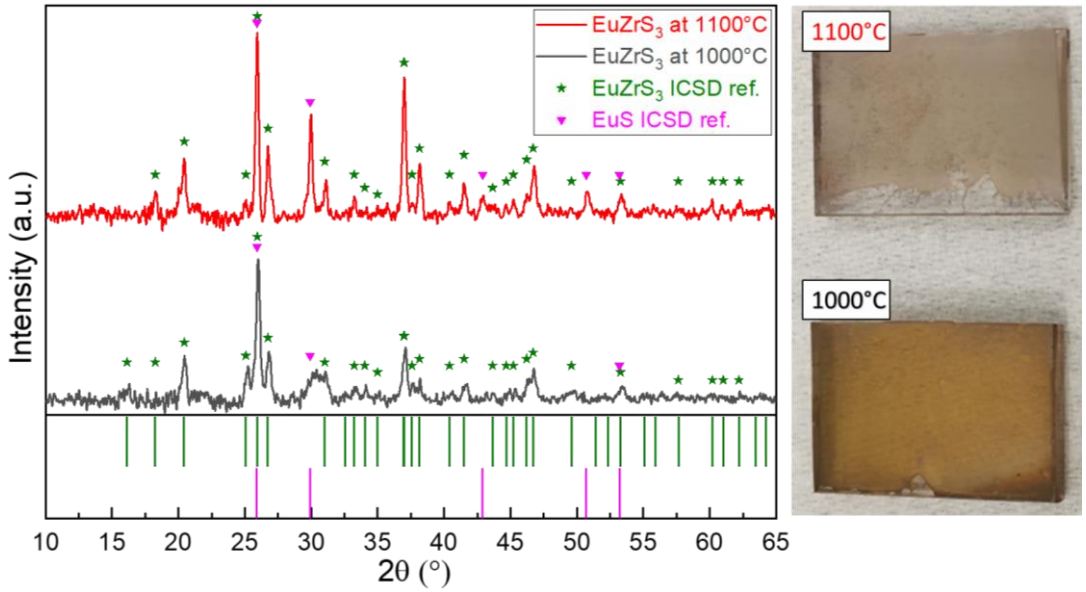

Figure 5.3: XRD patterns of the Eu-rich deposited films (left) (Eu:Zr=55:45) that are sulfurized at 1000 (black) and 1100 °C (red) for 30 minutes. ICSD database references are shown below for $EuZrS_3$ with the orthorhombic perovskite structure (ICSD-631644, green) and EuS (ICSD-657615, magenta).

The Raman peaks for the $EuZrS_3$ thin film and ink-based $BaZrS_3$ thin film (see chapter 3.2.3) can be seen in Figure 5.4. The similarity in peak positions can be observed which can be related to the similar structure.

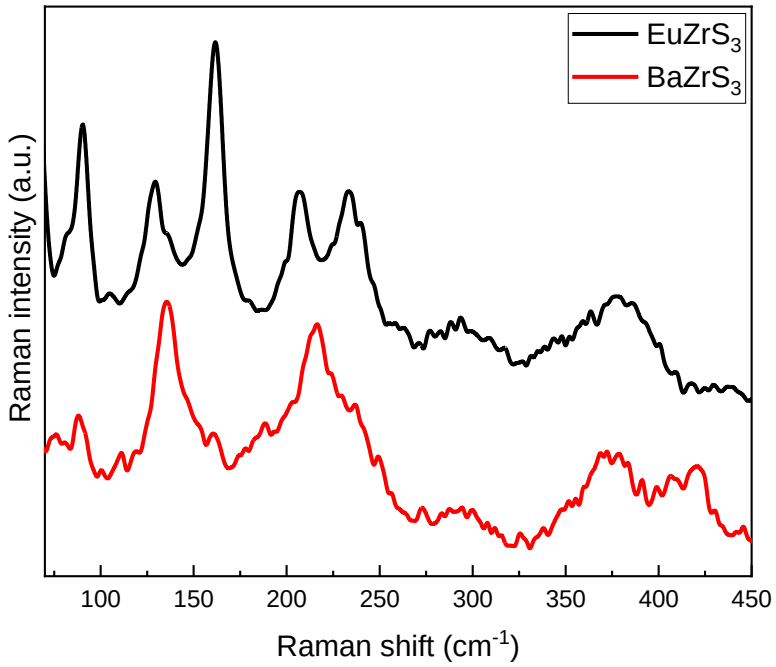

Figure 5.4: Raman spectra of $EuZrS_3$ film sulfurized at 1100 °C (black) and $BaZrS_3$ film sulfurized at 1000 °C (gold) that are measured at the room temperature for 60 seconds.

The following scanning electron microscopy (SEM) images in Fig 5.5 show that the crystalline size reached ~150 nm at 1100 °C. Since the XRD patterns show that there is perovskite formation for both reaction temperatures, the perovskite film at 1000 °C is covered by other phases, as can be observed in the first image. Because of the charging effects, going up to higher magnifications was not possible. The EDX measurements were not conclusive due to the same reason.

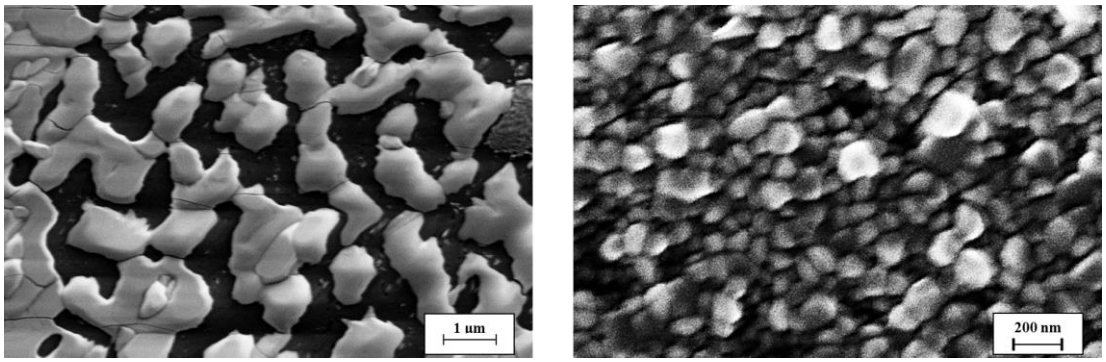

Figure 5.5: SEM images of the $EuZrS_3$ thin films for the sulfurization temperature of 1000 (left) and 1100 °C (right).

Since the material was determined in accordance with ICSD database reference, further measurements were performed, to determine the optoelectronic properties, which are necessary for the assessments of the material's eligibility for PV applications.

5.2.3. Optoelectronic properties of $EuZrS_3$

To calculate the absorbance, transmittance and reflectance were measured with the UV-Vis spectroscopy. As can be seen in Fig. 5.6, the band gap energy decreases, as the sulfurization temperature increases. Due to the changing of detectors, there are artifacts in the derivation of absorbance below 1.5 eV which can also be seen in the absorbance graph. Thus, Savitzky-Golay smoothing filter and Gaussian fit methods were used to estimate the band gap energy. It is concluded from the UV-Vis measurement that the material sulfurized at 1000 °C has the band gap of 2.06 eV, whereas the one sulfurized at 1100 °C has the band gap of 1.68 eV. So far, there is no band gap report for the distorted perovskite (β) phase of the material. On the other hand, the experimental band gap of 1.09 eV is reported for the non-perovskite configuration (α- $EuZrS_3$).[41] And when the tendency of having higher band gap in the distorted

perovskite structure than the one in the needle-like non-perovskite configuration is considered, it is likely that the numbers here are reliable.[23,25]

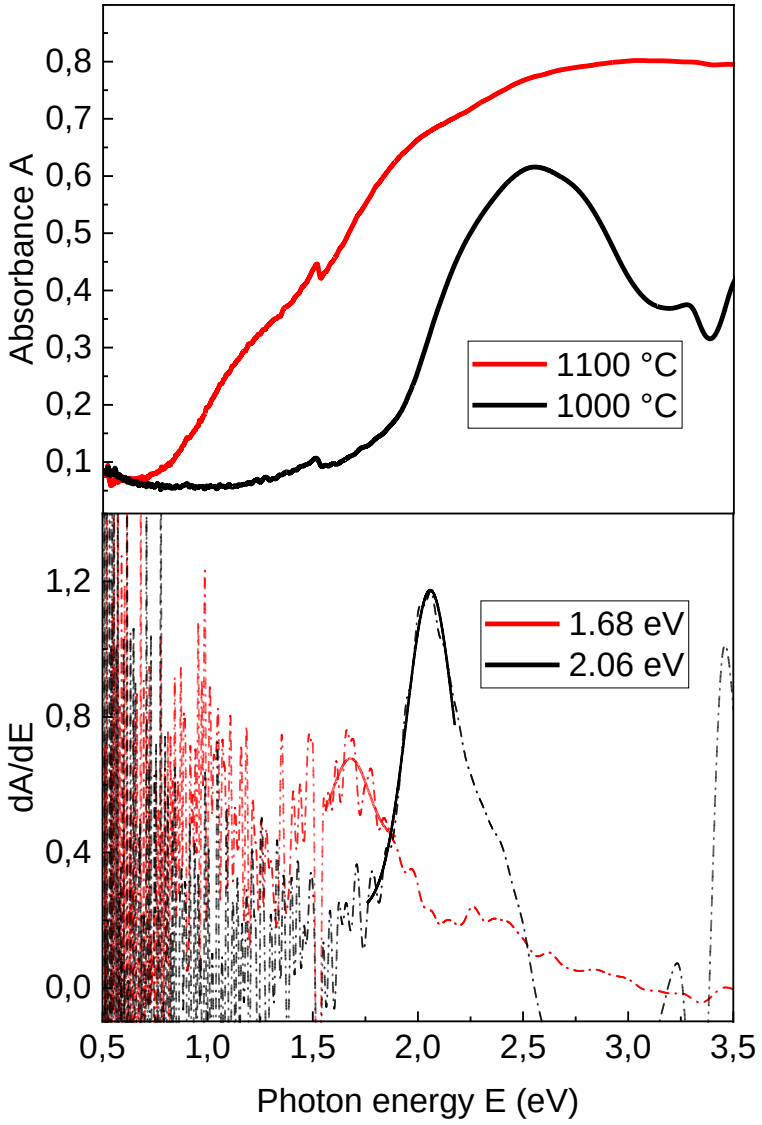

Figure 5.6: Absorbance for the films (top left), which is sulfurized at 1000 (black) and 1100 °C (red). The derivative of the absorbance and its Gaussian fits (bottom left) are used for the determination of the band gap energy values of the films.

Kelvin-Probe (KP) measurement is used under nitrogen atmosphere to determine the work function and the surface photovoltage of the films sulfurized at 1000 °C and 1100 °C. The results are shown in Fig. 5.7. The samples are illuminated by 532 nm laser. The difference between dark and light measurements gives the surface photovoltage which can be seen in Table 5.2. The work function is in the range of 4.4-4.7 eV. And the samples only differ in their sulfurization temperatures, since they are identically deposited precursors.

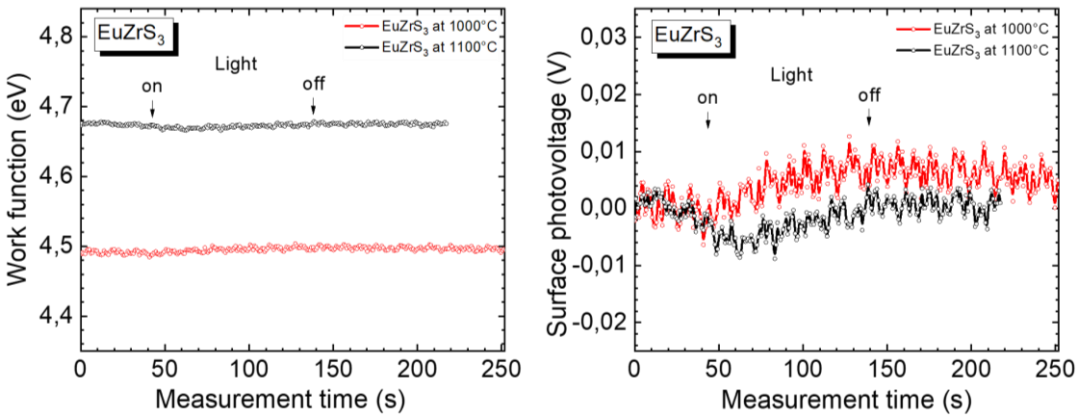

Figure 5.7: The work function and the surface photovoltage of the $EuZrS_3$ films sulfurized at 1000 °C (red) and 1100 °C (black).

Photoelectron Yield Spectroscopy (PYS) measures the ionization energy and the density of states (DOS) by using the derivative of the photoemission current. These measurements were done under nitrogen atmosphere as can be seen Fig. 5.8.

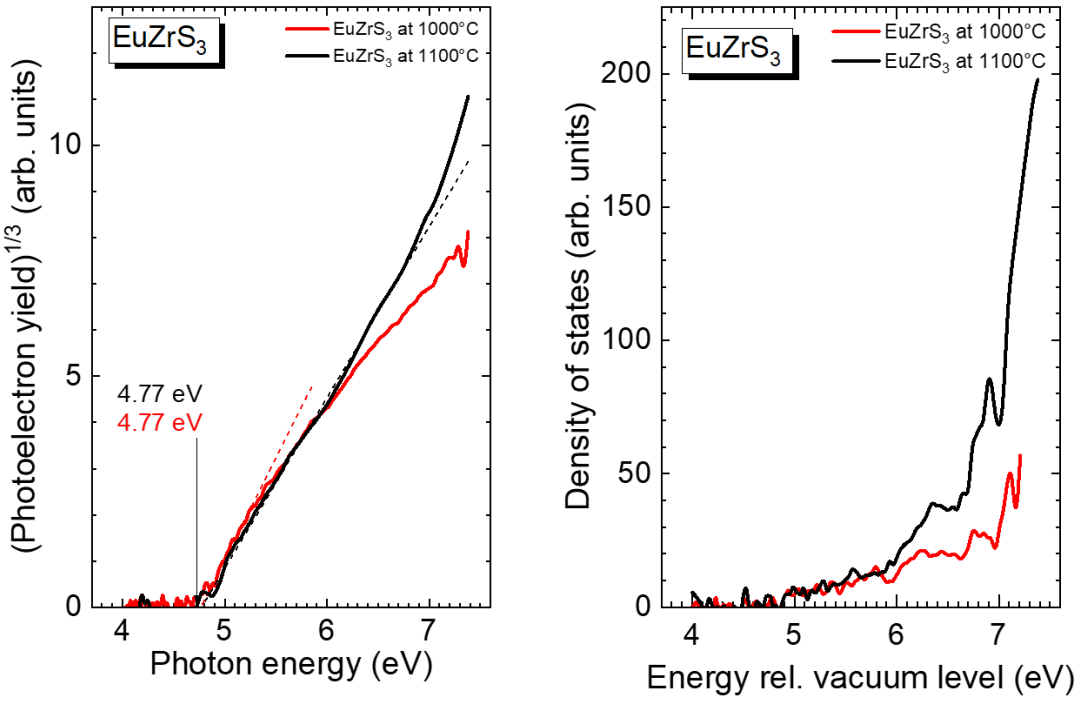

Figure 5.8: Ionization energy (left) and density of states (right) of the $EuZrS_3$ films sulfurized at 1000 (red) and 1100 °C (black).

It can also be seen in Fig. 5.8, that KP and PYS measurements show that the solution-processed $EuZrS_3$ material has an ionization energy of 4.77 eV (see Table 5.2). The negative value of the surface photovoltage shows that the film is a n-type material.

Table 5.2: Contact potential difference (CPD), surface photovoltage (SPV), work function (ϕ), ionization energy (E_i) and the energy difference between the Fermi level and the valance band maximum (E_F- E_{vbm}) of $EuZrS_3$ sulfurized at 1000 and 1100 °C.

Sample	Surface cond.	SPV (± 3 mV)	Φ (± 0.04 eV)		E_i (± 0.03 eV)	E_F - E_{VBM} (± 0.05 eV)	
			dark	light		dark	light
$EuZrS_3$/1000°C	air-exp.	6	4.49	4.50	4.77	-0.27	-0.27
$EuZrS_3$/1100°C	N_2-transf.	-5	4.67	4.70	4.77	-0.10	-0.10

Optical-Pump Terahertz-Probe spectroscopy is used to measure the dynamics of photogenerated charge carriers via obtaining photoconductivity transient $\Delta\sigma_\mu$. The photoconductivity transients of $EuZrS_3$ and $BaZrS_3$ can be seen in Fig. 5.9. The rapid decrease in the pattern on decay time shows that $EuZrS_3$ presented here is not suitable for photovoltaic applications.

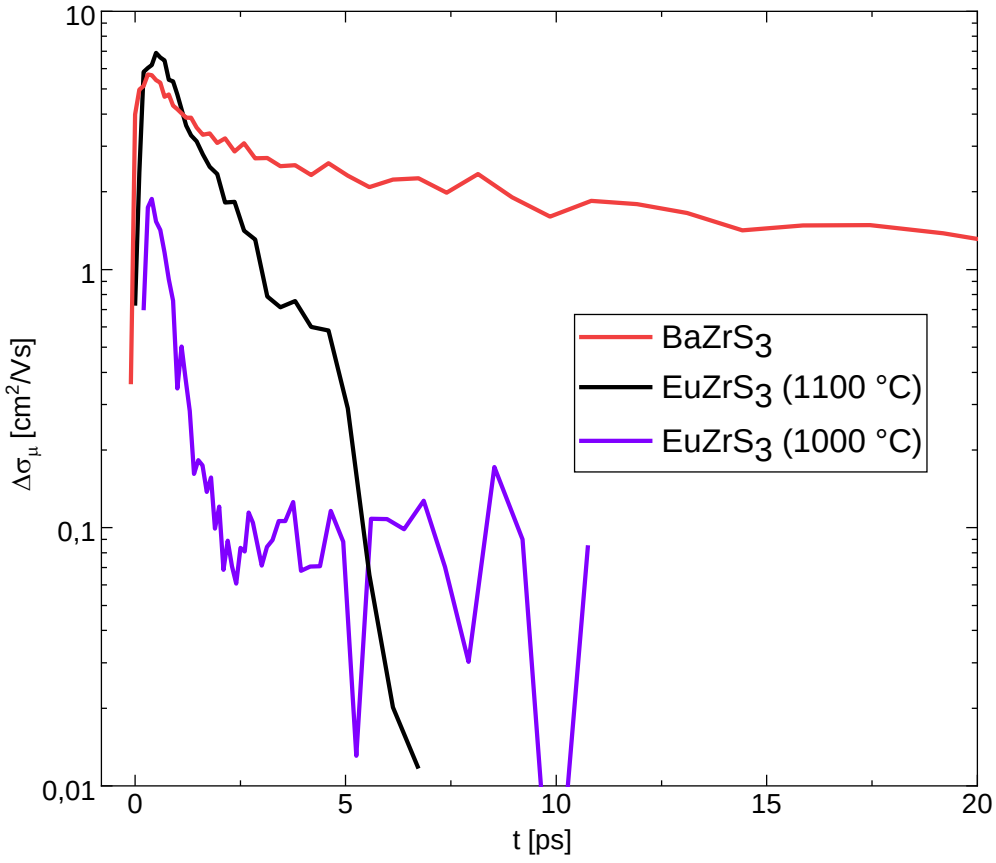

Figure 5.9: Photoconductivity transients of ink-based $EuZrS_3$ sulfurized at 1000 (purple) and 1100 °C (black). And their comparison with ink-based $BaZrS_3$ thin film (red).

5.3. Alloying of $EuZrS_3$ with titanium

So far, the structural and optoelectronic properties of β-$EuZrS_3$ were investigated. However, the alloying properties of $EuZrS_3$ are still unknown. Alloying it with titanium is one of the ways to decrease the band gap, although $EuTiS_3$ alone is not stable in the distorted perovskite structure. So far, it was an unknown as well, if titanium alloying changes the distorted perovskite structure.

As can be seen in Fig. 5.10, the 3% titanium alloyed material has the same peak positions with the needle-like non-perovskite configuration (α-$EuZrS_3$). Even though both alpha and beta phases are present in both graphs, some peaks of the beta phase vanish at 1100 °C, since the amount of the phase is less than 5% in the bulk. Whereas the beta phase is the dominant phase at elevated temperatures for the non-alloyed material, titanium alloying changed the crystal form into the needle-like configuration since titanium perovskites need even higher annealing temperatures to be formed.

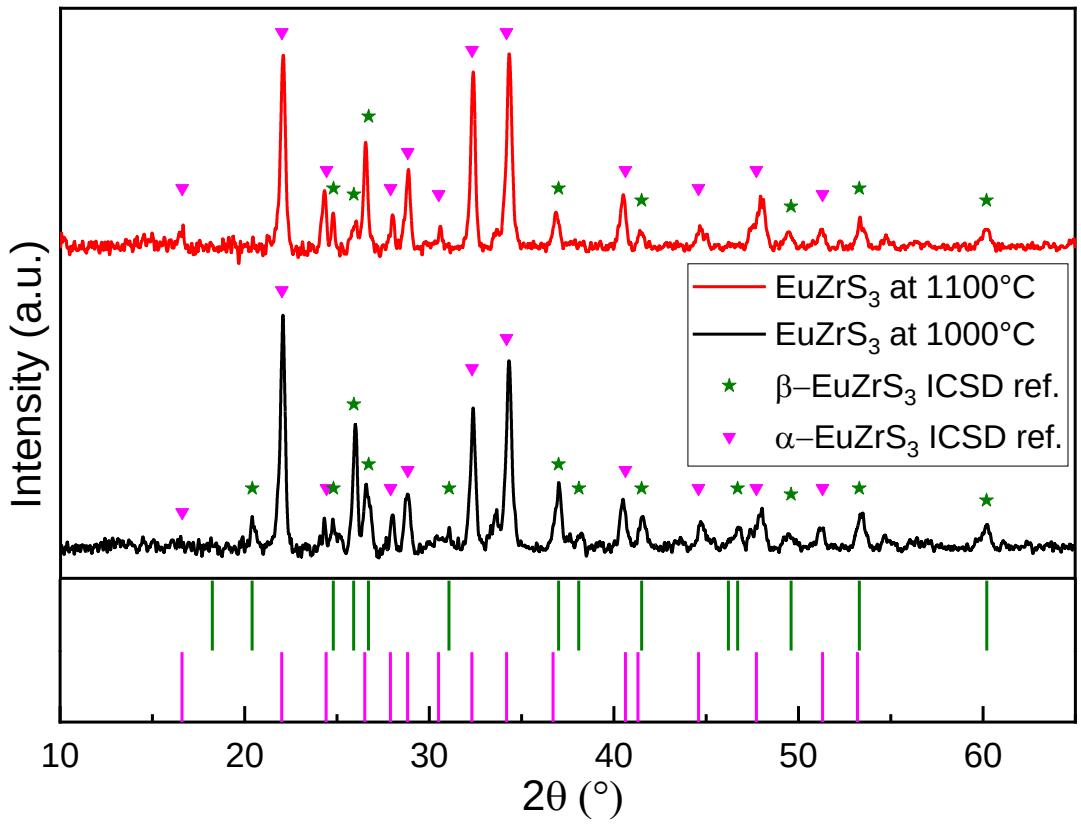

Figure 5.10: Diffractogram comparisons of the titanium alloyed $EuZrS_3$ samples that are sulfurized at 1000 (black) and 1100 °C (red). ICSD reference patterns for alpha (magenta, ICSD-430644) and beta (green, ICSD-631644) phases of $EuZrS_3$.

The lattice parameters of both phases of $EuZrS_3$ are shown in Figure 5.11. According to the values, the lattice parameters obtained by Le Bail analysis confirm that the produced film is in the alpha phase which is in the needle-like non-perovskite configuration.

Material	Lattice parameters at 1° grazing incidence angle					
	a, Å	±	*b*, Å	±	*c*, Å	±
β-$EuZrS_3$	7,085	0.006	9.719	0.007	6.683	0.005
α-$EuZrS_3$	8.451	0.001	3.803	0.001	13.79	0.002

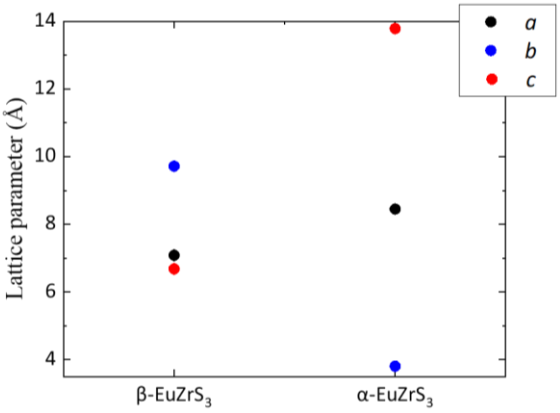

Figure 5.11: Lattice parameters of the titanium alloyed film sulfurized at 1100 °C.

5.4. Conclusions

In conclusion, $EuZrS_3$ thin films are deposited on quartz substrates and formed in the distorted perovskite structure by using the novel ink recipe developed in this work. The elemental composition and the sulfurization degree are determined via XRF analysis. The XRF analysis shows that material needs even higher sulfurization temperature than $BaZrS_3$, which needs 1000 °C, whereas $EuZrS_3$ needs 1100 °C for sulfurization to high degree as can be seen in Table 5.1. The XRF analysis also shows that a small amount of europium is lost during the spin-coating.

The crystal structure is confirmed via XRD measurements by the comparison of material diffractograms with the ICSD database reference patterns. This comparison also shows that the crystals did not have any preferred orientation. Despite a strong charging effect, topography images are taken via SEM to see the domain size which is ~150 nm. XRD and SEM showed that the crystalline domain sizes increased, as the sulfurization temperature increased. Raman spectroscopy data was also collected to be compared with spectra of $BaZrS_3$. In the Raman spectra of the film, the signature peaks for chalcogenide perovskites can be seen slightly moved with some extra peaks which likely belong to europium.

Absorption spectroscopy measurements are conducted to determine the absorbance of the material. By using the derivative of absorbance, the band gap is estimated as 1.68 eV for the film that is sulfurized at 1100 °C, whereas it is 2.07 eV for the film that is sulfurized at

1000 °C. The KP measurement shows that the films have p-type semiconductor material properties. The photoconductivity transients of $EuZrS_3$ and $BaZrS_3$ are compared as well.

Finally, a study of alloying $EuZrS_3$ with titanium was investigated as well. Only 3% of titanium alloying changed the crystal structure from the distorted perovskite to needle-like non-perovskite configuration, rendering it useless for photovoltaic applications in the scope of this work. The crystal structure was confirmed with XRD measurements and the subsequently lattice parameters were obtained by using Le Bail analysis.

To conclude, $EuZrS_3$ in the distorted perovskite structure is produced by using the solution-processed deposition technique. The one produced at 1100 °C has already a promising band gap for tandem solar cells as a top-cell.

CHAPTER 6
INVESTIGATION OF $EuHfS_3$ PEROVSKITE

The only reported study about $EuHfS_3$ is discussed in chapter 1.3.4 in detail. In this chapter, the production process of the $EuHfS_3$ thin film and its material properties for photovoltaic applications are discussed. $EuHfS_3$ only shows the distorted perovskite structure similar to $BaHfS_3$, whereas $EuZrS_3$ has two possible phases to adopt.

To investigate the structural and optoelectronic properties of $EuHfS_3$, first the preparation of the molecular ink is studied. To produce it, iodide, acetate-hydrate and acetylacetonate compounds are used. In the next step, the same parameters of spin-coating and sulfurization for $BaZrS_3$ are applied. As a last step, the material properties are determined by using the measurements introduced in chapter 2.2.

6.1. Preparation of $EuHfS_3$

First, 1.32 mmol of europium acetate-hydrate (Alfa-Aesar, >99.9%) are dissolved in a mixture of 3 mL N-N-dimethylformamide (DMF) (Sigma-Aldrich, 99.9%) and 3 mL acetic acid (Sigma-Aldrich, >99.8%) to prepare the molecular ink solution. 1.99 mmol of hafnium (IV) acetylacetonate powder (Alfa-Aesar, >97%) are added to the mixture afterwards. The prepared solution is stirred in a glovebox at room temperature for half an hour to obtain the clear pale-yellow solution.

In the second step of the thin film preparation, the quartz substrates (1 inch x 1 inch) are rinsed with acetone before spin-coating the molecular ink on them. To reach approximately 90 nm thickness, 240 µL of the precursor solution is taken by a pipette to dispense the ink onto the substrate. The films are spin-coated at 1000 rpm for 10 seconds, and then the spin rate is ramped up in 3 seconds to 3500 rpm and the coating continued for 20 seconds more. After 3 cycles of dynamic dispense spin-coating and the sulfurization, the deposited film reaches approximately 85 nm thickness. To evaporate the solvent residual, substrates are held at 250 °C for 2 minutes in between spin-coating of layers and again at 250 °C for 10 minutes in the end.

Keeping the precursors away from oxygen exposure is key point for this deposition technique. To minimize the oxidation of precursor, spin-coated films are taken out of the glovebox right before sulfurization. Otherwise, the sulfur replacement of oxygen could need more energy.

The samples are put in a quartz boat to place the samples in the furnace quickly. As soon as the quartz boat is put in the middle of the furnace, oxygen in the quartz tube is evacuated, and then the furnace is flushed with argon twice. For the third flushing, 5% H_2S in argon is used to condition the furnace. The flow of sulfurization gas of 5% H_2S (± 0.15 Vol %, Air Liquide) in argon is set to 60 sccm when the valve of the exhaust is opened. The furnace is turned on to heat up when the flow is ready, and it reaches the desired reaction temperature in 30 minutes to replace sulfur. And after another 30 minutes of the sulfurization process at the reaction temperature, the furnace is set to cool itself down naturally. As the temperature reaches down to 400 °C, the gas flow is switched back to pure argon to clear the residual H_2S from the tube. When room temperature is reached, the samples are collected to be measured.

6.2. Results and discussions

A series of samples with different stoichiometric compositions were produced to be used in the measurements to understand the nature of the $EuHfS_3$ material. In this section, the morphological, structural and optoelectronic properties of $EuHfS_3$ thin films were investigated.

6.2.1. Molecular ink preparation route of $EuHfS_3$

Solution-processed $EuHfS_3$ is prepared in the comparable way to -the well-known chalcogenide perovskite- $BaZrS_3$, which the molecular ink was initially created for. It is observed so far in this work that acetylacetonate, isopropoxide and acetate-hydrate compounds can be used instead of acetate as well in this method to be replaced by sulfur during the sulfurization process. Under vacuum, acetate-hydrates can also decompose easily and set the metal part free to react. And unlike most of the metal halides, acetate-hydrates are soluble in organic solvents.

6.2.2. Elemental composition and crystal structure of $EuHfS_3$

The elemental Eu:Hf ratio of the deposited material is measured as 1.00:1.32 (see sample 2 in Table 6.1), although the elemental Eu:Hf ratio of the solution is calculated as approximately 1.00:1.51 according to the molecular ink recipe. Possibly some of the hafnium (IV) acetylacetonate is lost during spin-coating. This loss might occur due to the low surface interaction with the substrate. And some more hafnium (IV) acetylacetonate is lost in the H_2S flow during sulfurization, which is reasonable since hafnium (IV) acetylacetonate is used for chemical vapor depositions. That is why the solution was prepared as hafnium (IV) acetylacetonate rich, however, the stoichiometry was far than expected in the end. A similar

trend of loss during sulfurization was seen during $BaHfS_3$ sulfurization as well. As a result, changes in the elemental ratio of the precursors might occur when different coating conditions are implemented.

X-ray fluorescence (XRF) analysis of the films are performed to investigate the elemental composition. Annealing above a temperature of 1000 °C brings the elemental stoichiometry of Hf-rich films closer to the perovskite structure stoichiometry of 1:1:3, since the hafnium acetylacetonate compound is volatile and used for MO-CVD applications. However, the films are not completely sulfurized. The Eu:Hf ratios for different samples before and after sulfurization can be seen in Table 6.1. The light color of the precursor turns into dark color which might be a sign of sulfurization (see Fig. 6.1). XRF measurements also show that the compositions on different points of the films deviate. A similar trend is present in the $BaZrS_3$ samples with barium acetate but without barium iodide compound, which might happen due to the material loss with the argon-flow of the reactor. This indicates that the mixture usage of iodide and acetate -or its acetylacetonate or isopropoxide replacement- compounds is necessary.

Table 6.1: Elemental composition for $EuHfS_3$ thin films at the sulfurization temperatures of 1000 and 1100 °C. Eu:Hf shows the cation ratio on the precursor films before the sulfurization step. Eu:Hf:S indicates the elemental ratio after sulfurization at given temperature.

Sample number	**Sulfurization temperature (°C)**	**Precursor Eu:Hf (molar %)**		**After sulfurization Eu:Hf:S (molar %)**		
1	1000 °C	1.39±0.01	1.00±0.01	1.34±0.07	1.00±0.06	1.42±0.13
2	1000 °C	1.00±0.08	1.32±0.08	1.00±0.07	1.11±0.02	1.86±0.14
3	1100 °C	1.00±0.09	1.51±0.09	1.00±0.03	1.40±0.08	2.45±0.07

All the main peaks of the orthorhombic $EuHfS_3$-structure (space group $Pnma$ #62), that can be seen in Fig. 6.1, are present on the X-ray diffraction (XRD) patterns. Another interpretation of the diffractograms could be that there are impurities of EuS and HfO_2, when they are compared with the reference patterns of the ICSD database. HfO_2 impurity is formed even with the excess europium due to possible oxidation of the hafnium binary before sulfurization. And EuS is formed even in the hafnium rich films which is the limiting compound of the perovskite formation here. As it can be seen in Fig. 6.1, XRD peaks of EuS are vanishing as the sulfurization temperature increases and the peaks of $EuHfS_3$ gets stronger.

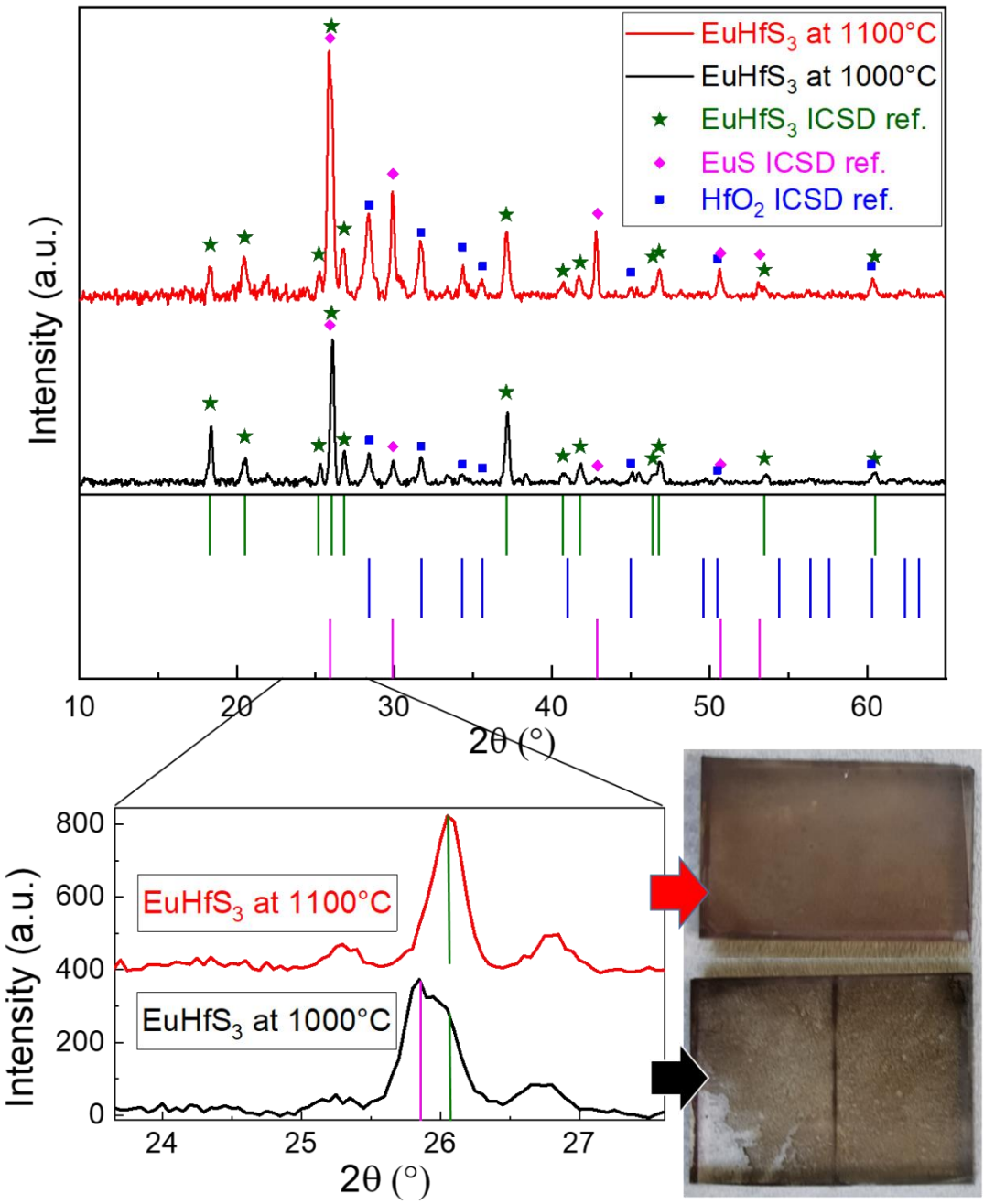

Figure 6.1: Sulfurization of Hf-rich films at 1000 °C (black) and 1100 °C (red) for 30 minutes. ICSD database references for $EuHfS_3$ with the orthorhombic perovskite structure (ICSD-631329, green), HfO_2 (ICSD-27313, blue) and EuS (ICSD-657615, magenta).

The Raman spectrum for the ink-based $EuHfS_3$ thin film and the Raman spectra of $EuZrS_3$ and $BaZrS_3$ thin films, for the purpose of comparison, are shown in Figure 6.2. The overlapping of the peak positions of $EuZrS_3$ and $EuHfS_3$ stems from the similar ionic radii of Hf and Zr for six-coordination which are 0.71 and 0.72 Å respectively.[28] Due to the same reason, a similar pattern can be seen in chapter 4.2.2 for $BaZrS_3$ and $BaHfS_3$. The remaining peaks that do not project on $BaZrS_3$ peaks can be assigned to vibrational modes of compounds with europium, as they are there for $EuZrS_3$ too.

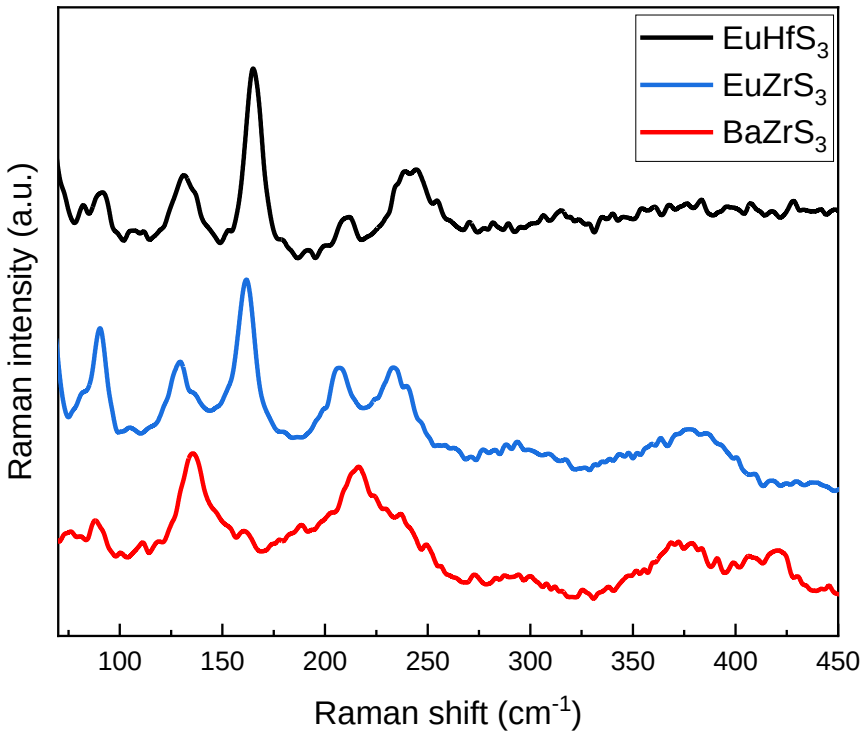

Figure 6.2: Raman spectra of Hf-rich $EuHfS_3$ film sulfurized at 1100 °C (black), $EuZrS_3$ film sulfurized at 1100 °C (blue) and $BaZrS_3$ film sulfurized at 1000 °C (red) that are measured at room temperature for 60 seconds each.

To investigate the effect of different sulfurization temperatures on crystallinity, scanning electron microscopy measurements are performed. It can be seen in the SEM images that the grain size reached more than ~1 µm at 1100 °C (see Fig. 6.3). The XRD patterns show that there are perovskite formations at both reaction temperature. And in both images very small HfO_2 crystallites can be seen as well.

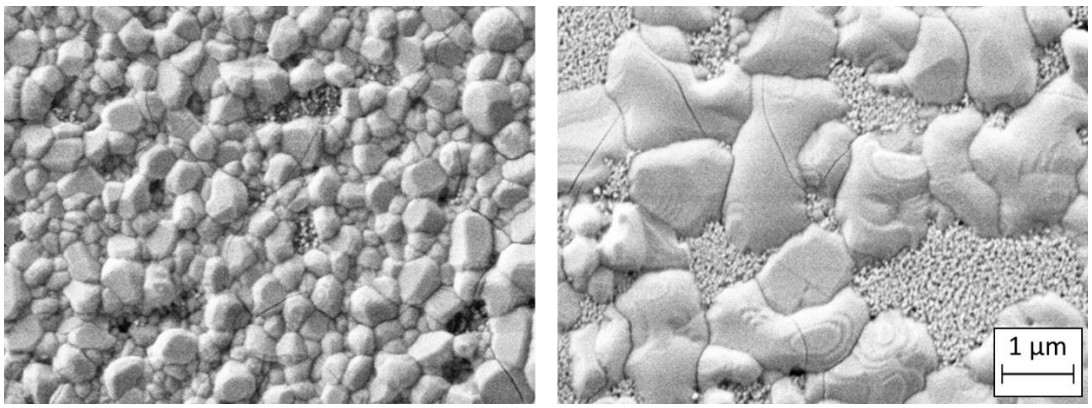

Figure 6.3: SEM images of the $EuHfS_3$ thin films for the sulfurization temperature of 1000 °C (left) and 1100 °C (right). The scale applies to both images.

6.2.3. Optoelectronic properties of $EuHfS_3$

To calculate the absorbance, transmittance and reflectance were measured with the UV-Vis spectroscopy. As seen in Fig. 6.4, the absorbance of the film is low. This might be too low due to the film thickness compared to samples covered in previous chapters, as the absorbance is dependent on the path length through the sample. Due to poor absorbance signal quality, the method used in this work to determine the band gap is not applicable here.

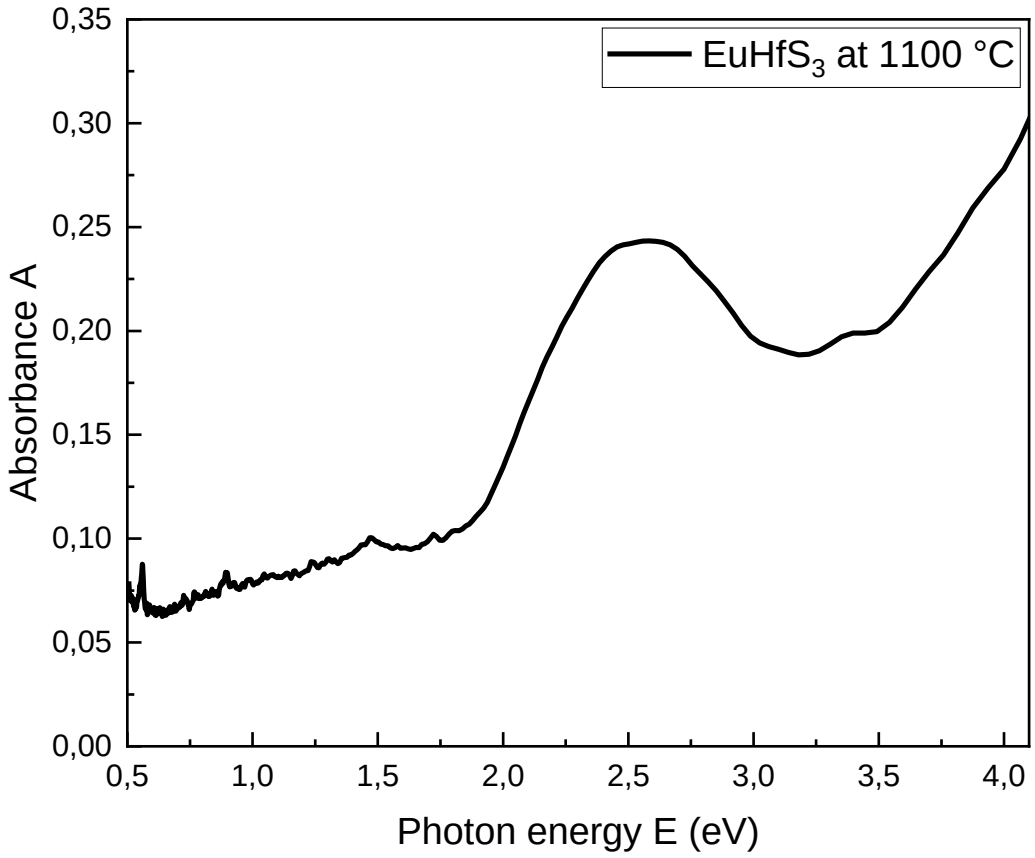

Figure 6.4: Absorbance for the $EuHfS_3$ film, which is sulfurized at 1100 °C for 30 minutes.

The ionization energy and the density of states (DOS) are measured by using Photoelectron Yield Spectroscopy (PYS) which is using the derivative of the photoemission current. These measurements were done under nitrogen atmosphere with photon energies as shown in Fig. 6.5. From the KP and PYS measurements the ionization energy of the solution-processed $EuHfS_3$ material can be determined as ~5.74 eV.

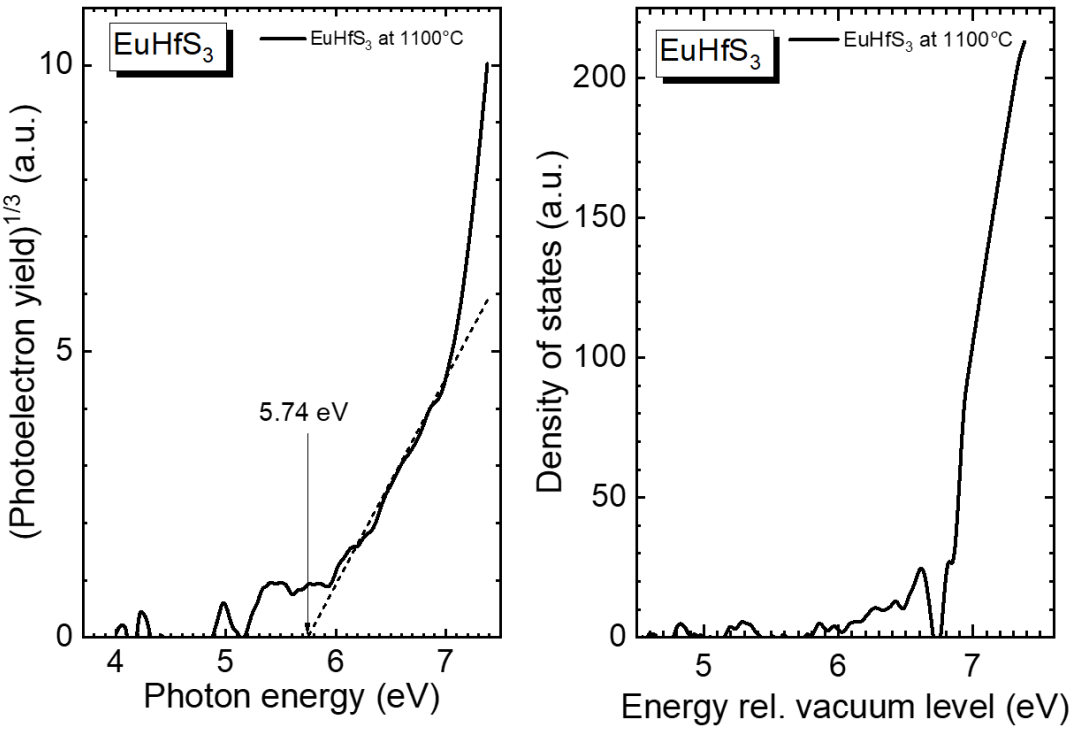

Figure 6.5: Ionization energy (left) and density of states (right) of the $EuHfS_3$ films sulfurized at 1100 °C.

Kelvin-Probe (KP) was difficult to measure for the $EuHfS_3$ thin film, due to the charging effect of the material. The work function of the film is recorded directly from the oscilloscope (see Table 6.2) which is approximately 4.46 eV. The samples are illuminated by a 532 nm laser. The difference between dark and light measurements gives the surface photovoltage which did not change, as can be seen in Table 6.2.

Table 6.2: Contact potential difference (CPD), surface photovoltage (SPV), work function (ϕ), ionization energy (E_i) and the energy difference between the Fermi level and the valance band maximum (E_F- E_{vbm}) of $EuHfS_3$ sulfurized at 1100 °C.

Sample	Surface cond.	SPV (± 3 mV)	Φ (± 0.04 eV)		E_i (± 0.03 eV)	E_F - E_{VBM} (± 0.05 eV)	
			dark	light		dark	light
$EuHfS_3$/QG	N_2-transf.	0	4.46	4.46	5.74	-1.29	-1.29

Optical-Pump Terahertz-Probe spectroscopy is used to measure the dynamics of photogenerated charge carriers via obtaining photoconductivity transient $\Delta\sigma_\mu$ of materials. The photoconductivity transients of $EuHfS_3$, $EuZrS_3$ and $BaZrS_3$ can be seen in Fig. 6.6.

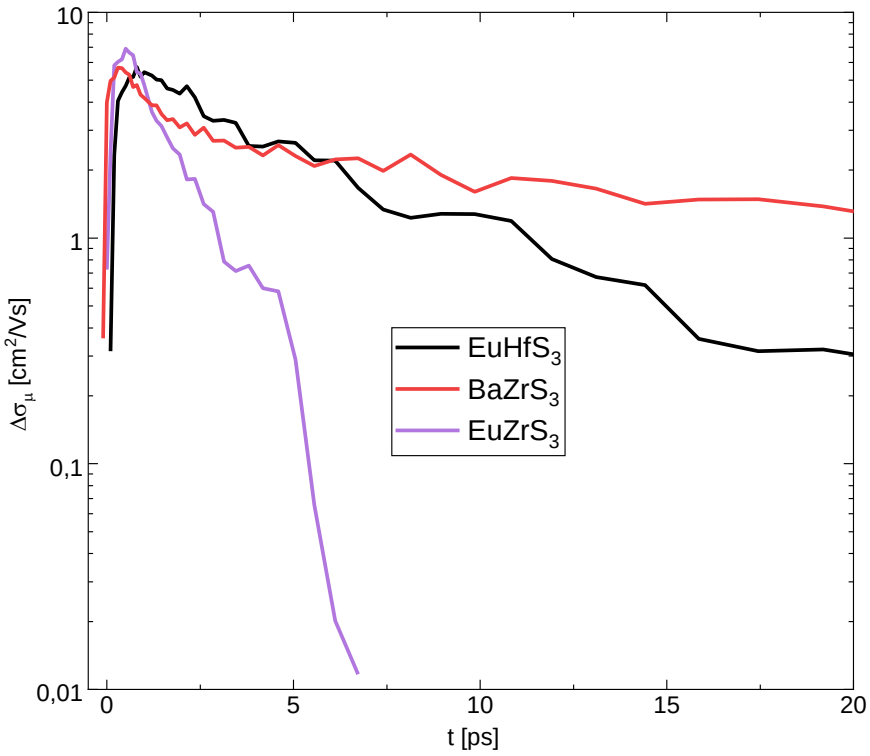

Figure 6.6: Photoconductivity transients of ink-based $EuHfS_3$ thin film sulfurized at 1100 °C (black). And its comparison with ink-based $BaZrS_3$ thin film (red) sulfurized at 1000 °C and $EuZrS_3$ thin film (purple) sulfurized at 1100 °C.

A fast decay -as shown by $BaZrS_3$ in the first ps- is not observed for the $EuHfS_3$ thin film. $EuHfS_3$ has longer decay time in comparison with $EuZrS_3$. The pattern of decay time shows that $EuHfS_3$ might be promising for photovoltaic applications if the carrier lifetime can be prolonged by elimination of defects.

6.3. Conclusions

Overall, the molecular ink recipe developed for the chalcogenide perovskite production is applied with the precursor binaries of europium and hafnium. $EuHfS_3$ thin films are prepared by the sulfurization of deposited precursors. Hf-rich compositions are investigated to determine the effects of different sulfurization temperatures. It can be seen in XRF measurements that the reaction temperature of 1100 °C is mandatory to reach higher sulfurization amounts. XRD measurements show that $EuHfS_3$ is formed in the distorted perovskite phase successfully.

Similar to previously studied materials, bigger crystal sizes are imaged with SEM as the reaction temperature increases. HfO_2 crystallites can be observed in SEM images as well which are detected by XRD as well.

The measurements in the optoelectronic properties were a little problematic due to the low film thickness and impurity of the side products. Nevertheless, the ionization energy of 5.74 eV, the work function of 4.46 eV and the photoconductivity transient are measured.

The investigation of the $EuHfS_3$ thin film material reveals that a possible suitability for the application as absorber materials in solar cells, if the material can be produced without impurities. The material needs further improvements to determine a clear band gap value, which is necessary for usage in devices and for band gap engineering.

CHAPTER 7
INVESTIGATION OF $SrHfS_3$ PEROVSKITE

The literature survey about the $BaHfS_3$ studies is reported in chapter 1.3.5. This chapter contributes to an understanding of the production process of $SrHfS_3$ thin films and its material properties for photovoltaic applications. So far, it has been reported that $SrHfS_3$ only shows the distorted perovskite structure, similar to $BaHfS_3$ and $EuHfS_3$.[28,40]

The experimental steps to determine a clear synthesis route start with the molecular ink preparation of $SrHfS_3$. It's fundamental principles are discussed in chapter 2.1.1. For the preparation, strontium iodide, strontium acetate and hafnium (IV) acetylacetonate binaries are used. The spin-coating and sulfurization parameters are adapted from the $BaZrS_3$ chapter (see chapter 3.1) as well. At last, the optimal sulfurization conditions are determined for this material, and material properties are investigated as a promising semiconductor.

7.1. Preparation of $SrHfS_3$

To prepare the molecular ink of $SrHfS_3$, 0.36 mmol of strontium iodide (Alfa-Aesar, >99.99%), 1.26 mmol of strontium acetate (Sigma-Aldrich, 99.95%) are dissolved in a mixture of 3 mL N-N-dimethylformamide (DMF) (Sigma-Aldrich, 99.9%) and 3 mL acetic acid (Sigma-Aldrich, >99.8%). Then 2.05 mmol of hafnium (IV) acetylacetonate powder (Alfa-Aesar, >97%) are added to the mixture. The prepared solution is stirred in a glovebox at room temperature for half an hour to obtain a murky pale-yellow solution.

Quartz substrates (1 inch x 1 inch) are used for the thin film deposition after they are rinsed with acetone. To spin-coat the solution on substrates, 250 µL of the precursor solution is taken by a pipette to dispense. The films are spin-coated at 1000 rpm for 10 seconds, and then the spin rate is ramped up in 3 seconds to 3500 rpm and the coating continued for 20 seconds more. After 1 cycle of dynamic dispense spin-coating and the sulfurization, the deposited film reaches approximately 187 nm thickness. Substrates are held at 250 °C for 2 minutes in between spin-coating of layers and are held also at 250 °C for 10 minutes in the end, to evaporate the solvent residual.

To minimize the precursor oxidation, spin-coated films are kept in glovebox, and they are taken out right before sulfurization since the sulfur replacement of oxygen needs more energy. The samples are put in a quartz boat to place them in the furnace as soon as possible. When

the quartz boat is placed in the middle of the furnace, oxygen in the quartz tube can be evacuated. Firstly, the furnace is evacuated, and then flushed with argon twice. The furnace is flushed with 5% H_2S in argon for the third flushing. The flow of sulfurization gas is initiated when the valve of the exhaust is opened. The reactive gas flow is set to 60 sccm of 5% H_2S (± 0.15 Vol %, Air Liquide) in argon. When the flow is ready, the furnace is turned on to heat up. And the desired reaction temperature for sulfur replacement is set to be reached in 30 minutes. After another 30 minutes of the sulfurization process, the furnace is left to cool itself down naturally. When the temperature reaches down to 400 °C, the gas flow is changed back to pure argon to evacuate the residual H_2S in the tube. When the samples cool down to room temperature, they are collected. The fundamental principles of sulfurization are discussed in chapter 2.1.3.

7.2. Results and discussions

Preliminary experiments of the $SrHfS_3$ thin film were conducted to study its structural, compositional, and morphological properties. The results of the measurements are discussed in the following sections.

7.2.1. Molecular ink preparation route of $SrHfS_3$

Solution-processed $SrHfS_3$ is prepared in a similar way as $BaZrS_3$, which the molecular ink is designed for. Only the metal ions are changed, and hafnium precursor is picked as acetylacetonate since hafnium acetate is not available commercially. Under vacuum, acetylacetonates can decompose easily and set the metal part free to react (see chapter 2.1.3). Unlike most of the metal halides, acetylacetonates are soluble in organic solvents.

7.2.2. Elemental composition and crystal structure of $SrHfS_3$

The elemental Sr:Hf ratio of the deposited material has been measured as 1.00:1.16 (see Table 7.1), although the elemental Sr:Hf ratio of the solution is approximately 1.00:1.27 according to the molecular ink recipe. Possibly some of the hafnium (IV) acetylacetonate is lost during spin-coating due to the low surface interaction with the substrate. Hence, changes in the elemental ratio should be considered when different conditions of coating are implemented.

X-ray fluorescence (XRF) analysis shows that the films are sulfurized poorly at 1100 °C. The Sr:Hf ratios before and after sulfurization can be seen also in Table 7.1. Moreover, the pale-yellow color of the precursor turns into pale-green color which might be a sign of sulfurization (see Fig. 7.1).

Table 7.1: Elemental composition of the $SrHfS_3$ thin film at the sulfurization temperature of 1100 °C. Sr:Hf shows the cation ratio on the precursor films before the sulfurization step. Sr:Hf:S indicates the elemental ratio after sulfurization at given temperature.

Sulfurization temperature (°C)	**Precursor Sr:Hf (molar %)**		**After sulfurization Sr:Hf:S (molar %)**		
1100 °C	1.00±0.03	1.16±0.03	1.00±0.05	1.16±0.05	1.73±0.08

All the prominent peaks of the orthorhombic $SrHfS_3$-structure reference (space group *Pnma* #62), that can be seen in Fig 7.1, are present on the samples X-ray diffraction (XRD) patterns. Another interpretation of the diffractograms could be that there is no preferred orientation for the crystals since the diffractogram peaks of the reference powder sample have the similar intensity pattern with the reference peaks of the powder sample of the ICSD database. At 1100 °C, HfO_2 crystals are formed due to the excess hafnium.

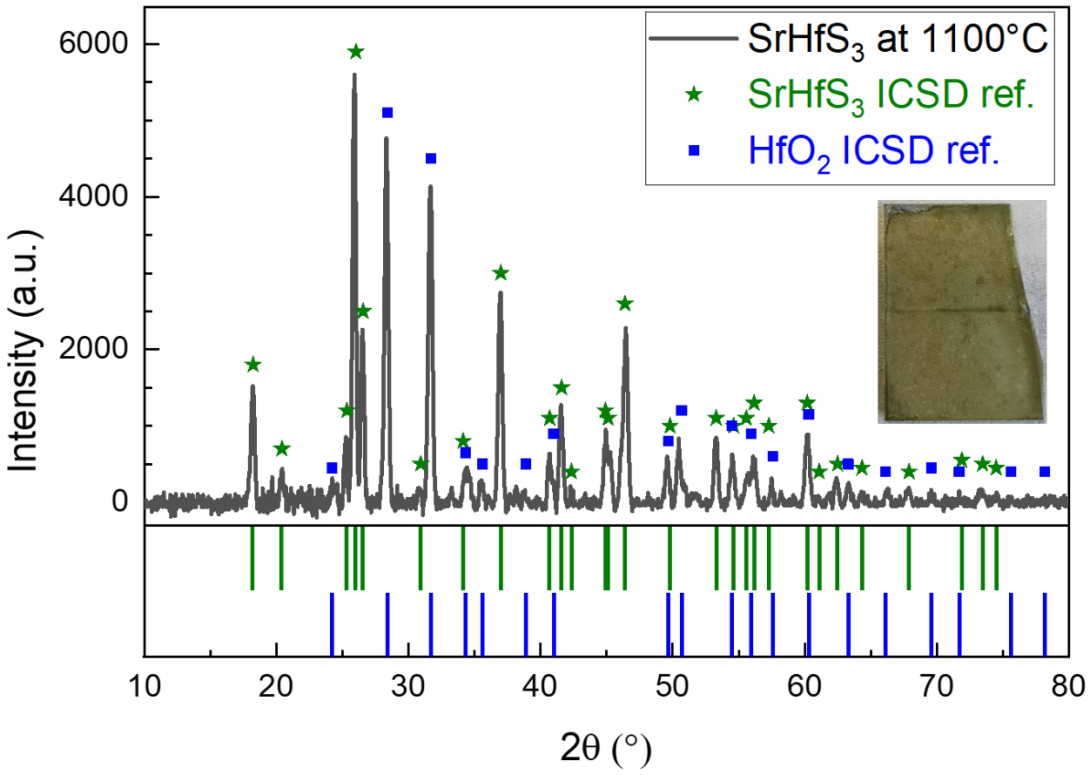

Figure 7.1: Sulfurization of $SrHfS_3$ film at 1100 °C (black) for 30 minutes. ICSD database references for $SrHfS_3$ with the orthorhombic perovskite structure (ICSD-631329, green) and HfO_2 (ICSD-27313, blue).

The Raman spectra of the $SrHfS_3$ thin film, the $EuHfS_3$ thin film (see chapter 6.2.3) and ink-based $BaZrS_3$ thin film (see chapter 3.2.3) can be seen in Figure 7.2. A similarity in peak positions of $EuHfS_3$ and $SrHfS_3$ can be observed since ionic radii of Sr and Eu with 2+ oxidation state are close to each other.[41] Thus they are showing these respective vibrational modes belong to compounds which occur in both materials or to compounds which have similar properties. And there peaks which can be attributed to the well-known $BaZrS_3$ perovskite due to similar vibrational modes.

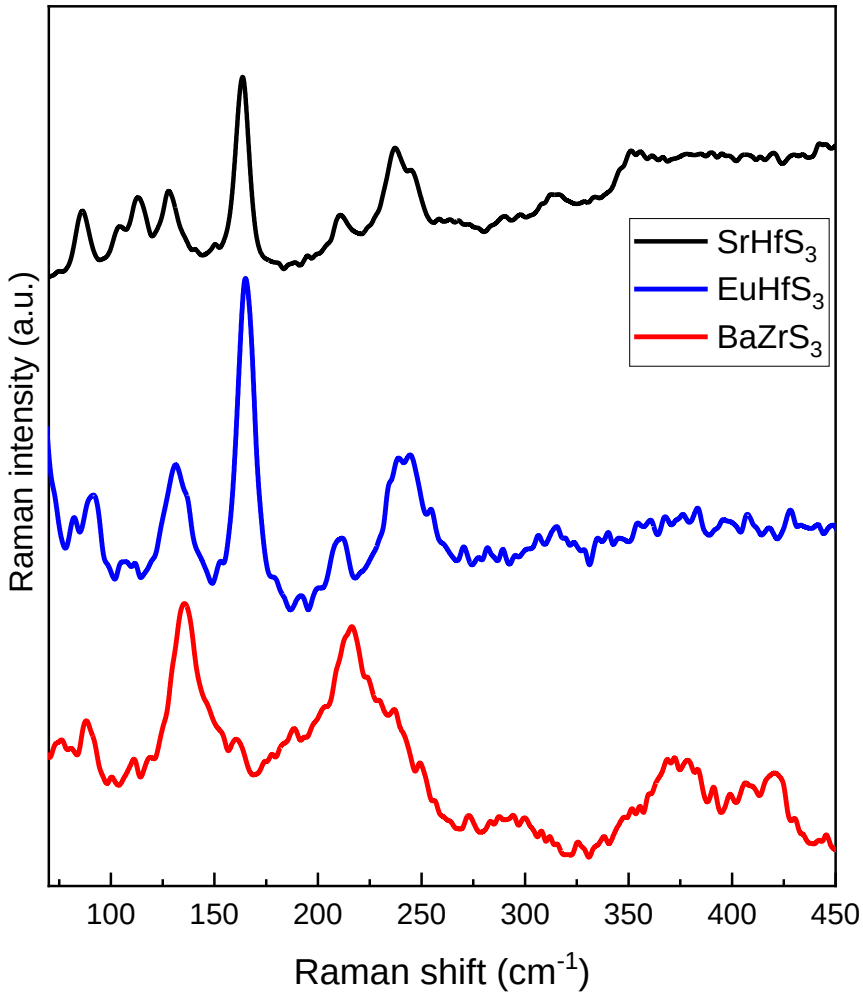

Figure 7.2: Raman spectra of $SrHfS_3$ film sulfurized at 1100 °C (black), $EuHfS_3$ film sulfurized at 1100 °C (blue) and $BaZrS_3$ film sulfurized at 1000 °C (red) that are measured at the room temperature for 60 seconds.

It can be seen in the scanning electron microscopy (SEM) images that the crystal size reached ~400 nm at 1100 °C (see Fig. 7.3). Because of the charging effect whose signs can already be seen on the top of the right image as a shift, going up to higher magnifications was not possible. The EDX measurement could not be done for to the same reason.

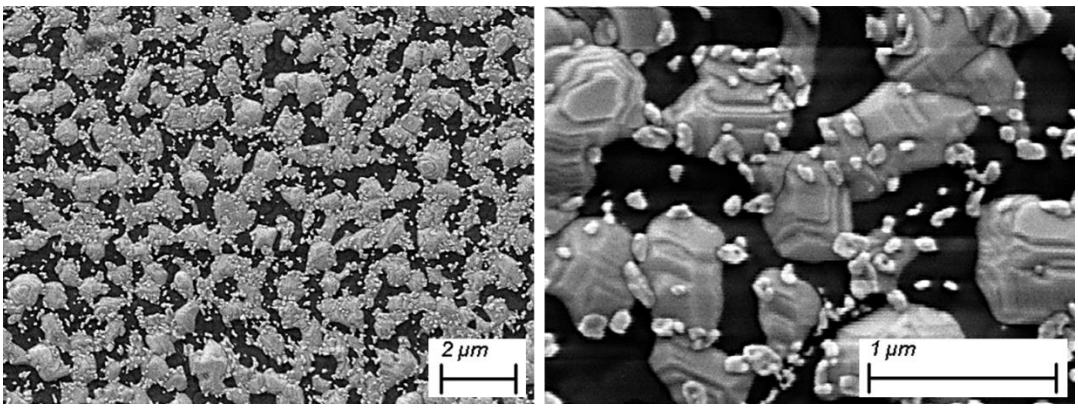

Figure 7.3: SEM images of the $SrHfS_3$ thin film at different scales for the sulfurization temperature of 1100 °C.

7.2.3. Optoelectronic properties of $SrHfS_3$

Optical-Pump Terahertz-Probe spectroscopy is used to measure the dynamics of photogenerated charge carriers via obtaining photoconductivity transient $\Delta\sigma_\mu$. The comparison of photoconductivity transients for $SrHfS_3$, $EuHfS_3$, $BaHfS_3$ and $BaZrS_3$ can be seen in Fig. 7.4. Compared to $BaZrS_3$, $SrHfS_3$ has lower mobility (initial amplitude). However, the pattern on decay time shows that $SrHfS_3$ is more promising than $BaHfS_3$ for photovoltaic applications, although this sample of $SrHfS_3$ has the impurity of HfO_2 in the bulk.

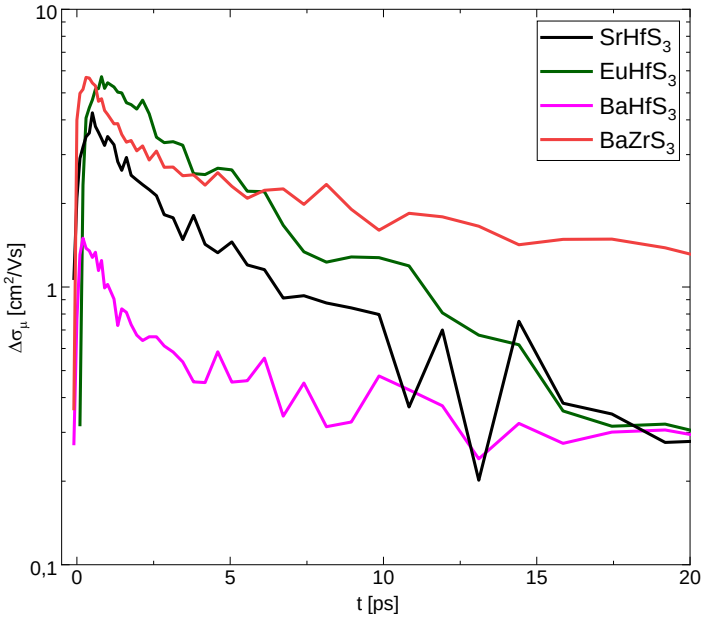

Figure 7.4: Photoconductivity transients of ink-based $SrHfS_3$ thin film sulfurized at 1100 °C (black). And their comparison with ink-based $EuHfS_3$ (green), $BaHfS_3$ (magenta) thin films sulfurized at 1100 °C and $BaZrS_3$ thin film (red) sulfurized at 1000 °C.

Guo *et al*. also reported the $SrHfS_3$ structure is a promising material for green light emitting diodes due to its strong nature against defects.[41] When the need in green-range emission is considered, it is worth investigating $SrHfS_3$ in detail in the future.

7.3. Alloying of $SrHfS_3$ with europium

Alloying changes the properties of materials, e.g., band gap, semiconductor type or stable crystal phase. In this subchapter, the results of $SrHfS_3$ alloying with europium are investigated.

Fig. 7.5 shows the diffractogram of europium alloyed $SrHfS_3$. From the diffractogram it can be concluded that the material has HfO_2 impurities, possibly due to an already oxidized Hf binary used in the molecular ink. The XRD peaks of the two pure perovskites are remarkably close to each other. Hence the XRD peaks of the hybrid material are slightly shifted from one to another as it can be seen in the right image of the Fig. 7.5.

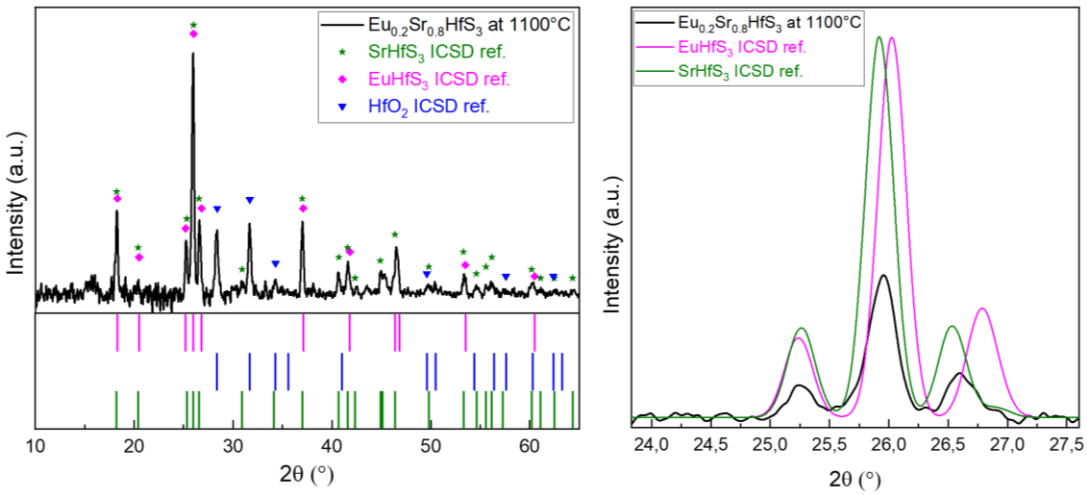

Figure 7.5: XRD patterns of europium alloyed $SrHfS_3$ films sulfurized at 1100 °C (black) for 30 minutes. ICSD database references for HfO_2 (ICSD-27313, blue), $EuHfS_3$ (ICSD-631329, magenta), and $SrHfS_3$ (ICSD-631329, green) with the orthorhombic perovskite structure.

In Fig. 7.6, a similar shift on the Raman spectra can be seen as well. Despite that the ionic radii of Eu^{2+} is close to earth-alkali metals, change in the lattice parameters affects the molecular interactions.[41] There is also a shift on the Raman peaks due to the changings in the lattice parameters which obeys the Vegard's Law.[55]

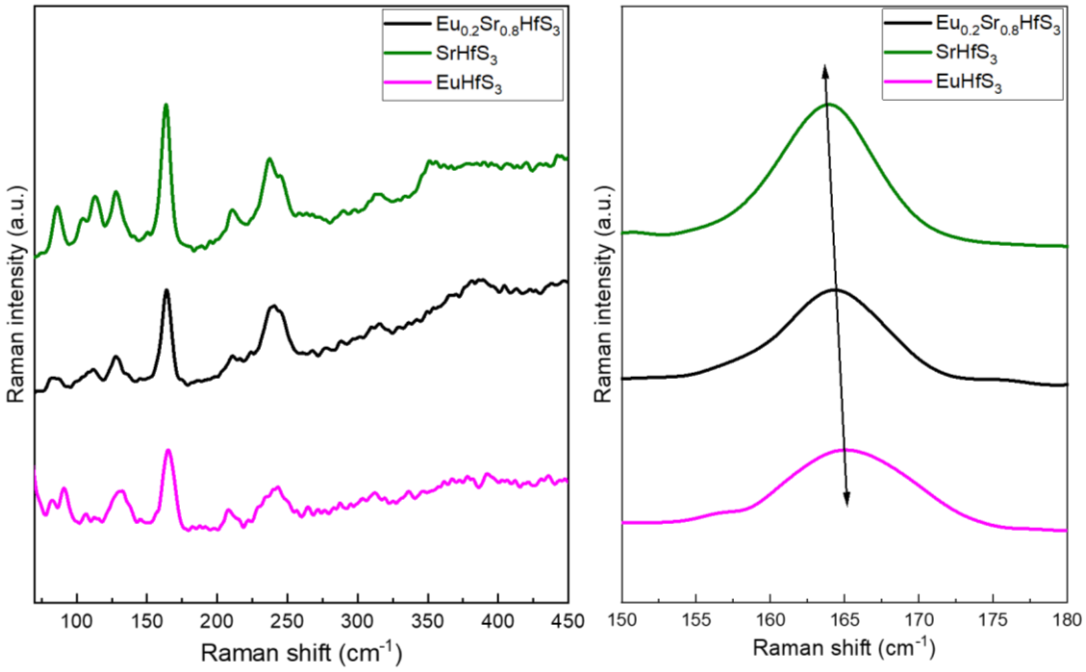

Figure 7.6: Raman spectra of $Eu_{0.2}Sr_{0.8}HfS_3$ (black) $EuHfS_3$ (magenta) and $SrHfS_3$ (green) films sulfurized at 1100 °C that are measured at the room temperature for 60 seconds.

$SrHfS_3$ is used for green LEDs due to its high photoluminescent properties.[40] However as can be seen in Fig. 7.7, obtaining a better coverage on a quartz substrate is easier as europium amount increases, since the pure $EuHfS_3$ has bigger grains and the one with 20% europium still has bigger grains compared to other mixtures with lower europium content, even though its coverage here does not look good since the film is deposited from a low concentration solution. A study on the concentrations of these mixtures might be useful for future thin film technologies.

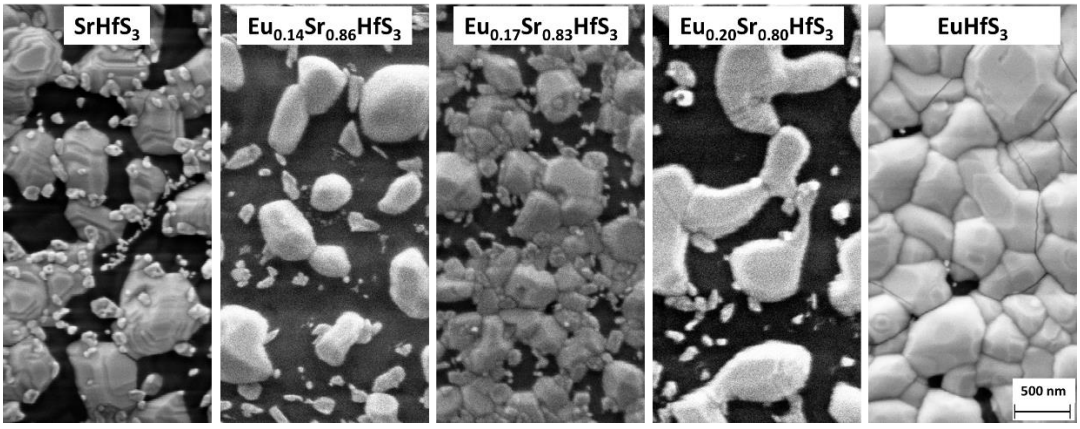

Figure 7.7: SEM images of Eu-alloyed $SrHfS_3$, pure $SrHfS_3$ and pure $EuHfS_3$ films sulfurized at 1100 °C for 30 minutes.

The aim of alloying these materials was to decrease the reported band gap of $SrHfS_3$ (2.37 eV), however the band gaps for none of these materials were measured with the methods that are used in whole of this study due to poor quality of thin films, e.g. HfO_2 impurity, bad coverage etc.[40]

7.4. Conclusions

To conclude, $SrHfS_3$ thin films are prepared at the reaction temperature of 1100 °C from the molecular ink developed for chalcogenide perovskites. XRF results show that sulfurization degree to form a 1:1:3 ratio of the perovskite homogenously throughout the sample is not high, due to the difficult sulfurization nature of HfO_2.

On the other hand, XRD measurements show that $SrHfS_3$ is formed in the distorted perovskite phase with the HfO_2 secondary phase due to the oxidized Hf source. The peaks in the XRD diffractograms are indexed according to the ICSD standard diffractograms. Based on the XRD measurements and analysis, the crystalline material has no preferred orientation. The HfO_2 grains measured with XRD can be seen in SEM images as well. The Raman spectra is obtained and compared with other chalcogenide thin films produced in this study. The signature Raman peaks for chalcogenide perovskites are present in this film as well.

Similar to previously studied titanium alloyed-materials (e.g. $BaZrS_3$ and $EuZrS_3$), the $SrHfS_3$ thin film is alloyed with europium to decrease the reported band gap of 2.37 eV. XRF measurements are used to determine the changes in the mixing ratio of alloys, and XRD confirms the structural properties of the alloyed materials. SEM imaging shows that the alloyed film has bigger grains on the quartz substrate. Further measurements were not conducted due to the impurity in the material and poor quality of thin films.

Current commercially available LEDs (GaN, InGaN, etc.) have a severe problem due to the drop in the quantum efficiency in the wavelength range around the green region (E_g = 2.18-2.50 eV), which is called the “green gap problem”. $SrHfS_3$ might be a promising material to remove this deficiency with its reported experimental band gap of 2.3 eV.[40,75,76]

CHAPTER 8
DIRECT SELENIZATION OF Sr-Sn COMPOUNDS

This study is performed to understand the nature of the $SrSnSe_3$ thin film and its material properties for photovoltaic applications. As it is discussed in chapter 1.3.6, it was reported that $SrSnSe_3$ shows the properties of the distorted perovskite structure with a direct band gap of 1.00 eV.[24] The adsorption-controlled growth studies of Filippone *et al*. calculated that the partial pressure of SrSe is higher than the BaSe partial pressure which is the driving force for the perovskite formation.[32] As a result of these studies, it is likely to produce $SrSnSe_3$ at lower reaction temperature of 1000 °C as it is used for other chalcogenide perovskites in this work.

For the Experimental steps, various compounds of Sr and Sn are used. For the preparation, strontium chloride, strontium chloride hexahydrate, strontium iodide, strontium acetate, strontium acetylacetonate, tin (IV) chloride, tin (IV) iodide and tin (IV) acetate binaries are used. The spin-coating parameters from the chapter 2.1.2 are used for this material as well. In the end, the optimal selenization conditions are determined to selenize the materials fully.

8.1. Preparation of Sr-Sn precursor

To prepare the molecular ink of Sr-Sn-Se precursor, 0.36 mmol of strontium acetate (Sigma-Aldrich, 99.95%) or strontium acetylacetonate hydrate (Alfa-Aesar, >99.99%) is dissolved in 3 mL of N-N-dimethylformamide (DMF) (Sigma-Aldrich, 99.9%). Then 0.4 mmol of tin (IV) acetate powder (Alfa-Aesar, >97%) or tin (IV) chloride (Sigma-Aldrich, 98%) is added to the mixture. The prepared solution is stirred in a glovebox at room temperature for half an hour to obtain a pale-yellow solution. Because less energy is needed to replace sulfur with selenium compared to replacing oxygen; thiourea or thioacetamide is used as a so-called catalyst. To satisfy the charge balance of 1:1:3 ratio for the perovskite structure, 1.2 mmol thiourea or thioacetamide is used.

Soda-lime glass substrates (1 inch x 1 inch) are used for the thin film deposition after they are rinsed with acetone. To spin-coat the solution on substrates, a pipette is used to take 250 µL of the precursor solution to dispense. The films are spin-coated dynamically at 500 rpm for 10 seconds, and then the spin rate is ramped up in 3 seconds to 1500 rpm and the coating continued for 20 seconds more. 5 cycles of spin-coating are done. Substrates are held at 220 °C

for 2 minutes in between spin-coating of layers and are held also at 220 °C for 10 minutes in the end, to evaporate the solvent residual.

To minimize the oxidation amount, spin-coated films are kept in glovebox, and they are taken out right before selenization since the selenium replacement of oxygen needs more energy. The samples are put in a graphite box with selenium chunks to place them into the custom-made selenization furnace (see chapter 2.1.3.2) quickly. When the graphite box is placed into the cold zone of the furnace, oxygen in the tube furnace can be evacuated. Firstly, the furnace is evacuated, and then flushed with nitrogen twice. When the temperature reaches the desired reaction temperature, the graphite box is put to the hot zone (see Fig. 2.3). After 30 minutes of selenization process, the graphite box is taken to the cool zone. When the samples cool down to room temperature, they are collected.

8.2. Results and discussions

$SrSnSe_3$ was introduced as a promising material in the literature as mentioned in chapter 1.3.6. The results of the investigation of its compositional and structural properties are discussed in the following sections.

8.2.1. A Molecular ink preparation route of Sr-Sn precursor

$SrSnSe_3$ is aimed to be prepared by the solution-processed method in a similar way to $BaZrS_3$, which the molecular ink is designed for. Strontium acetylacetonate and strontium acetate precursors are picked since strontium chloride and high amount of strontium iodide are not dissolving in anhydrous-DMF fully. On the other hand, tin (IV) chloride and tin (IV) acetate are picked for tin selenization since tin (IV) iodide is not soluble in anhydrous-DMF as well. Under vacuum, acetylacetonates decomposes easily and set the metal part free to react (see chapter 2.1.3), whereas high amounts of iodide are difficult to replace due to their stronger bonds. In early trials, thiourea or thioacetamide was used to form bisthiourea-metal acetate chelates with acetate compounds which forms sulfide compounds after thermal decompositions.[51,77] However, these sulfur source materials react with oxygen filters of gloveboxes due to similarity in the chemical properties of sulfur and oxygen. Hence, they were not used in the late phase.

8.2.2. Selenization of binaries and their crystal structure of Sr-Sn precursor

The first study of binary selenization started with chloride binaries. The mixture of strontium chloride and tin (IV) chloride binaries is heated at 542 °C for 30 minutes with 100 mg

selenium chunks. As can be seen in the XRD pattern in Fig. 8.1, only the tin compound is selenized. Strontium chloride might be staying non-oriented in the film. On the other hand, the peaks of tin (IV) selenide -including one extraordinarily strong peak- show a crystallization with a preferred orientation. This peak gets even stronger when the $SnSe_2$ is produced from tin (IV) acetate.

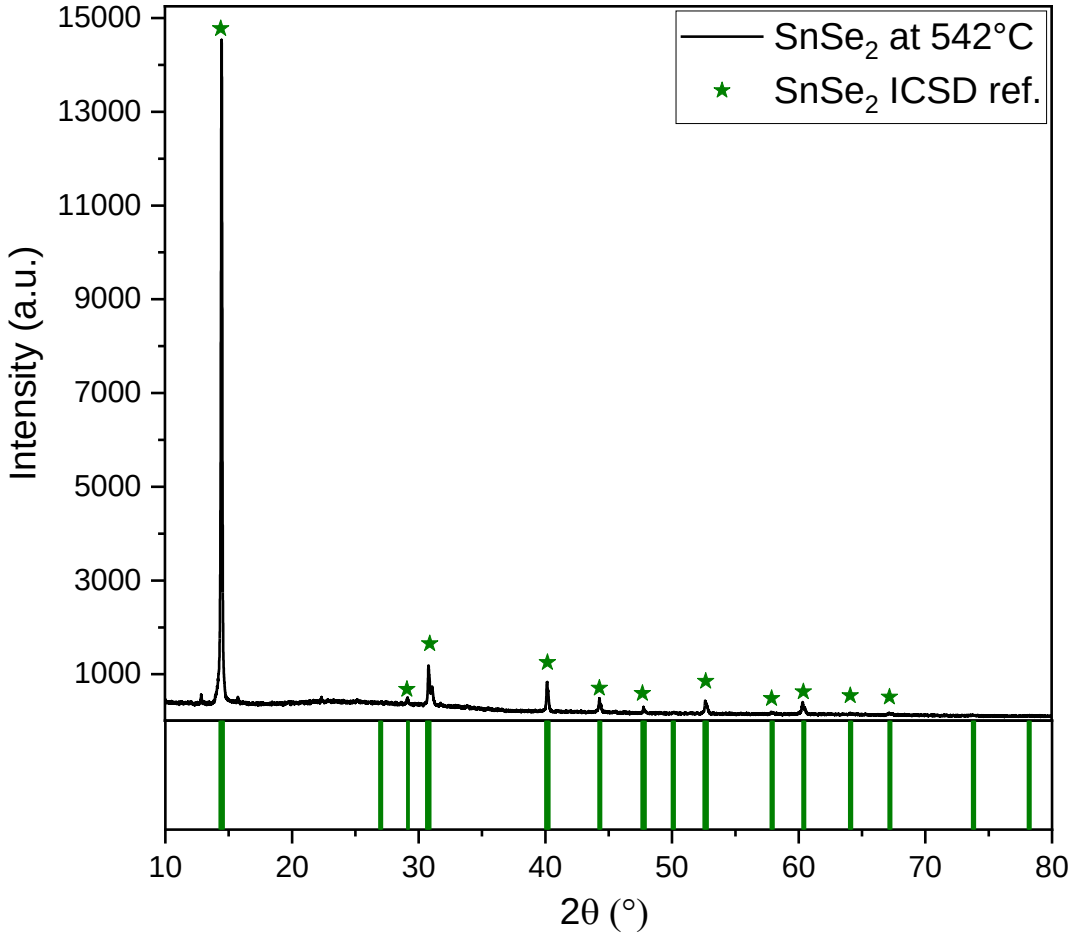

Figure 8.1: XRD pattern of the $SnSe_2$ film that is selenized from tin (IV) chloride at 542 °C (black) for 30 minutes. ICSD database references (below) for SrSe powder (ICSD-230887, green).

Strontium chloride hexahydrate is more problematic than the anhydrous strontium chloride. Water should be eliminated in the setup by using annealing first, since the perovskite formation reactions are sensitive to moisture. Strontium chloride can be seen in Fig 8.2 as accumulations of strontium and chlorine at the same positions of EDX measurements. On the other hand, the tin mapping aligns with the selenium mappings, which is a sign of selenization as well as the XRD.

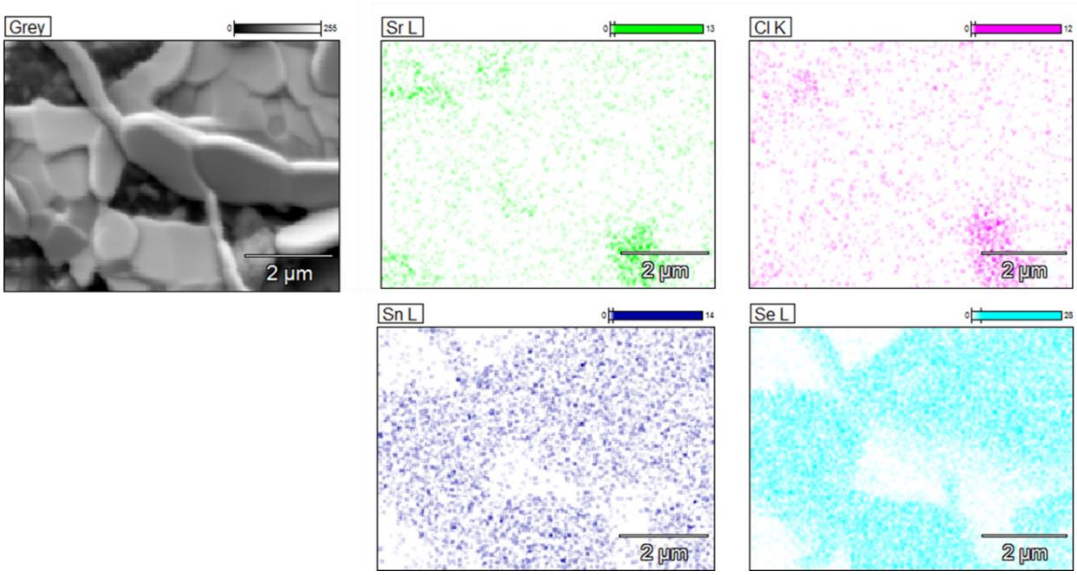

Figure 8.2: EDX imaging of non-selenized strontium chloride and tin (IV) selenide which is selenized from tin (IV) chloride precursor at 542 °C for 30 minutes. Similar accumulation patterns can be seen for Sr-Cl and Sn-Se counts.

However, the characteristic peaks of strontium selenide appear in Fig. 8.3, when the strontium acetate binary precursor is used as a strontium source. The reaction pathways of metal acetates are explained in the chapter 2.1.3.

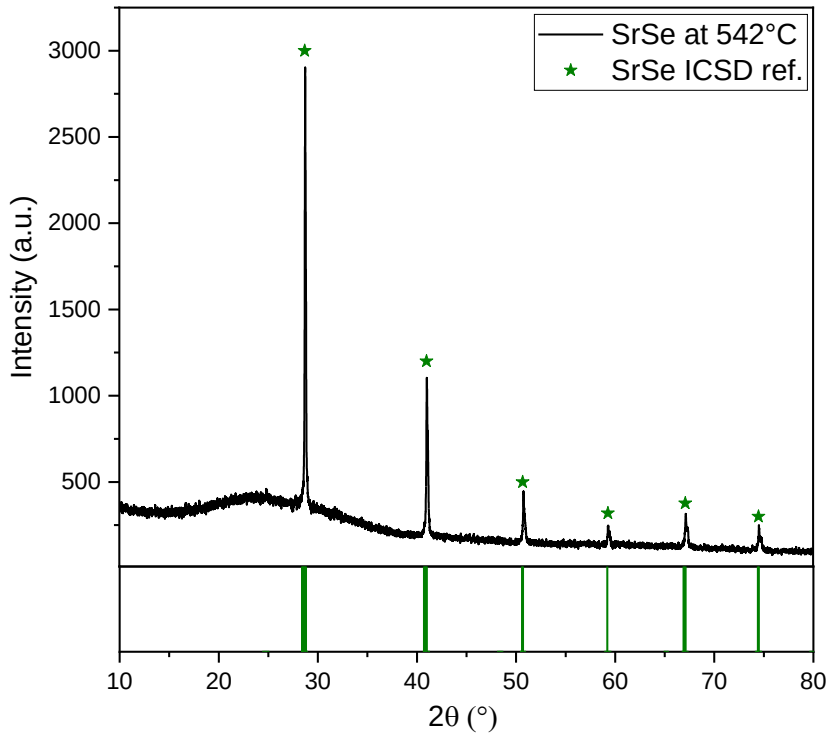

Figure 8.3: XRD pattern of the SrSe film that is selenized at 542 °C (black) for 30 minutes. ICSD database references (below) for SrSe powder (ICSD-52429, green).

After selenization is proven as possible for both compounds, mixtures of these compounds are prepared to see the potential of the perovskite formation. XRD measurements are performed to identify the material which can be seen in Fig 8.4. The produced material has similar peaks to $Sr_4Sn_2Se_{10}$. The XRD measurement of $Sr_4Sn_2Se_{10}$ reference material was performed at 200K temperature which can explain the shift in the peak positions.[78] And since $Sr_4Sn_2Se_{10}$ is not in the perovskite structure, further measurements were not done.

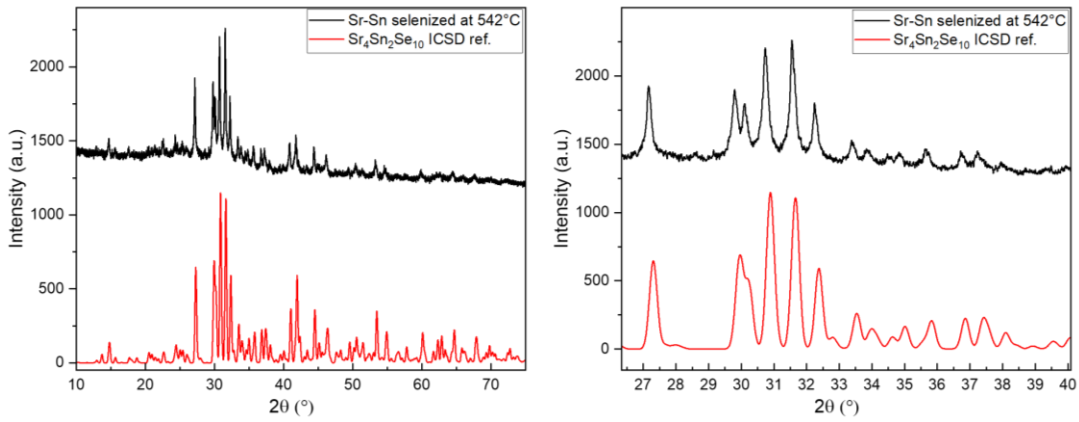

Figure 8.4: XRD pattern of the Sr-Sn precursor film that is at 542 °C (black) for 30 minutes. ICSD database reference (below) measured at 200K for $Sr_4Sn_2Se_{10}$ powder (ICSD-170233, red).

To examine the morphological structure, SEM imaging is performed for the final product. Charging effect of the material shows that it has a poor conductivity. Due to this reason, high magnification of imaging for $Sr_4Sn_2Se_{10}$ is not possible.

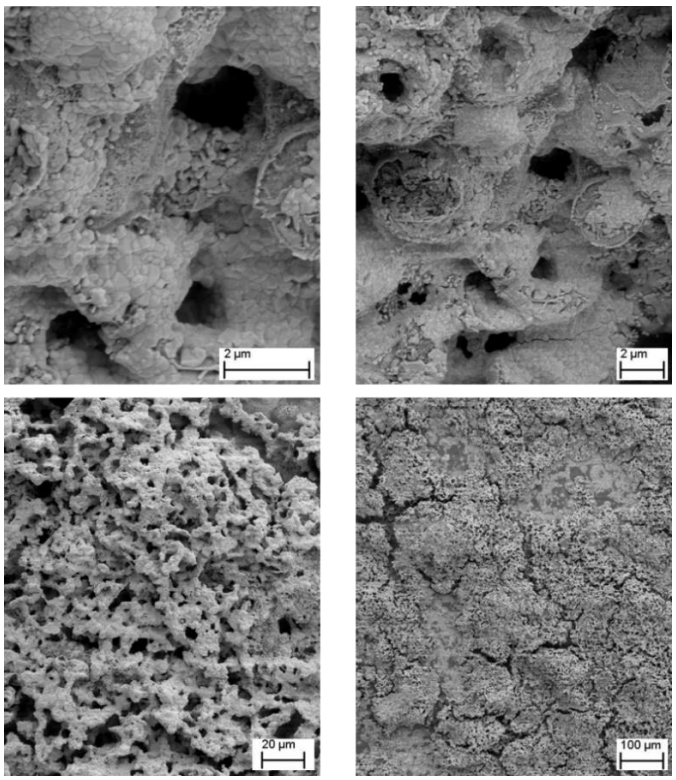

Figure 8.5: SEM image of the $Sr_4Sn_2Se_{10}$ thin film selenized at 542 °C for 30 minutes.

EDX measurement is performed to investigate the elemental composition of the produced $Sr_4Sn_2Se_{10}$ thin film. As it can be seen in Fig. 8.6, the framework of the material has selenium intensely compared to other elements. Tin concentration in the mapping is the lowest, which is proportioned to Sr:Sn:Se of 4:2:10 ratio.

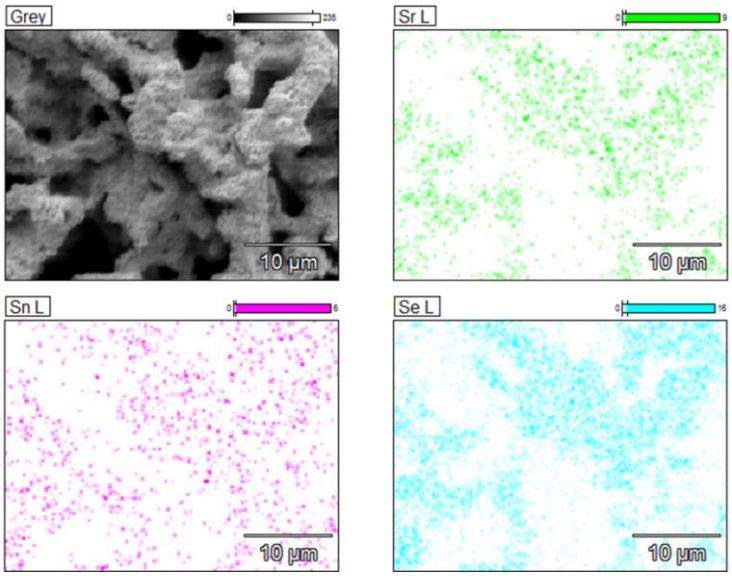

Figure 8.6: EDX imaging of $Sr_4Sn_2Se_{10}$ thin film selenized at 542 °C for 30 minutes. Homogeneous distribution of the element-counts can be seen in the images.

Another Sr-Sn mixture precursor with thiourea was measured by using the XRD instrument combined with a high temperature oven chamber. Each measurement was performed when the chamber temperature increased 50 °C. Thiourea in the film was not strong enough to sulfurize the film since the film was not sealed and open to oxygen exposure. As the reaction temperature reached 750 °C, the peaks for $SrSnO_3$ became visible. All the prominent peaks of the orthorhombic $SrSnO_3$-structure (space group *Pnma* #62) are present on the X-ray diffraction patterns which can be seen in Fig 8.7.

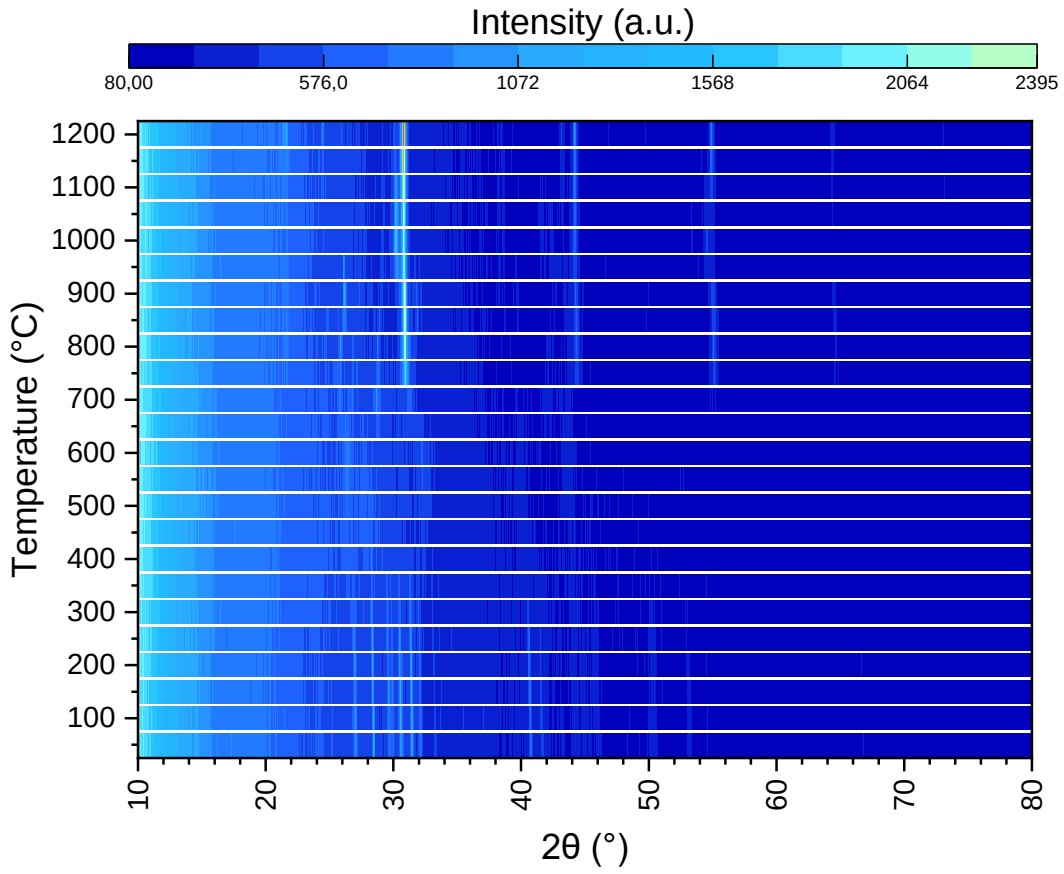

Figure 8.7: Temperature dependent annealing of the Sr-Sn-S_3 precursor film at various temperatures from room temperature up to 1200 °C with 50 °C difference for each measurement. Measurements are conducted in the Bragg-Brentano geometry. ICSD reference for $SrSnO_3$ with the distorted perovskite structure appeared above 750 °C (ICSD-13793).

Subsequent selenization trials of the $SrSnO_3$ perovskite did not fully succeed as well. The selenization process was repeated for the oxide ternary perovskite in the selenization tube furnace with 300 mg selenium chunks at 542 °C for 30 minutes. The peaks of $SrSnO_3$ decreased or slightly shifted due to partial selenium replacement as can be seen in Fig. 8.8. On

the other hand, the peaks for $Sr_4Sn_2Se_{10}$ appeared as well. The indexation is done based on ICSD reference diffractograms.

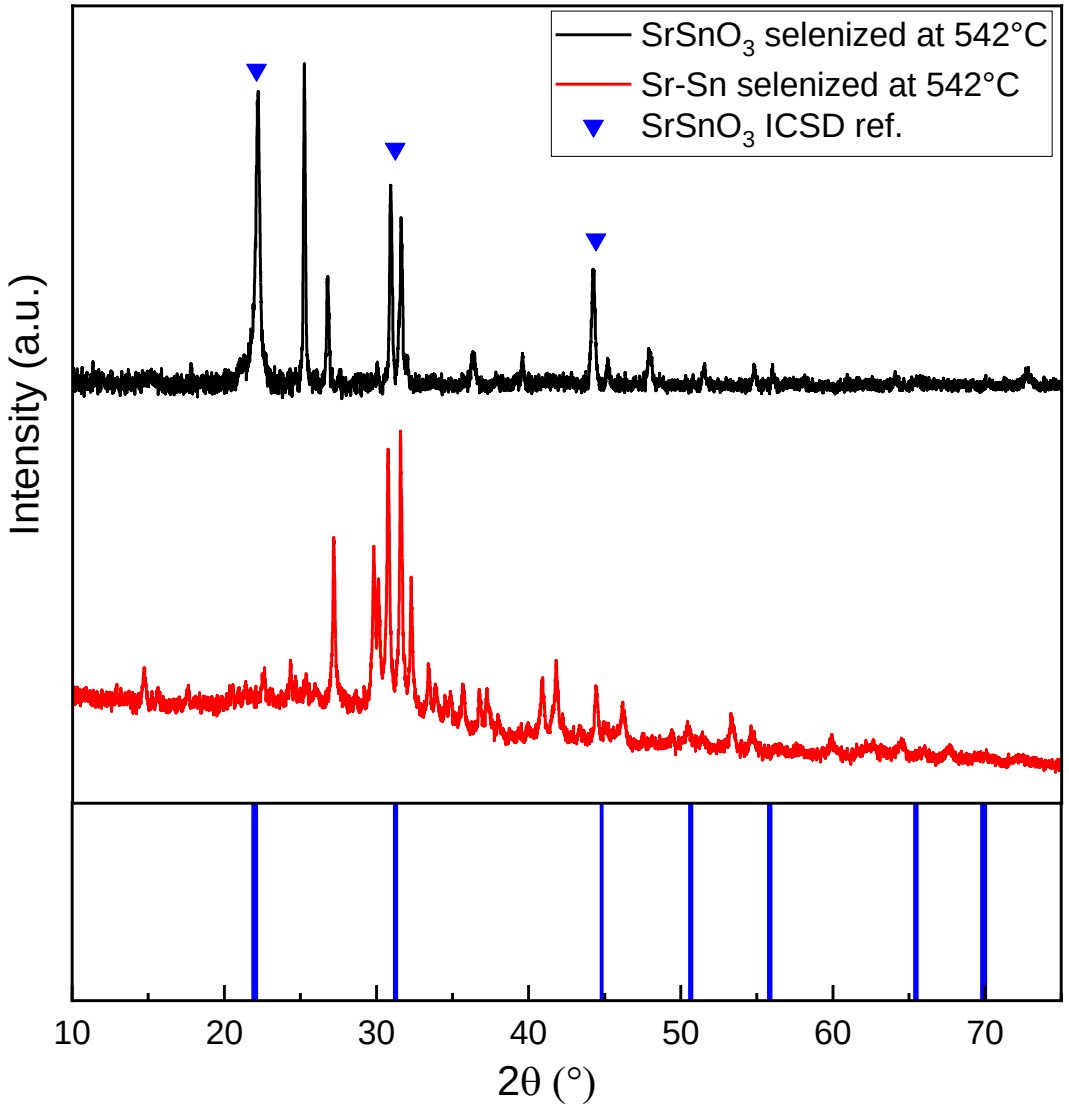

Figure 8.8: XRD results of selenized $SrSnO_3$ (black) and its comparison with the material selenized from the precursors (red), both selenizations are performed at 542 °C for 30 minutes. ICSD reference for $SrSnO_3$ with the distorted perovskite structure (ICSD-13793, blue).

X-ray diffractograms show that $SrSnO_3$ is either not selenized or partially selenized and $Sr_4Sn_2Se_{10}$ is formed at the same time. The similarity between the two samples is clear which shows the formation of $SrSnSe_3$ does not work over this reaction pathway.

8.3. Conclusions

In conclusion, the preparation of pure $SrSnSe_3$ thin films was not successful from its binary compounds at the reaction temperature of 542 °C. However, the XRD measurements show that $Sr_4Sn_2Se_{10}$ is formed in these conditions apart from the pathway of the reaction and precursors. $Sr_4Sn_2Se_{10}$ is another promising material which can be used for thermoelectric applications.[79] The XRD peaks are indexed according to the ICSD standard reference diffractograms. Since the material is not in the perovskite structure, further measurements were not performed.

$SrSnO_3$ thin film was formed from the precursor, to see if the deposition conditions of precursor were right. The ternary oxide perovskite was formed, but it was not fully selenized which might be the sign of instability of $SrSnSe_3$ as it is reported later in Sopiha *et al*.[43] Or it might be more complicated that what it is expected. However, the partial selenization of $SrSnO_3$ might be possible, since there are some unidentified peaks that are slightly shifted from the peak positions of the $SrSnO_3$ phase. Further investigations would be needed to understand its nature.

CHAPTER 9
GENERAL CONCLUSIONS

In this study, perovskites with the chemical formula of II-IV-VI_3 are investigated and their chemical and optoelectronic properties are characterized. Alkali-earth metals are picked due to their abundance in the earth's crust. From the transition metal family, early-transition metals (*e*TM: Ti, Zr, Hf) are selected due to their high and stable oxidation states which inhibit the generated electron localization. Perovskites with *e*TMs are also eligible for doping due to their non-boding d-orbitals.[40] And finally, sulfur is mainly used as the anion to reach the desired band gap energy range between 1.3-1.7 eV for the highest solar cell efficiency.

$BaZrS_3$, $BaHfS_3$, $EuZrS_3$, $EuHfS_3$ and $SrHfS_3$ thin films were deposited by a solution-processed method, which was prepared with acetate, acetylacetonate and iodide binary compounds. The catalytic property of iodide compounds is used in mixtures of other compounds in this study. The binaries were not produced in this study, instead commercially available materials were used. As a solvent, acetic acid and N-N-dimethylformamide mixture was prepared in a volumetric 1:1 ratio. The prepared ink-solutions were coated on 25x25 mm quartz substrates by spin-coating. This resulted in the study to determine the optimal deposition parameters for each material. To reach a higher thickness of the film, multiple coating cycles were done. During the static spin-coating method, solutions dissolve the previous layer and result in uneven film and/or poor coverage. To prevent that, the dynamic spin-coating method was chosen to keep the dissolution time of the already-deposited layers lower. Between spin-coating cycles, films were heated at 250 °C for 2 minutes and for 10 minutes at the end of deposition procedures to evaporate residual solvents. Spin-coating cycle numbers were determined empirically. All these deposition processes were carried out in a nitrogen filled glovebox to keep the oxygen impurity low in the final product.

At least 100 nm for post-sulfurization thickness was the aim for the thin films. To reach this thickness systematically, experiments were repeated, and each of the thicknesses was controlled by using X-ray fluorescence before and after sulfurization to record the statistics. XRF measurements also revealed the elemental composition of the films. With 100 nm thickness, reaching the elemental ratio of the perovskite structure (1:1:3), or close to it, was essential to continue conducting further measurements. For the measurements of precursor films, 5x25 mm of the samples was cut from the point of the laser-engraving. The rest of the sample could be divided into two pieces as well with the size of 20x12.5 mm. In most cases,

these almost-identical two pieces of samples were used for different sulfurization temperatures to see the effect of reaction temperature on the identical elemental composition.

After the deposition step, the samples were carried out of the glovebox in an airtight container to keep them as safe from oxidation as much as possible. There was only around one-minute oxygen exposure to the materials when taking them out of the container until sealing them in a quartz tube, where sulfurization took place. For pure earth-alkali metals, oxygen exposure for even a couple tens of seconds is too much, however, the binary compounds that were used in this study kept them relatively oxygen-free. This can be observed for the highly sulfurized $BaZrS_3$ and $BaHfS_3$ in chapters 3 and 4, respectively. Due to the stable nature of oxide perovskites, refraining from oxide phases helps to sulfurize at a lower temperature. Comparotto *et al.* suggested that capping the material with SnS is reducing the reaction temperature by keeping precursors in the non-oxide phase.[39] However, when the binaries that are used in this work are considered, it can be seen that they are picked from the easily-decomposable compounds to sulfurize and form the perovskite structure at a lower temperature subsequently. And it is seen from the XRD measurements that the perovskite crystallization is only starting after 900 °C, even though the sulfur amount of the film is already more than 50% at 800 °C. Hence, using SnS as a capping material might have a catalytic effect on the sulfurization and perovskite formation, rather than mere protection layer against oxygen.

After the evacuation of oxygen, the tube furnace was flushed with argon twice and for the third time with the reaction gas. As a sulfur source, 60 sccm flow of 5% H_2S in argon was used. Reactive H_2S gas replaced the anions of the deposited binaries with sulfur. The excess H_2S and the side products in the gas phase were evacuated from the tube through the exhaust before taking the samples out. The reaction temperatures were determined empirically for each material. And the duration of reaction was kept the same for all the materials as 30 minutes.

As the first material, $BaZrS_3$ was produced by solution deposition and consequent sulfurization. The temperature study of $BaZrS_3$ was investigated for various reaction temperatures to determine the optimum one. At 1100 °C, the $Ba_4Zr_3S_{10}$ phase of 2D-chalcogenide perovskite was formed, which is a member of the Ruddlesden-Popper phases.[65–68] Solution-processed material was compared with the PLD deposited material of Márquez *et al* which has the oxide phase as impurity, whereas the solution-processed does not have it.[36] These results showed that these two materials are comparable and the solution-processed thin film does not have any drawbacks. Due to the poor quality of the samples, photoluminescence could not be measured with our available setup. This suggests dominant non-radiative recombination due to defects. As a result, this is currently not a good candidate for PV applications. However, if it is possible to reduce the amounts of defects as well as the processing temperature, this material might exhibit the desired properties after all. The effect of titanium alloying is also investigated. Titanium alloyed material stayed in the distorted

perovskite structure whereas $BaTiS_3$ is in the needle-like non-perovskite configuration. Moreover, titanium addition decreased the band gap as expected.

$BaHfS_3$ is another material that was investigated for PV applications. Due to its low carrier lifetime, it might not be a promising solar cell absorber without further developments. However, it might be promising material for LEDs. With the band gap engineering, the band gap can be adjusted for the orange-yellow emission range by using oxygen to increase the band gap and selenium to decrease.

Europium is a special part of this work since the divalent ions of Eu^{2+} have ionic radii close to earth-alkali metals. Due to this property, chalcogenide perovskites of europium show similar structural and physical properties to earth-alkali perovskites. Moreover, both divalent and trivalent europium ions have strong photoluminescence.[41] $EuZrS_3$ was produced in the distorted perovskite (β-phase) structure with sulfur deficiency. A longer reaction duration than 30 minutes could help to increase the sulfur amount. Nevertheless, there was no XRD-peak for binaries, which means this deficiency is in the perovskite crystal structure. On the other hand, EuS peaks were observed on the europium-rich films. This material needs a higher reaction temperature of 1100 °C for a higher degree of sulfurization, whereas $BaZrS_3$ needs only 1000 °C. The trial of titanium alloying of 3% resulted in the needle-like non-perovskite (α-phase) configuration, which means the distorted perovskite structure is only metastable, as it is reported that the α-phase is more stable at low temperature.

Approaches for the $EuHfS_3$ production were successful as well. The material was produced in the distorted perovskite structure, whose properties are still not fully unveiled. Unfortunately, due to the earlier-oxidized Hf source in this study, some of its properties are still unclear. The XRD pattern showed that $EuHfS_3$ with HfO_2 impurity was obtained. To reach better crystallinity, $EuHfS_3$ needs a high reaction temperature of 1100 °C, just like $EuZrS_3$. Raman spectra showed a similar pattern with $EuZrS_3$ due to the similar crystal structure. And the photoconductivity transient measurement showed that $EuHfS_3$ might be promising for PV applications if the carrier lifetime can be prolonged by doping or alloying etc.

$SrHfS_3$ was the last material that was researched in this work. The production was conducted simultaneously with $EuHfS_3$, thus a similar HfO_2 impurity is present in this film as well. However, the XRD peaks of $SrHfS_3$ were strong enough to identify the material. The color was green as it is reported in the literature, which was the main reason for the usage proposals for the green LED studies. Raman spectra showed that $SrHfS_3$ has a similar structure to $EuHfS_3$ rather than $BaHfS_3$. Due to this reason, europium was alloyed with strontium in various amounts as a side study, which increased the coverage on the substrate. Up to 20% of europium was alloyed to $SrHfS_3$, and yet there was not any sign of phase separation.

All the measurements were conducted at room temperature. Some of the measurements were not successful or even conducted due to poor coverage of the samples or charging that stemmed from low conductivities as well as impurities.

Recently, Sopiha *et al*. reported the materials that can be produced based on the calculations of the Goldsmith tolerance factor and the octahedral factor.[43] From these materials, $BaZrS_3$, $BaHfS_3$ and $SrHfS_3$ were synthesized successfully which are on the edge of the perovskite region. If the similarity between the ionic radii of Eu^{2+} and Sr is considered, the place of europium chalcogenide perovskites can be found around the corresponding Sr perovskites which makes this study experimentally reliable.

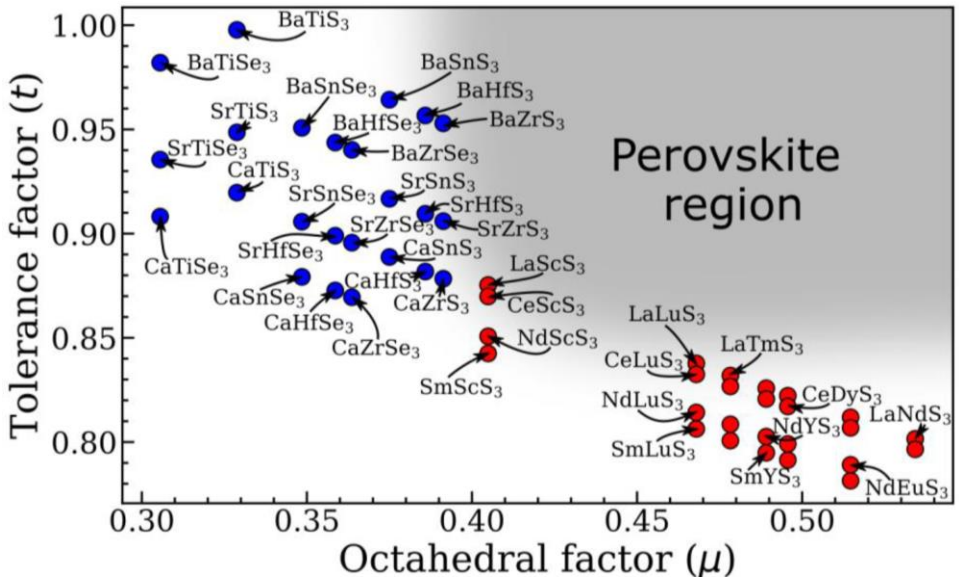

Figure 9.1: Octahedral factor and Goldschmidt tolerance factor of Chalcogenide perovskites. The perovskite formations are expected in the shaded region (reprinted with permission: Sopiha *et al*., 'Chalcogenide Perovskites: Tantalizing Prospects, Challenging Materials', *Adv. Optical Mater.* 2021, 2101704).

In this work, various sulfide perovskites with transition metals were studied in the distorted perovskite structure. From time to time, the effect of slight variations in the structure of the material were investigated as well. Another effort was performing the production as thin films, rather than powders, since they are practical for industrial applications. The ink-based deposition method was developed to realize that purpose and it was observed that the ink-recipe can be applied to unconventional materials not only to earth-alkali metals but also to one member of the lanthanides. With the help of the developed molecular ink recipe, oxidation of the precursors to form the perovskite structure before sulfurization is not necessary anymore.

CHAPTER 10
OUTLOOK AND FUTURE WORKS

This study of chalcogenide perovskites with transition metals has opened vast fields of insight into the material and optoelectronic properties of novel materials by designing, synthesizing, and analyzing the data. Chalcogenide perovskites are still developing, and they have immense potential. The focus of the future work should be placed on improving the quality and integrating these materials into the practical works (e.g., solar cells, water-splitting cathodes, batteries, or LEDs.)

In this work, mainly sulfide materials were studied. However, selenides have significant importance in the semiconductor field as well. Selenide perovskites still need to be investigated. So far, the selenide materials in ABX_3 chemical structures were either non-perovskite or contain uranium or thorium which makes their applications unpractical.[43,80–82] However, it is worth looking into selenide materials that were not investigated yet.

Due to the hafnium oxidation, hafnium chalcogenide perovskites that were produced in this study should be researched once more and processed from an unoxidized batch of the hafnium binary to unveil their properties fully. The proposed method in this study worked with $BaHfS_3$, but not with $EuHfS_3$ and $SrHfS_3$ which were produced with another batch of hafnium acetylacetonate from the same brand.

Another promising field for distorted chalcogenide perovskites is using them as LEDs. Their short carrier lifetime and the blue shift on the PL make them favorable for their light emissions. Current commercially available semiconductors (GaN, InGaN, etc.) have a severe problem due to the drop in the quantum efficiency in the wavelength range around the green region (E_g = 2.18-2.50 eV), which is called the "green gap problem". $SrHfS_3$ might be a promising material to remove this deficiency with its experimental band gap of 2.3 eV.[40,75,76]

Doping is another aspect to change the semiconductor material type. Due to the sulfur deficiency in chalcogenide perovskites, they tend to form n-type material which needs material-specific solar cell architecture than the commonly used one. For $SrHfS_3$ doping, Hanzawa *et al.* used SrP and La_2S_3 for doping to p-type and n-type respectively.[40] Similar compounds can be used for other chalcogenide perovskites as well to improve their efficiency.

Even though fully selenized precursors form the non-perovskite structures, it is possible to selenize the sulfurized distorted perovskites partially, to decrease band gaps by applying band

gap engineering. Nishigaki *et al*. produced $BaZr(S_{0.6}Se_{0.4})_3$ in the distorted perovskite structure with 0.18 eV lesser band gap than the pure $BaZrS_3$.[33] Alloying of cations is a good example for band gap engineering as well. By alloying titanium to *e*TMs, the band gap can be decreased as well, which increases the power conversion efficiency.[33,37,69,83]

To make these materials cost-effective, low-temperature production is necessary. Productions at high reaction temperature are not only costly but also makes the scaling up of processes more difficult. Additionally, these high temperatures pose a problem for usage in tandem photovoltaic cells, as many layers currently used for the bottom cell cannot withstand them. Investigation of novel catalysts could help to decrease the reaction temperature by increasing the reaction rate. One different aspect is using ionic solvents combined with microwave heating, which can reach remarkably high temperatures locally. Laser ablation might solve the problem as well since the material is deposited as thin films. Another aspect is producing high amounts of powder at high temperatures by using the ink-based method, and making targets from the powder for low-temperature deposition methods (e.g. sputtering, PLD).[38,84]

REFERENCES

(1) Ashton, T. S.; others. The Industrial Revolution 1760-1830. *OUP Catalogue* **1997**.

(2) Kardashev, N. S. Transmission of Information by Extraterrestrial Civilizations. *sovast* **1964**, *8*, 217.

(3) Sagan, C. *Carl Sagan's Cosmic Connection: An Extraterrestrial Perspective*; Cambridge University Press: Cambridge ; New York, 2000.

(4) Christiansen, J. Global Market Outlook for Solar Power. **2022**, 116.

(5) Rhodes, C. J. The 2015 Paris Climate Change Conference: Cop21. *Science Progress* **2016**, *99* (1), 97–104. https://doi.org/10.3184/003685016X14528569315192.

(6) IPCC; Masson-Delmotte, V.; Zhai, P.; Pörtner, H.-O.; Roberts, D.; Skea, J.; Shukla, P.; Pirani, A.; Moufouma-Okia, W.; Péan, C.; Pidcock, R.; Connors, S.; Matthews, R.; Chen, Y.; Zhou, X.; Gomis, M.; Lonnoy, E.; Maycock, T.; Tignor, M.; Tabatabaei, M. *Global Warming of 1.5°C. An IPCC Special Report on the Impacts of Global Warming of 1.5°C above Pre-Industrial Levels and Related Global Greenhouse Gas Emission Pathways, in the Context of Strengthening the Global Response to the Threat of Climate Change, Sustainable Development, and Efforts to Eradicate Poverty*; 2018.

(7) Goldschmidt, J. C.; Wagner, L.; Pietzcker, R.; Friedrich, L. Technological Learning for Resource Efficient Terawatt Scale Photovoltaics. *Energy Environ. Sci.* **2021**, *14* (10), 5147–5160. https://doi.org/10.1039/D1EE02497C.

(8) Glass Is the Hidden Gem in a Carbon-Neutral Future. *Nature* **2021**, *599* (7883), 7–8. https://doi.org/10.1038/d41586-021-02992-8.

(9) *National Renewable Energy Laboratories, Efficiency Chart*. https://www.nrel.gov/pv/cell-efficiency.html.

(10) Rose, G. Beschreibung einiger neuen Mineralien des Urals. *Ann. Phys. Chem.* **1839**, *124* (12), 551–573. https://doi.org/10.1002/andp.18391241205.

(11) High Efficiency Plants and Building Integrated Renewable Energy Systems. In *Handbook of Energy Efficiency in Buildings*; Elsevier, 2019; pp 441–595. https://doi.org/10.1016/B978-0-12-812817-6.00040-1.

(12) Lincot, D. The New Paradigm of Photovoltaics: From Powering Satellites to Powering Humanity. *Comptes Rendus Physique* **2017**, *18* (7–8), 381–390. https://doi.org/10.1016/j.crhy.2017.09.003.

(13) Kojima, A.; Teshima, K.; Shirai, Y.; Miyasaka, T. Organometal Halide Perovskites as Visible-Light Sensitizers for Photovoltaic Cells. *J. Am. Chem. Soc.* **2009**, *131* (17), 6050–6051. https://doi.org/10.1021/ja809598r.

(14) Beard, M. C.; Luther, J. M.; Nozik, A. J. The Promise and Challenge of Nanostructured Solar Cells. *Nature Nanotech* **2014**, *9* (12), 951–954. https://doi.org/10.1038/nnano.2014.292.

(15) Goldschmidt, V. M. Die Gesetze der Krystallochemie. *Naturwissenschaften* **1926**, *14* (21), 477–485. https://doi.org/10.1007/BF01507527.

(16) Bartel, C. J.; Sutton, C.; Goldsmith, B. R.; Ouyang, R.; Musgrave, C. B.; Ghiringhelli, L. M.; Scheffler, M. New Tolerance Factor to Predict the Stability of Perovskite Oxides and Halides. *Sci. Adv.* **2019**, *5* (2), eaav0693. https://doi.org/10.1126/sciadv.aav0693.

(17) Filip, M. R.; Giustino, F. The Geometric Blueprint of Perovskites. *Proc. Natl. Acad. Sci. U.S.A.* **2018**, *115* (21), 5397–5402. https://doi.org/10.1073/pnas.1719179115.

(18) Pilania, G.; Ghosh, A.; Hartman, S. T.; Mishra, R.; Stanek, C. R.; Uberuaga, B. P. Anion Order in Oxysulfide Perovskites: Origins and Implications. *npj Comput Mater* **2020**, *6* (1), 71. https://doi.org/10.1038/s41524-020-0338-1.

(19) Min, H.; Lee, D. Y.; Kim, J.; Kim, G.; Lee, K. S.; Kim, J.; Paik, M. J.; Kim, Y. K.; Kim, K. S.; Kim, M. G.; Shin, T. J.; Il Seok, S. Perovskite Solar Cells with Atomically Coherent Interlayers on SnO2 Electrodes. *Nature* **2021**, *598* (7881), 444–450. https://doi.org/10.1038/s41586-021-03964-8.

(20) Pareek, D.; Taskesen, T.; Márquez, J. A.; Stange, H.; Levcenco, S.; Simsek, I.; Nowak, D.; Pfeiffelmann, T.; Chen, W.; Stroth, C.; Sayed, M. H.; Mikolajczak, U.; Parisi, J.; Unold, T.; Mainz, R.; Gütay, L. Reaction Pathway for Efficient $Cu_2ZnSnSe_4$ Solar Cells from Alloyed Cu-Sn Precursor via a Cu-Rich Selenization Stage. *Sol. RRL* **2020**, *4* (6), 2000124. https://doi.org/10.1002/solr.202000124.

(21) Yetkin, H. A.; Kodalle, T.; Bertram, T.; Tovar, A. V.; Klenk, R.; Rusu, M.; Ibaceta-Jana, J.; Ruske, F.; Simsek, I.; Muydinov, R.; Szyszka, B.; Schlatmann, R.; A. Kaufmann, C. Elucidating the Effect of the Different Buffer Layers on the Thermal Stability of CIGSe Solar Cells. *IEEE J. Photovoltaics* **2021**, 1–10. https://doi.org/10.1109/JPHOTOV.2021.3053483.

(22) Comparotto, C.; Davydova, A.; Ericson, T.; Riekehr, L.; Moro, M. V.; Kubart, T.; Scragg, J. Chalcogenide Perovskite BaZrS3 : Thin Film Growth by Sputtering and Rapid Thermal Processing. *ACS Appl. Energy Mater.* **2020**, *3* (3), 2762–2770. https://doi.org/10.1021/acsaem.9b02428.

(23) Sun, Y.-Y.; Agiorgousis, M. L.; Zhang, P.; Zhang, S. Chalcogenide Perovskites for Photovoltaics. *Nano Lett.* **2015**, *15* (1), 581–585. https://doi.org/10.1021/nl504046x.

(24) Ju, M.-G.; Dai, J.; Ma, L.; Zeng, X. C. Perovskite Chalcogenides with Optimal Bandgap and Desired Optical Absorption for Photovoltaic Devices. *Adv. Energy Mater.* **2017**, *7* (18), 1700216. https://doi.org/10.1002/aenm.201700216.

(25) Huo, Z.; Wei, S.-H.; Yin, W.-J. High-Throughput Screening of Chalcogenide Single Perovskites by First-Principles Calculations for Photovoltaics. *J. Phys. D: Appl. Phys.* **2018**, *51* (47), 474003. https://doi.org/10.1088/1361-6463/aae1ee.

(26) Hahn, H.; Mutschke, U. Untersuchungen über ternäre Chalkogenide. XI. Versuche zur Darstellung von Thioperowskiten. *Z. Anorg. Allg. Chem.* **1957**, *288* (5–6), 269–278. https://doi.org/10.1002/zaac.19572880505.

(27) Clearfield, A. The Synthesis and Crystal Structures of Some Alkaline Earth Titanium and Zirconium Sulfides. *Acta Cryst* **1963**, *16* (2), 135–142. https://doi.org/10.1107/S0365110X6300030X.

(28) Lelieveld, R.; IJdo, D. J. W. Sulphides with the GdFeO3 Structure. *Acta Crystallogr B Struct Sci* **1980**, *36* (10), 2223–2226. https://doi.org/10.1107/S056774088000845X.

(29) Bennett, J. W.; Grinberg, I.; Rappe, A. M. Effect of Substituting of S for O: The Sulfide Perovskite BaZrS3 Investigated with Density Functional Theory. *Phys. Rev. B* **2009**, *79* (23), 235115. https://doi.org/10.1103/PhysRevB.79.235115.

(30) Perera, S.; Hui, H.; Zhao, C.; Xue, H.; Sun, F.; Deng, C.; Gross, N.; Milleville, C.; Xu, X.; Watson, D. F.; Weinstein, B.; Sun, Y.-Y.; Zhang, S.; Zeng, H. Chalcogenide Perovskites – an Emerging Class of Ionic Semiconductors. *Nano Energy* **2016**, *22*, 129–135. https://doi.org/10.1016/j.nanoen.2016.02.020.

(31) Niu, S.; Huyan, H.; Liu, Y.; Yeung, M.; Ye, K.; Blankemeier, L.; Orvis, T.; Sarkar, D.; Singh, D. J.; Kapadia, R.; Ravichandran, J. Bandgap Control via Structural and Chemical Tuning of Transition Metal Perovskite Chalcogenides. *Adv. Mater.* **2017**, *29* (9), 1604733. https://doi.org/10.1002/adma.201604733.

(32) Filippone, S. A.; Sun, Y.-Y.; Jaramillo, R. Determination of Adsorption-Controlled Growth Windows of Chalcogenide Perovskites. *MRC* **2018**, *8* (01), 145–151. https://doi.org/10.1557/mrc.2018.10.

(33) Nishigaki, Y.; Nagai, T.; Nishiwaki, M.; Aizawa, T.; Kozawa, M.; Hanzawa, K.; Kato, Y.; Sai, H.; Hiramatsu, H.; Hosono, H.; Fujiwara, H. Extraordinary Strong Band-Edge Absorption in Distorted Chalcogenide Perovskites. *Sol. RRL* **2020**, *4* (5), 1900555. https://doi.org/10.1002/solr.201900555.

(34) Gupta, T.; Ghoshal, D.; Yoshimura, A.; Basu, S.; Chow, P. K.; Lakhnot, A. S.; Pandey, J.; Warrender, J. M.; Efstathiadis, H.; Soni, A.; Osei-Agyemang, E.; Balasubramanian, G.; Zhang, S.; Shi, S.; Lu, T.; Meunier, V.; Koratkar, N. An Environmentally Stable and Lead-Free Chalcogenide Perovskite. *Adv. Funct. Mater.* **2020**, 2001387. https://doi.org/10.1002/adfm.202001387.

(35) Wei, X.; Hui, H.; Zhao, C.; Deng, C.; Han, M.; Yu, Z.; Sheng, A.; Roy, P.; Chen, A.; Lin, J.; Watson, D. F.; Sun, Y.-Y.; Thomay, T.; Yang, S.; Jia, Q.; Zhang, S.; Zeng, H. Realization of BaZrS3 Chalcogenide Perovskite Thin Films for Optoelectronics. *Nano Energy* **2020**, *68*, 104317. https://doi.org/10.1016/j.nanoen.2019.104317.

(36) Márquez, J. A.; Rusu, M.; Hempel, H.; Ahmet, I. Y.; Kölbach, M.; Simsek, I.; Choubrac, L.; Gurieva, G.; Gunder, R.; Schorr, S.; Unold, T. BaZrS3 Chalcogenide Perovskite Thin Films by H2S Sulfurization of Oxide Precursors. *J. Phys. Chem. Lett.* **2021**, 2148–2153. https://doi.org/10.1021/acs.jpclett.1c00177.

(37) Sharma, S.; Ward, Z.; Bhimani, K.; Li, K.; Lakhnot, A.; Jain, R.; Shi, S.-F.; Terrones, H.; Koratkar, N. Bandgap Tuning in $BaZrS_3$ Perovskite Thin Films. *ACS Appl. Electron. Mater.* **2021**, acsaelm.1c00575. https://doi.org/10.1021/acsaelm.1c00575.

(38) Yu, Z.; Wei, X.; Zheng, Y.; Hui, H.; Bian, M.; Seo, J.-H.; Sun, Y.-Y.; Jia, Q.; Zhang, S.; Yang, S. Chalcogenide Perovskite BaZrS3 Thin-Film Electronic and Optoelectronic Devices by Low Temperature Processing. **2021**, 27. https://doi.org/doi.org/10.1016/j.nanoen.2021.105959.

(39) Comparotto, C.; Ström, P.; Donzel-Gargand, O.; Kubart, T.; Scragg, J. J. S. Synthesis of $BaZrS_3$ Perovskite Thin Films at a Moderate Temperature on Conductive Substrates. *ACS Appl. Energy Mater.* **2022**, acsaem.2c00704. https://doi.org/10.1021/acsaem.2c00704.

(40) Hanzawa, K.; Iimura, S.; Hiramatsu, H.; Hosono, H. Material Design of Green-Light-Emitting Semiconductors: Perovskite-Type Sulfide SrHfS3. *J. Am. Chem. Soc.* **2019**, *141* (13), 5343–5349. https://doi.org/10.1021/jacs.8b13622.

(41) Guo, S.-P.; Chi, Y.; Zou, J.-P.; Xue, H.-G. Crystal and Electronic Structures, and Photoluminescence and Photocatalytic Properties of α-$EuZrS_3$. *New J. Chem.* **2016**, *40* (12), 10219–10226. https://doi.org/10.1039/C6NJ02106A.

(42) Moroz, N. A. Engineered Transition Metal Chalcogenides for Photovoltaic, Thermoelectric, and Magnetic Applications, University of Michigan, 2017.

(43) Sopiha, K. V.; Comparotto, C.; Márquez, J. A.; Scragg, J. J. S. Chalcogenide Perovskites: Tantalizing Prospects, Challenging Materials. *Adv. Optical Mater.* **2021**, 2101704. https://doi.org/10.1002/adom.202101704.

(44) Van Der Sluys, W. G. The Solubility Rules: Why Are All Acetates Soluble? *J. Chem. Educ.* **2001**, *78* (1), 111. https://doi.org/10.1021/ed078p111.

(45) Sarfraz, J.; Määttänen, A.; Ihalainen, P.; Keppeler, M.; Lindén, M.; Peltonen, J. Printed Copper Acetate Based H2S Sensor on Paper Substrate. *Sensors and Actuators B: Chemical* **2012**, *173*, 868–873. https://doi.org/10.1016/j.snb.2012.08.008.

(46) Wang, Y.; Sato, N.; Yamada, K.; Fujino, T. Synthesis of BaZrS3 in the Presence of Excess Sulfur. *Journal of Alloys and Compounds* **2000**, *311* (2), 214–223. https://doi.org/10.1016/S0925-8388(00)01134-8.

(47) Wang, Y.; Sato, N.; Fujino, T. Synthesis of BaZrS3 by Short Time Reaction at Lower Temperatures. *Journal of Alloys and Compounds* **2001**, *327* (1–2), 104–112. https://doi.org/10.1016/S0925-8388(01)01553-5.

(48) Davidson, A. W. SOLUTIONS OF SALTS IN PURE ACETIC ACID. I. PRELIMINARY PAPER [1]. *J. Am. Chem. Soc.* **1928**, *50* (7), 1890–1895. https://doi.org/10.1021/ja01394a009.

(49) Hwang, U.-Y.; Park, H.-S.; Koo, K.-K. Behavior of Barium Acetate and Titanium Isopropoxide during the Formation of Crystalline Barium Titanate. *Ind. Eng. Chem. Res.* **2004**, *43* (3), 728–734. https://doi.org/10.1021/ie030276q.

(50) Chang, Q.; Zhang, N.; Liu, W.; Ye, Q.; Yu, Y.; Chen, X.; Li, C. Thermal Properties and Gas Decomposition Products of Hafnium(IV) Acetylacetonate. *Asian J. Chem.* **2010**, *22* (3), 4.

(51) Ki, W.; Hillhouse, H. W. Earth-Abundant Element Photovoltaics Directly from Soluble Precursors with High Yield Using a Non-Toxic Solvent. *Adv. Energy Mater.* **2011**, *1* (5), 732–735. https://doi.org/10.1002/aenm.201100140.

(52) Bucaro, J. A.; Dardy, H. D. High-temperature Brillouin Scattering in Fused Quartz. *Journal of Applied Physics* **1974**, *45* (12), 5324–5329. https://doi.org/10.1063/1.1663238.

(53) Lakshmikumar, S. T.; Rastogi, A. C. Selenization of Cu and In Thin Films for the Preparation of Selenide Photo-Absorber Layers in Solar Cells Using Se Vapour Source. *Solar Energy Materials and Solar Cells* **1994**, *32* (1), 7–19. https://doi.org/10.1016/0927-0248(94)90251-8.

(54) Bucherl, C. N.; Oleson, K. R.; Hillhouse, H. W. Thin Film Solar Cells from Sintered Nanocrystals. *Current Opinion in Chemical Engineering* **2013**, *2* (2), 168–177. https://doi.org/10.1016/j.coche.2013.03.004.

(55) Hodul, D. T.; Sienko, M. J. Hf(SexTe1-x)2: Deviation from Vegard's Law in Mixed Systems. *Inorg. Chem.* **1981**, *20* (11), 3655–3659. https://doi.org/10.1021/ic50225a014.

(56) Thornton, S. T.; Rex, A. F. *Modern Physics for Scientists and Engineers*, 4th ed.; Cengage Learning: Boston, MA, 2013.

(57) Le Bail, A. Whole Powder Pattern Decomposition Methods and Applications: A Retrospection. *Powder Diffr.* **2005**, *20* (4), 316–326. https://doi.org/10.1154/1.2135315.

(58) Inkson, B. J. Scanning Electron Microscopy (SEM) and Transmission Electron Microscopy (TEM) for Materials Characterization. In *Materials Characterization Using Nondestructive Evaluation (NDE) Methods*; Elsevier, 2016; pp 17–43. https://doi.org/10.1016/B978-0-08-100040-3.00002-X.

(59) Álvarez-García, J.; Izquierdo-Roca, V.; Pistor, P.; Schmid, T.; Pérez-Rodríguez, A. Raman Spectroscopy on Thin Films for Solar Cells. In *Advanced Characterization Techniques for Thin Film Solar Cells*; Abou-Ras, D., Kirchartz, T., Rau, U., Eds.; Wiley-VCH Verlag GmbH & Co. KGaA: Weinheim, Germany, 2016; pp 469–499. https://doi.org/10.1002/9783527699025.ch17.

(60) Cesaria, M.; Caricato, A. P.; Martino, M. Realistic Absorption Coefficient of Ultrathin Films. *J. Opt.* **2012**, *14* (10), 105701. https://doi.org/10.1088/2040-8978/14/10/105701.

(61) Zanatta, A. R. Revisiting the Optical Bandgap of Semiconductors and the Proposal of a Unified Methodology to Its Determination. *Sci Rep* **2019**, *9* (1), 11225. https://doi.org/10.1038/s41598-019-47670-y.

(62) Rusu, M.; Kodalle, T.; Choubrac, L.; Barreau, N.; Kaufmann, C. A.; Schlatmann, R.; Unold, T. Electronic Structure of the CdS/Cu(In,Ga)Se $_2$ Interface of KF- and RbF-

Treated Samples by Kelvin Probe and Photoelectron Yield Spectroscopy. *ACS Appl. Mater. Interfaces* **2021**, *13* (6), 7745–7755. https://doi.org/10.1021/acsami.0c20976.

(63) Dhaliwal, A. K.; Hay, J. N. The Characterization of Polyvinyl Butyral by Thermal Analysis. *Thermochimica Acta* **2002**, *391* (1–2), 245–255. https://doi.org/10.1016/S0040-6031(02)00187-9.

(64) Wang, J. Low Energy Electron Diffraction Studies of Transition Metal Oxide Surfaces and Films. PhD Thesis, Universitäts-und Landesbibliothek, 2005.

(65) Niu, S.; Zhao, B.; Ye, K.; Bianco, E.; Zhou, J.; McConney, M. E.; Settens, C.; Haiges, R.; Jaramillo, R.; Ravichandran, J. Crystal Growth and Structural Analysis of Perovskite Chalcogenide BaZrS3 and Ruddlesden-Popper Phase Ba3Z2S7. *J. Mater. Res.* **2019**, *34* (22), 3819–3826. https://doi.org/10.1557/jmr.2019.348.

(66) Niu, S. Perovskite Chalcogenides: Emerging Semiconductors for Visible to Infrared, UNIVERSITY OF SOUTHERN CALIFORNIA, 2019.

(67) Niu, S.; Sarkar, D.; Williams, K.; Zhou, Y.; Li, Y.; Bianco, E.; Huyan, H.; Cronin, S. B.; McConney, M. E.; Haiges, R.; Jaramillo, R.; Singh, D. J.; Tisdale, W. A.; Kapadia, R.; Ravichandran, J. Optimal Bandgap in a 2D Ruddlesden–Popper Perovskite Chalcogenide for Single-Junction Solar Cells. *Chem. Mater.* **2018**, *30* (15), 4882–4886. https://doi.org/10.1021/acs.chemmater.8b01707.

(68) Li, W.; Niu, S.; Zhao, B.; Haiges, R.; Zhang, Z.; Ravichandran, J.; Janotti, A. Band Gap Evolution in Ruddlesden-Popper Phases. *Phys. Rev. Materials* **2019**, *3* (10), 101601. https://doi.org/10.1103/PhysRevMaterials.3.101601.

(69) Wei, X.; Hui, H.; Perera, S.; Sheng, A.; Watson, D. F.; Sun, Y.-Y.; Jia, Q.; Zhang, S.; Zeng, H. Ti-Alloying of BaZrS3 Chalcogenide Perovskite for Photovoltaics. *arXiv:2004.04261 [cond-mat]* **2020**.

(70) Basera, P.; Bhattacharya, S. Chalcogenide Perovskites: An Emerging Class of Semiconductors for Optoelectronics. 34.

(71) Filippone, S. A.; Sun, Y.-Y.; Jaramillo, R. The Effect of an Improved Density Functional on the Thermodynamics and Adsorption-Controlled Growth Windows of Chalcogenide Perovskites. *MRS Advances* **2018**, *3* (55), 3249–3254. https://doi.org/10.1557/adv.2018.497.

(72) Hulliger, F.; Siegrist, T. The Crystal Structures of $BaSe_2$ and $BaSe_3$. *Zeitschrift für Naturforschung B* **1981**, *36* (1), 14–15. https://doi.org/10.1515/znb-1981-0104.

(73) Rimmington, H. P. B.; Balchin, A. A. Crystal Data for Layer Compounds in the Series HfSxSe2?X. *J Mater Sci* **1974**, *9* (2), 343–345. https://doi.org/10.1007/BF00550964.

(74) Greenaway, D. L.; Nitsche, R. PREPARATION AND OPTICAL PROPERTIES OF GROUP IV-VIZ CHALCOGENIDES HAVING THE Cd12 STRUCTURE. 14.

(75) Usman, M.; Munsif, M.; Mushtaq, U.; Anwar, A.-R.; Muhammad, N. Green Gap in GaN-Based Light-Emitting Diodes: In Perspective. *Critical Reviews in Solid State and Materials Sciences* **2021**, *46* (5), 450–467. https://doi.org/10.1080/10408436.2020.1819199.

(76) Schiavon, D. Analysis of the Green Gap Problem in III-Nitride LEDs, Universität Ulm, 2015. https://doi.org/10.18725/OPARU-3224.

(77) Veluchamy, P. Growth and Characterisation of New Semi Organic Crystal Bisthiourea Calciumacetate. *IOSR JAP* **2017**, *09* (02), 69–75. https://doi.org/10.9790/4861-0902016975.

(78) Pocha, R.; Johrendt, D. Crystal Structures of $Sr_4Sn_2Se_9$ and $Sr_4Sn_2Se_{10}$ and the Oxidation State of Tin in an Unusual Geometry. *Inorg. Chem.* **2004**, *43* (21), 6830–6837. https://doi.org/10.1021/ic049663y.

(79) Assoud, A.; Soheilnia, N.; Kleinke, H. Band Gap Tuning in New Strontium Seleno-Stannates. *Chem. Mater.* **2004**, *16* (11), 2215–2221. https://doi.org/10.1021/cm0499242.

(80) Daoudi, A.; Noel, H. Synthese, structure cristalline et proprietes magnetiques du seleniure ternaire d'uranium et de palladium: PdUSe3. *Journal of the Less Common Metals* **1989**, *153* (2), 293–298. https://doi.org/10.1016/0022-5088(89)90124-0.

(81) Mar, A.; Ibers, J. A. Structure of Europium Zirconium Selenide, EuZrSe3. *Acta Crystallogr C Cryst Struct Commun* **1992**, *48* (5), 771–773. https://doi.org/10.1107/S0108270191011599.

(82) Prakash, J.; Tarasenko, M. S.; Mesbah, A.; Lebègue, S.; Malliakas, C. D.; Ibers, J. A. Synthesis, Crystal Structure, Theoretical, and Resistivity Study of $BaUSe_3$. *Inorg. Chem.* **2016**, *55* (15), 7734–7738. https://doi.org/10.1021/acs.inorgchem.6b01202.

(83) Meng, W.; Saparov, B.; Hong, F.; Wang, J.; Mitzi, D. B.; Yan, Y. Alloying and Defect Control within Chalcogenide Perovskites for Optimized Photovoltaic Application. *Chem. Mater.* **2016**, *28* (3), 821–829. https://doi.org/10.1021/acs.chemmater.5b04213.

(84) Surendran, M.; Chen, H.; Zhao, B.; Thind, A. S.; Singh, S.; Orvis, T.; Zhao, H.; Han, J.-K.; Htoon, H.; Kawasaki, M.; Mishra, R.; Ravichandran, J. Epitaxial Thin Films of a Chalcogenide Perovskite. *Chem. Mater.* **2021**, *33* (18), 7457–7464. https://doi.org/10.1021/acs.chemmater.1c02202.

Declaration of Authorship

I hereby declare that this thesis with the title "Ink-based preparation of chalcogenide perovskites as thin films for PV applications" and the work presented in it are my own and the result of my own original research. All sources and resources of other authors are marked as such and listed in the bibliography. And I have not submitted the thesis at any other university.

Ibrahim Simsek